PICOSECOND KERR GATED IMAGING OF PHANTOMS IN TURBID MEDIA

by

LEMING WANG

A dissertation submitted to the Graduate Faculty in Engineering in partial fulfillment of the requirements for the degree of Doctor of Philosophy, The City University of New York

1995

This manuscript has been read and accepted by the Graduate Faculty in Engineering in satisfaction of the dissertation requirement for the degree of Doctor in Philosophy.

7/14/95
Date:

Chairman of the Examining Committee:
Dr. Robert R. Alfano, Distinguished Professor of Science and Engineering, Department of Physics and Electrical Engineering, The City College of The City University of New York.

7/24/95
Date:

Co-Chairman of the Examining Committee:
Dr. Ping P. Ho, Professor, Department of Electrical Engineering, The City College of The City University of New York.

7/24/95
Date:

Executive Officer:
Professor G. Lowen

Dr. Roger Dorsinville,	Professor, Department of Electrical Engineering, The City College of The City University of New York.
Dr. J. Malinsky	Associate Professor, Department of Physics, Bronx Community College of City University of New York.
Dr. V. Petriceivic	Assistant Professor, Department of Physics, The City College of The City University of New York.

Supervisory Committee

The City University of New York

Abstract

Picosecond Kerr Gated Imaging of Phantoms in Turbid Media

By Leming Wang

Ph.D Advisors: R.R. Alfano and P. P. Ho

The focus of this thesis is to characterize, understand, and improve upon a picosecond time-gated optical imaging method to localize hidden objects inside turbid media with sub-millimeter resolution. It was found that imaging information can be transported through the scattering medium by early-arriving ballistic and snake photons. Effective improvements of the image spatial resolution, dynamic range, contrast and signal to noise ratio of phantoms hidden in biomedical turbid media were achieved using a picosecond time- and space-gated imaging system. The rejection rate of diffusive photons provided by the time and space imaging system was $\sim 10^{10}$ to select the early light. The spatial resolution of image signal through turbid media was experimentally determined by estimating FWMH of point spread function of a point source. The spatial Fourier spectrum of turbid media with and without hidden object were examined. The minimum detectable contrast difference of $\Delta OD=\sim 0.14$ or scattering coefficient difference $\Delta\mu=0.05mm^{-1}$ was demonstrated in a 50-mm thick highly scattering media with l_t = 4.6mm. Early-time-detected scattering attenuation coefficients of Intralipid solution was found. Images of translucent objects hidden in thick turbid media were obtained.

The thesis is divided into ten chapters. In the first chapter, the scientific background to field is introduced, which includes: several key issues to be investigated using the early light detection and spatial Fourier spectrum analysis in optical imaging in turbid media.

In Chapter II, the operational principles behind the experimental arrangements, in which the time- and non-time-resolved imaging methods, transmission characters of the imaging set up are discussed. In this chapter, (1) a traditional continuous wave (CW) transillumination imaging method (Diaphanography); (2) a picosecond Kerr time-resolved imaging system without spatial gate (Kerr imaging); (3) a continuous wave spatial gate imaging system (CW-F); (4) a time-resolved Fourier gate imaging system (K-F); and (5) a double-stage optical Kerr gate imaging system are discussed. In the chapter III, the optical properties of biomedical media are discussed at different wavelengths. In the chapter IV, the transmission of the image signal of a point source, as the basic element of an image, is presented. In the chapter V, the spatial Fourier transform of turbid media using a time-resolved imaging system and its application to image quality improvement are introduced, which includes Fourier spectrum of turbid media, the frequency filtering effect of an aperture on the image contrast and the temporal intensity distribution of the image signal through turbid media. Chapter VI focuses on the illumination intensity dependence of the image contrast in turbid media. The experimental results of the image contrast for both 1054nm and 527nm are described. In chapter VII, three basic influences onto the image quality in thick turbid media are discussed: 1) the size of the target; 2) the target depth (location) inside turbid media; 3) the minimum irradiation difference (the object contrast or contrast resolution) between the target object and the surroundings. The conclusion and future-direction of this work are fund in Chapter VIII. The appendix is in Chapter IX, The last two sections of this thesis are Bibliography and list of my publications.

Dedicated to

my parents, my wife and daughter

Acknowledgments

I would like to take this opportunity to express my sincere thanks to my parents, Wenna Li and Jiguang Wang. They have continuously encouraged me to pursue higher education and have made many sacrifices to give me tremendous support. Especially my mother, without her admonishments and sacrifices, it would have been impossible for me to continue my study. I will always be grateful to them for their encouragement and support.

I wish to thank my thesis advisors Professor R. R. Alfano and Professor P. P. Ho suggestion about problems and ideas, and for their patient guidance, rigorous training, continued counsel, and providing financial support during this research project. Most of all for their help of assistance in defining a thesis project. I would like to thank Professor Alfano for introducing the concept of ballistic and snake photons used in my thesis for imaging. I wish to thank Professor Roger Dorsinville and Dr. Nathan Ockman for many helpful discussions. I wish to thank Gang Zhang, Chenghui Liu, Feng Liu, Quanzhen Wang, Wubao Wang, Guichen Tang, L. L. Kalpaxis, Xiangchun Liang, Yuanlong Yang, and P. Galland for their valuable theoretical and experimental assistance. I wish to thank my fellow colleagues for their kindness and help and NSF, Mediscience Technology Corp., the Institute of Ultrafast Spectroscopy and Lasers and at the Medi-Photonics Laboratory for support.

Finally, I would like to thank my wife, Diana Oisin Lee, for her love, patience, understanding, and support.

TABLE OF CONTENTS

List of Tables

List of Figures

Chapter I

Introduction

I.1 Introduction

Seeing small hidden objects inside highly "scattering walls" remains one of today's most challenging technological problems in the development of optical mammography and tomography in biomedical and other applications. Optical technology[1-23] offers many advantages over conventional approaches such as X-ray in that it uses non-ionizing radiation to locate small objects such as tumors in their earliest stage of growth. One key issue of the time-gated early light imaging is the large scattering loss through thick scattering media, and secondly large dynamic range (> 10^{10}) is required to detect the weak transmitted early light through thick turbid biomedical media.

My thesis focuses on the development of a gated early-light imaging technique to detect phantom in highly scattering media such as breast cancer screening. When a photons travels through a turbid medium, three signal components[1,2] can be defined: diffusive, ballistic, and snake. The diffusive medium **D**, operates on the input pulse $I_0(t)$ profile to produce an output complex pulse given by:

$$I_{out}(t) = \mathbf{D}\, I_0(t) \qquad (I.1)$$

A schematic diagram of these three components is shown in Fig.I.1. The diffusive scattered photons of the signal travel over a much larger distance in turbid sample, while the ballistic ones take the shortest path through the turbid medium. The snake component arises from those photons scattering within a small forward angular cone that arrive at the onset of the diffusive component. In a highly turbid inhomogeneous medium, such as human breast, the contribution to the ballistic component becomes exceedingly small and is buried and merged into the snake/diffusive component. The early snake component preserves the image information, while the diffusive component loses most of the information.

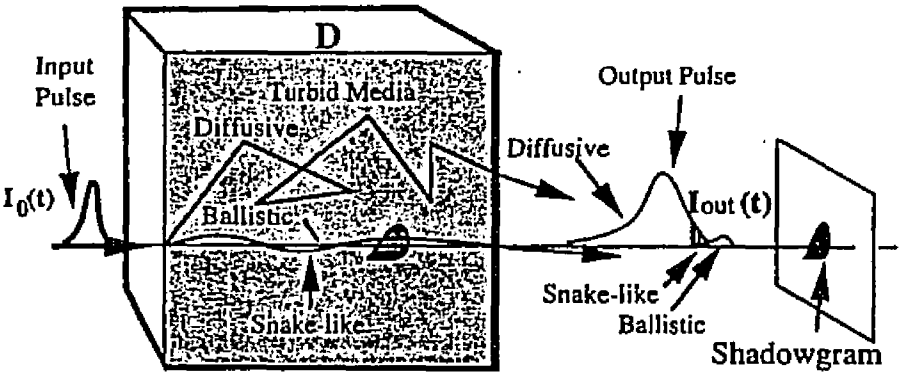

Fig.I.1. Three components of photons transmitted through a turbid medium.

I have investigated time-resolved optical methods to detect early arrival photons and obtain 2D images with ultra-high dynamic range and sub-mm spatial resolution for biomedical samples. Optical signal transmitted through the breast depends on the size,

amount of fat, composition, and optical density of skin and glandular tissues, vascular supply, the presence and extent of fibrosis, inflammation, cysts, and neoplasia. With today's ultrashort lasers and ultrasensitive detectors, a ~1mm spatial resolution of the optical image in a turbid medium may be achieved. This thesis describes 2D shadowgram images of objects hidden in highly scattering thick walls using 10 ps gate resulted part of transmitted light.

Over the past several years, various optical detection and imaging methods have been used to try to determine the location of objects through turbid and biomedical media. The theoretical approach was first proposed by Ewings and Adair in 1928 and actually tested by Culter on breast tissue in 1929 using steady-state transillumination (also called diaphanography). Direct visual interpretation has been used for extension to physical examinations of the breast. In this case the entire signal consisting of ballistic, snake, and diffusive components are detected without time or space gating. This results in the higher noise levels and poor spatial resolution(>1 cm). To improve upon this approach of optical imaging technique, ultrafast lasers, time-gating, space gating, and the new optical technique, and computer-assisted CCD system are now employed in a shadowgram approach.

Recently, several groups have pioneered advances using the early snake light for imaging. Using an optical Kerr gate[2-4], the early light was selected to generate clear images[2] of a 0.1 mm width test bar hidden behind a 3.5 mm human breast tissue. A photon counting based delayed coincidence detection technique from the Svanberg group[8] was developed to detect structures inside turbid media. Using picosecond semiconductor

diode laser[9] and 120 ps early light time-gating, a large tumor embedded in a 30 mm thick breast tissue could be identified with > 10 mm resolution. Reintijes et al.[10]used the nonlinear gain from stimulated Raman scattering[10] to enhance the quality of optical images in the scattering media. Chance, et al.[11-14] have demonstrated an optical imaging system using streak camera technology to study the deoxyhemoglobin in brain with a stimulation system. Chromo-coherent imaging was investigated by Spears[15] using the principle of the pulsed holographic interference technique. A holographic image is formed from the coherent (ballistic) part and is separated out from the incoherent (diffusive) part, which takes a longer path and contributes a uniform noise background. The time-resolved holographic technique has been further studied by Feinberg using a polymeric film[16] and by Valdmanis et al.. at the University of Michigan using electronic video recording[17]. Path-resolved imaging method by David A. Benaron[18], Stanford University, the SHG time-gated imaging by Yoo et al.[19], and the multi-wavelength imaging method by A. Duncan et al.[20]. A new reconstruction imaging method, (one being the Banana's imaging method), using diffusive light has been recently studied[21], in which, the inner structure of turbid media can be reconstructed by the measurement of the distribution of the photon path in turbid media.

For biomedical imaging applications, a significantly large dynamic range and ultrahigh SNR improvement are needed to obtain image information of an object in thick turbid media. For instance, for 80mm-thick chicken breast tissue with $l_t \approx 2.5$mm, the photon intensity is attenuated to very low level of $\exp(-50/2.5) \approx 10^{-10}$. A conventional time-gated approach may not achieve this required range and SNR. A Fourier spatial

filtering technique[22] coupled with ultrafast time gating can greatly improve the dynamic range and SNR forward this level ~ 10^{-11}. The angular spatial frequencies of scattering light will be forwardly Fourier transformed to the Fourier spectral plane. The central pattern arising from the collimated portion of the transmitted light represents the zero frequency (DC) component. The intensity of the region spread around the central part represents higher spatial frequencies. Higher angular frequencies are of larger radii. The earlier ballistic/snake and the later diffusive signals can be spatially filtered and separated out.

I.2 Thesis Statement

This thesis focuses on characterizing, understanding and improving upon optical imaging to locate hidden objects in turbid media with sub-millimeter resolution using picosecond time-gated optical imaging.

The following are the thesis goals:

1) Using picosecond time-resolved imaging for turbid media to give the quantitative determination of the imaging quality and the minimum object size;

2) Design and improvement of using time- and spatial-gated optical imaging approach;

3) Spatial Fourier spectrum imaging in turbid media and objects surrounded by turbid media;

4) Compares of CW, CWF, Kerr and KF imaging systems and as a function of the temporal intensity profile, sample thickness, spatial resolution and contrast, and analysis of SNR improvement in a sample with l_{tr} = ~5mm.

5) Resolution vs time for scattering media with l_{tr} = 2mm.

6) Improvement of SNR and temporal resolution of a multi-stage Kerr gate imaging system.

I.3 Definitions

The definitions of terms frequently used in my thesis are displayed in Table I.3.1.

Terms	Definitions
Ballistic photons	Coherent photons, which travels in a straight line parallel with original input direction, and arrives first. It is part of remaining light pulse scattered coherently.
Snake photons	Photons, which travels along a zig-zag path slightly off the original input direction, arrives after the ballistic photon, attenuates exponentially with distance as relation exp[-bZ/l_t], where snake transport distance l_t/b is larger than l_t, where b = b(Δt), is strongly dependent on Δt, the observation time window for the early portion of scattering light. The snake photons are those which arrive within an early time of Δt prior to parts of diffusive light. Snake photons are quasi-diffusive photon[23], which do not obey the diffusion statistics or equation.
Diffusive photons	Photon, which takes a random walk path and arrives late with a broad temporal distribution.
CW imaging	Signal detected in an ultrashort period of time
Time-resolved imaging	Averaged input signal in a long period of time is detected
Ballistic time	$T = L/c_m$, T: time needed for ballistic photon travels through distance of L in medium; c_m: the light speed in the medium (c/n).
Fourier spectrum	Intensity distribution as a function of spatial Fourier frequency
Spatial frequency	Different harmonic components obtained by spatial Fourier transform
Kerr gate	Gating operation produced by using optical Kerr effect
Space gate	Gating operation produced by using a spatial filter
4F Space gate	Gating operation produced by placing a sample and a spatial filter at front and back focal planes of the first Fourier transform lens, respectively. Two lenses are separated by 2F.
Kerr-Fourier (KF)	Gating operation of the combination of Kerr-gate and spatial gate
Spatial resolution	Detectable minimum separation of object

Signal to Noise ratio (SNR)	Intensity ratio of signal to noise: ~ I_{signal} / I_{noise}
Noise background	Average value of noise component
Object contrast	Variation of irradiation intensity from an object
Image contrast	Intensity variation of detected signal: $(I_{max} - I_{min})/(I_{max} + I_{min})$
Detection Sensitivity	For a certain SNR requirement, the minimum exposure value
l_s, scattering length	Mean free path between two scattering event
l_t transport length	~ l_s /(1-g), the mean value of the distances where a photon lost all information about the original input traveling direction, phase, and intensity due to the scattering.
g-factor	~ < cosine (α)>, mean value of cosine of scattering angles

References

1. K. M. Yoo and R. R. Alfano, "Time-resolved coherent and incoherent components of forward light scattering in random media", Opt. Lett., 15, 320-322(1990).
2. L. Wang, P. Ho, C. Liu, G. Zhang, R.R. Alfano,"Ballistic 2-D imaging through scattering walls using an ultrafast Kerr gate", Science, 253, 769 (1991)
3. A. Duguay and A. T. Mattick, "Ultrahigh speed photography of picosecond light pulses and echoes", Appl. Opt. 10, 1971, 2162-2170.
4. L. Wang, Liang, P. P. Ho, and R.R. Alfano, "Fourier -Kerr imaging in thick turbid media", Opt. Lett.,15, 1993 241-2435.
5. Navarro and A. Profio, "Contrast in diaphanography of the breast", Med. Phys. 15, 1988, 181-187.
6. B. Das et al., "Ultrafast time imaging in thick tissue", to be published in Opt. Lett.
7. K. M. Yoo, B.B. Das, R.R. Alfano, Opt. Lett., 17, 958 (1992)
8. S. Anderson-Engles et al.,"Time-resolved transillumination for medical diagnosis", Opt. Lett. 15, 1178-1180, (1990).

9. R. Berg,et al.,"Medical transillumination using short pulse diode lasers", Appl. Opt.. 32. 1993, 574-579.

10. M. Duncan, R. Mahon, L. Tankerskey, J. Reintjes, Spectral and temporal characteristics of spontaneous Raman scattering in transient regime", Opt. Lett., 16, 1868 - 1870 (1991)

11. B. Chance, J. Leigh, J. Miyake, D. Smith, S. Nioka, R. Greenfield, M. Finander, K. ufmann, W. Levy, M. Young, P. Cohen, H. Yoshioka, R. Boretsky, "Comparison of time-resolved and un-time-resolved measurements of deoxyhemoglobin in brain", Proc. Nat. Acad. Sci. 5, 4971-4975 (1988)

12. B. Chance, Ed., **Photon Migration in Tissues**(Plenum, New York, 1990).

13. E. Sevick, et al.,"Time-dependent photon migration imaging" SPIE, 1599, 1992,274-283.

14. B. Chance and R. R. Alfano, ed,"Photon migration and imaging in random media and tissue", SPIE, 1888, 1993.

15. K.G. Spears, J. Serafin, N.H. Abramson, "Chrono-Coherent Imaging for Medicine", IEEE Trans. Biomed. Eng. 36, 1210-1221 (1989); N. H. Abramson and K.G. Spears "Single pulse light-in-flight recording by holography", Appl. Opt., 28 1834-1841 (1989)

16. A. Rebane and J. Feinberg, "Time-resolved holography", Nature, 351, 378-380 (1991)

17. H. Chen, Y. Chen, D. Dillworth, E. Leith, J. Lopez, J. Valdmanis, "Two-dimensional imaging through diffusing media using 150-fs gated electronic holography

techniques", Opt. Lett., 16, 487-489 (1991)

18. D. Benaron, D. Stevenson, "Optical time of flight absorbance imaging of biological media" Science, 259, 1463-1466 (1993).

19. K. Yoo et al.,"Imaging objects hidden in highly scattering media using a femtosecond second-harmonic-generation cross-correlation time gating", Opt.. Lett., 16, 1991, 1019-1021. 20. A. Duncan et al.,"A multi-wavelength, wideband, intensity modulated optical imaging", SPIE,1888.

21. J. C. Scotland, J. C. Haselgrove, and J. S. Leigh,"Photon hitting density", Appl. Opt 4 1993

22. L. Wang, P. P. Ho, R. R. Alfano, "Time-resolved Fourier spectrum and imaging in highly scattering media", Appl. Opt. 26, 5043-5048(1993)

23. J. A. Moon, P. R. Battle, M. Bashkansky, and J. Reintjes,"Measurement of the achievable time-dependent point-spread-function of multiply-scattered light between the ballistic and diffusive limits", SPIE, 2389 (1995).

Chapter II

Experimental Arrangements for Optical Imaging

II.1 Transillumination Imaging

II.1.1 History of Optical Transillumination

Optical transillumination or diaphanography is a noninvasive optical procedure for examination of the breast involving transillumination with either visible or infrared light. The concept of transillumination of the breast was first introduced by Ewings (J.Ewing, *Neoplastic Disease,* Sauders, PA, 1928) and Adair of the Breast Clinic at Memorial Hospital in New York at 1928[1,2]. An earliest clinical examination using the transmission of light through the breast was reported by Cluter[1-3] in New York at 1929. Since the image signal level was too weak and the contrast was too low to be used in an actually clinical examination, the optical transillumination technique development was temporally stopped in 1940's. From 1950 to 1970's, the technique had been improved by Gros, et al by using a new light source, in which the most heat radiated from light was removed by a water cooling device[1]. In 1972, Gros et al, reported that they were able to distinguish benign from malignant lesions using light and coined the obscure term "diaphanography" to describe the transillumination process. One of the first commercial instrument was manufactured in Sinus Medical Equipment AB, Stockholm, Sweden. In 1978, the limitations of X-ray radiography in the case of young dense breast and the increasing

concern over the smallest radiation dose led to a reawakening of interest in diaphanography as a diagnostic method[2]. In 1980, Olsson et al. found that adding infrared wavelengths (by photographing the transilluminated breast with an infrared-sensitive film) considerably improved their ability to identify carcinoma. In 1980's, Isard, Ohlsson, Hussey, et al, have encouraged the view that diaphangraphy has a valuable role as a supplement to mammary radiography[2]. Ohlsson proposed a new method at Sweden, in which a high sensitivity color film and 35mm SLR camera were used to improve the detection sensitivity and specificity of the transillumination approach[1]. In Ohlsson's technique, the illumination light was delivered from a 75W halogen projector lamp by a fibercable for visual inspection and electronic flashlight for photography[1]. Watmough found out that the large-size light source caused the more scattering and decreased the resolution[2]. He used a new torch light with a small exit aperture to improve the resolution to less than 5mm in 1982[4]. Watmough, Carlson, and Drexler modified procedure by eliminating all light wavelengths except for visible red and near infrared and view the breast in real-time by using a TV vidicon tube and a television monitor. Carlsen called this new method "lightscanning". Based on the Carlsen's design, a two-wavelength commercial diaphanography was manufactured by Spectrascan, Inc.. The similar product (for instance, Spectrascan Litescan model 10) was stopped because of poor result. In 1987, Jacson, et al proposed and tested a transillumination tomography method. However this technique has not been used as a commercial product[4]. After 65 years development, the transillumination of the breast as progressed from a pocket flashlight to present sophisticated, computerized equipment for breast evaluation. The resolution was

determined to be 1cm and offer no specificity of tumor types (see section II.1.3 for detailed)

II.1.2 Principles of Diaphanography

Diaphanography or lightscanning method consists of shining light onto an scattering object and viewing the transmitted light on the opposite or nearby side. Any defects are observed as a shadow. In this method, a visual inspection of the superior aspect of teeth or breast is obtained when a light source is applied to the outer surface of the teeth or skin surface. The second part of the examination is to make either view the shadow in a monitor or take a color infrared photographic record using 35mm camera synchronized to a neon flash tube in the torch or a video system.

According to Ariel and Cleary[5], the criteria evaluated in breast examination are: (1) symmetry in overall transmission of both breasts, (2) detection of focal areas of decreased or increased transillumination, and (3) the vascular pattern of the superficial veins. The ratio of fibroglandular to adipose tissue determine the amount of light absorbed. Cysts are visualized as discrete, round areas of increased transillumination. Gradations of decreased transillumination of focal areas are noted in benign masses, such as fibroadenoness or papillomas. Poorly defined areas of markedly decreased transillumination are characteristic of malignancy.

Early diagnosis was based on visual analysis of different color signals transmitted through the breast, which can provide more information than black/white pictures to improve the accuracy of diagnosis. Experimental results have showed[1-4], there was no

clear distinction between transmission characteristics of neoplastic and benign lesions in the visible band (450 - 700nm), i.e., what were imaged was not the properties of the tissue and lesions themselfs. However, the image contrast with a white light illumination appeared in different characteristic colorations. Profio found that[1]: a carcinoma was generally dark blue and dim (indicating a high infrared/red radio and low overall transmission; a normal glandular tissue was gray and medium bright; fibrous tissue was white and bright; a fatty tissue is reddish and bright; blood (deoxygenated) was red and dim, even so dark no color can be perceived; fluid filled, blood-free cysts were distinguished by their much brighter appearance (greater light transmission because of less scattering and absorption than normal breast tissue). Watmough reported that the absorption of the light in hemoglobin is basis for the contrast and shift in the IR-to-red transmission ratio in diaphanography images. Cluter found that a variety of solid lesions absorbed more light than the surrounding tissue, appearing dark spots in the breast. Ohlsson pointed out that not only neoplasms and cystic lesions may be recognized by the technique but also areas of fibroadenosis by their characteristic intense charred color. He found in 1980[6] that breast tissues exposed to visible yellow light absorbs more than 99.95% of this light and the emitted radiation was red-infrared. Based on Watmough's report, the breast in younger woman appears in red-yellow tones; malignant changes appear as a brown-black color, benign conditions with an increase in the stroma or connective tissue, or hyperplasia of the parenchyma produces an intensely red color, which represents mainly adenosis (sometimes the red color is interspersed with lighter areas representing fibrosis); cysts containing clear fluid are seen as brighter areas

(sometimes is darker, and difficult to be distincted from a cancer).

Although color by itself is not sufficient for diagnosis, the obvious correlation between the contrast in infrared range and the red-ball concentration (RBC) make a lightscanning method useful in distinguishing carcinoma and benign lesions. Experiments by Watmough[2] shown that the density of blood in the tissue, (number of red cells per unit volume) was the factor giving rise to different colours of breast tissues and breast pathology observed upon transillumination with white light in vivo. The colours depended on the red cell. The experimental results of transmission percent for different concentration blood diluted by saline as a function of wavelength are shown in Fig.II.1.2.1. The (d) curve in Fig.II.1.2.1 suggests the concentration of red cell in breast is ~10% since a red colour image of breast usually is obtained with a white illumination. From Edward's results, the RCB concentration varying with different conditions of tissues[1] are shown in Table II.1.1.

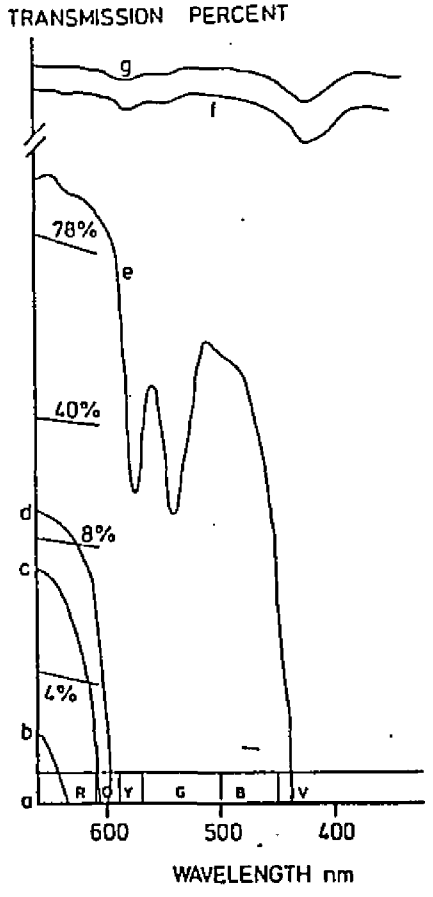

Fig.II.1.2.1 Spectrophotometric trace obtained with blood at a range of dilutions indicating optical cut-offs whose wavelength depends on the dilution factor. R:red;O:orange; Y:yellow; G:green; B:blue; V:violet; g:1/2000; f:1/1000; e:1/100; d:1/10; c:1/5; b:1/2; a:1/1.

It was found that the highest concentration occurred at the edge of a carcinoma;

the next highest one in the peripheral tissue immediately outside the carcinoma; the next

Tissues	RBC (mm^3/g)
Normal tissue	4.2
Fibroadenoma	5.4
Carcinoma (tumor)	4.9
Carcinoma (edge)	16
Peripheral tissue immediately outside the carcinoma	9.2

Table II.1.1 RBC of different types of tissues (Ref.1)

highest one in the peripheral tissue immediately outside the fibroadenoma. The third highest one is in the fibroadenoma, and roughly the same concentration was measured inside the acarcinoma and nontumorous tissues.

The contrast in infrared wavelength is related to the cell concentration, which is important in determination of carcinoma and benign. For instance, the region at the growing edge of a carcinoma has a higher RBC than fibroadenoma or normal tissue, carcinoma has higher RBC than fibroadenomas.

II.1.3 Drawbacks of Diaphanography or Lightscanning Techniques

Over the years, the breast diaphanography method has been investigated in clinical practice by several groups[1-10]. The examination results of diagnostic sensitivity and specificity usually were compared with that of a X-ray mammography. There have been a number of experimental results convincing the potential of a diaphanography to detect breast cancer[1-6,9], which includes: a two-wavelengths diaphanography is capable to detect some cancers, not be adversely affected by dysplastic breast, gives a rather good view in

young patients in where mammography gives poor penetration, and no radiation problem to which young women are especially sensitive[5], more easily distinguish benign lesions from cancers. However, due to the fact that a diaphanography test was examiner-dependent[1], the predicting sensitivity of clinical examination results were great different for different research groups. For instance, in Marshall's experiments, the diaphanography sensitivity was ~95%, which was very close to that of X-ray mammography[8]; while in Geslien and Sickles's experiments[4,10], it was about 20 - 50%, much lower than that of mammography. However, the overall evaluation results have shown that the sensitivity of diaphanography is still lower than the mammography, especially for a small size tumor (< 1 cm)[1,4-6,10].

To enhance the diagnostic sensitivity, the lightscanning technique has been experienced a series of improvements, which include: a new torch light source to detect the small-size lesions (Watmough), the multi-wavelength detection, a high sensitivity color camera, film, and television monitor,, and a spatial filter to decrease the light noise[1,2]. However, so far a poor spatial resolution is a fundamental weakness of a diaphanography, which limited the further development and application of diaphanography. One of problems is optical physicist was not involved in the development of the method and it was premedically tested by medical university. The lower sensitivity came from a poor spatial resolution, which is mainly caused by the diffusive scattering of photons by a breast tissue (additionally, a diffusive light source often used in a diaphanography also limited the spatial resolution). These diffusive scattering photons increased noise background, decreased the signal contrast, resulted a

loss of the fine structure of optical images, and finally caused a low predicting sensitivity and a high false rate in a clinical examination. The clinical examination has shown that for tumor size < 1cm, a sensitivity of ~30-44% for diaphanography was compared with a sensitivity of ~90% for X-ray mammography[3,7]. This caused poor detection capability for the early (first and second) stage tumor in comparing: ~87% for X-ray mammography, ~60% for diaphanography[3]. In addition, diaphanography is not adversely affected by dysplastic tissue, in which neoplasms embedded most often have been overlooked by X-ray mammography test[7]. More work is needed by experimental optical physicists and engineers to test and improve this method.

The research experimental and clinical results are showing the overcoming of the scattering has been seriously limited by using only conventional spatial improvement technique. In this thesis research, several new approaches have been proposed and tested to create a further improvement of the lightscanning diaphanography performance by addition of time and space gates. These new imaging methods concentrated on the elimination of the diffusive scattering photons before they arrive at detector to increase the SNR and resolution < 1cm of the images. The space gating is an addtional appraoch to improve the signal to noise ratio and discussed in the following section.

II.2 Experimental Arrangements

Four optical imaging arrangements have been used and tested in my research, they are: 1) a steady-state or continuous wave imaging system (CW system); 2); a

conventional picosecond optical Kerr gate imaging system (Kerr system); 3) a steady-state or regular continuous wave imaging system with Fourier spatial filtering (CW-F system); and 4) a picosecond Kerr-Fourier filtering imaging system (K-F system).

The main operational principles of these methods are described in this chapter. The detailed specifications of each method are discussed in the relevant chapters where they have been used.

II.2.1 Non-Time-Resolved or Steady State Imaging Method

A conventional lightscanning technique is a steady-state or continuous wave (CW) imaging system, which operates based on a non-time resolved imaging technique. The image is formed by the time-averaged transmitted optical signal since the image signal is received by a detector in a long period of time, such as in a breast diaphanography. The basis for the breast diaphanography is the differential transmission of optical radiation. The visible or IR source illuminates one side of a breast, and the output optical signal is detected in the other side. For CW integrated intensity detection, The output intensity has been expressed as[3]:

$$I = 4I_0(1+2D\alpha)^{-1}\exp(-\alpha x) \qquad \text{(II.2.1.1)}$$

D is diffusion coefficient, is equal to $\{3[\mu_s(1-g) + \mu_a]\}^{-1}$, $\alpha = (\mu_a/D)^{1/2} = L^{-1}$. L is the diffusion length, or penetration depth.

Recent research has shown that the detected intensity in the early time period of ~

300 ps can be expressed by a numerical formula (from Feng Liu's Thesis):

$$I_D \approx I_0 (l_t / Z) \qquad \text{(II.2.1.2)}$$

where l_t is the transport mean free path, and Z is the thickness of turbid media.

An numerical example for a 50mm-thick breast tissue estimated by the equation II.2.1.1 using the relation $D=(3l_t)^{-1}$, absorption coefficient of $\mu_a \sim 0.01 mm^{-1}$ and the mean free transport path of $l_t = 2mm$:

$I = 4I_0[1+2\cdot(3\cdot 2mm)^{-1}\cdot 0.0408mm^{-1}]^{-1}\exp(-0.0408\cdot 50mm) = 4\cdot 0.997\cdot 0.13I_0 = 0.518I_0$; and

$L = (D/\mu_s)^{1/2} \sim 24.5mm.$

However, with the same tissue parameters and thickness as above, Equation II.2.1.2 gives $I = 0.04I_0$, which is much smaller than that from eq. II.2.1.1. The reason for the difference is the $0.04I_0$ is detectable transmitted intensity in the early-period of ~ 300ps, while $0.518I_0$ is CW measurement result.

Due to the long time detection, the considerable light noise is received, and the image resolution is decreased to scale of centimeter in a conventional light transillumination imaging method. A relatively much slower detection compared to the traveling speed of the signal photons in the steady state or continuous wave imaging technique causes a serious loss of some important information, such as the variation of

index n along the travelling path and the time-dependence of the true image signal determined by the arriving-time difference between the ballistic/snake and diffusive photons. For instance, in the imaging of phantoms in the 50mm thick 2% diluted Intralipid solution using 10ps 1054nm laser pulses, the image signal part with highest resolution, contrast and SNR (ballistic/snake component) is only located in the earliest period of time of $\sim 10 - 40 \times 10^{-12}$ second. Meanwhile, the shutter speed of steady-state light imaging instrument is usually very slow, for instance, 30×10^{-3} second for diaphanography or lightscanning, which is operating in a TV video system. A shutter with such long opening time would actually let all photons including late-arriving diffusive noise part arrive at detector, which will result in a total distortion of an image.

II.2.2 Time-resolved Imaging Method

In a time-resolved imaging system, the image signal is detected in a very short period of time. The temporal distribution of the photons in turbid media with a 10ps opening time of an optical Kerr gate imaging technique is used in this research work. In this case, only the selected portion of signal photons is detected, which is not averaged with rest part of the signal arrives beyond the opening time of the optical gate.

The operational principle of a time-resolved imaging technique and a steady-state or non-time-resolved technique (CW technique) is shown in Fig.II.2.2.1a and b, respectively. In time-resolved imaging method (Fig.II.2.2.1.a), only the portion of the signal (the shadow area of the profile) covered by detection gate duration δt is detected.

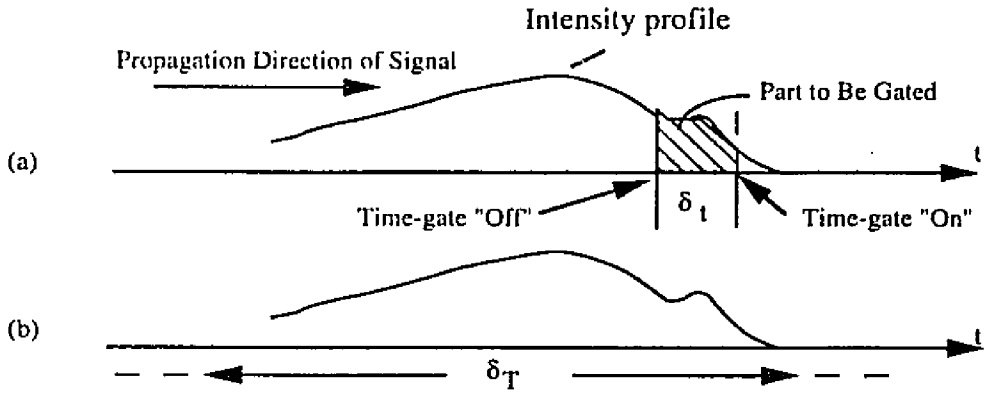

Fig.II.2.2.1 Principle of the time-resolved (a), and non-time-resolved detection (b). δt: detection duration of time-gate; δT detection time in non-time resolved process.

All the rest part of the signal is rejected before the signal is received by a detector. The gate position can be shifted to any place in the time-axis using an optical delay line to select a particular part to be detected.

In this research work, the gate width is determined by the width of the pumping pulse and release time of Kerr medium, which is ~10 ps (refer to the discussion on Kerr gate imaging in the following). In steady-state method (Fig.II.2.2.1b), whole signal profile, covered by the detection time period δT, is received by the detector. In this research work, a computer-controlled mechanical gate is used in cooled-CCD camera in the steady-state imaging experiment, the detection time is 4 second, which is much larger than that time duration of the output signal profile of scale of nanosecond.

When a laser pulses were broadened due to the multi-scattering, the early part of pulses were still carrying non-distorted signal, but the late part lost true image signal and became light noise. To separate the early-time signal (or any portion of the signal) from the rest, an time-gate has to be set in between the detector and the turbid sample and this

gate must be "on" at a proper time. When the adjustment of the "on time" of the time-gate synchronized with the left dashed line, the part of signal in δt duration (between dashed lines) is detected, and all the rest part of signal is rejected. The SNR improvement of this technique has been demonstrated to detect a hidden object in turbid media. The transmitted optical signal through highly scattering media consists of the early-arrival little-distorted signal part (ballistic/snake component) and late-arrival diffusive component. The signal SNR is proportional to the ratio of ballistic/snake component to diffusive component, i.e., SNR ~ $I_{true\ signal} / I_{diffusive}$, which is usually as low as 10^{-10} or even less for a highly scattering medium. To improve SNR, it is necessary to filter out as more diffusive photons as possible. Which can be realized by an early-time detection using an ultrafast time-resolved imaging system, where the gate interval δt is located at the T=0 to let ballistic/snake photons only pass through the gate. For a different case in which a conventional non-time-resolved (a continuous wave imaging system, CW system) is used, where there is no time gate, all part of the transmitted photons are to be detected (the early- and late-arriving photons are accumulated together). The mix-up of the true image signal carried by the early arriving-photons and the light noise formed by the later arriving-photons would result in an image blurring. In the actual bio-medical imaging and other applications, an ultrafast (a few picosecond or less) gate is needed to pick up the early-arriving photons from the diffusive light noise. An electronic imaging gate with the gate-opening time of a few picosecond is not available in market.

A picosecond optical Kerr gate has been involved in a time-resolved imaging system.

The operational principle of an optical Kerr gate and the imaging system is shown in Fig.II.2.2.2a and b[11-19]. respectively. The imaging system consists of a mode-locked Nd glass laser, a CS_2 Kerr shutter and an video image processing system. The 1054-nm laser pulse has a peak power $5x10^8$W with 8-ps pulse duration. The 1054-nm laser beam passes through a KDP crystal to produce the second harmonic component with a wavelength 527-nm and peak power of about 10^7W. The 1054nm (or 527-nm) pulse was used to illuminate the hidden object. The 527nm (or 1054nm) pulse was separated by a beam splitter and sent into a CS_2 cell to open the gate for ~10-ps. The thickness of optical glass cell is 1cm. The extinction coefficient for a pair of crossed calcite polarizers is $\sim 10^{-6}$, and ~2 x 10^{3-1} for a pair of crossed plastic polarizers. The aperture size of polarizers is 15mm diameter. The spot size of pumping beam on CS_2 cell is ~1cm maximum for 1054nm.

An picosecond optical Kerr gate is a time-varying nonlinear device, in which, the optical transmission characteristic is dominated by the interaction of the gating pulse and Kerr active medium. When an intensive linearly polarized laser pulse passed through a Kerr active medium, the difference of the induced indices of refraction parallel and perpendicular to the polarization direction of the orienting laser field can be written as:

$$\delta n(t) = n_2^e \langle E_g 2(t) \rangle + (n_2^0/\tau_0) \int \langle E_g^2(t) \rangle \exp(-(t-\tau)/\tau_0) d\tau \qquad \text{(II.2.2.1)}$$

where $\langle E_g^2(t) \rangle$ is the time averaged gating laser pulse intensity function which is assumed

be a Gaussian temporal profile $\langle E_g^2(t)\rangle = 1/2\ E_{g0}^2 \exp(-t^2/\tau_g^2)$, τ_g is the pulse width defined as e^{-1} decay time of the pulse envelope, n_2^e is the fast nonlinear refractive index caused by fast relaxation mechanisms such as electron cloud distortion; and n_2^o is the slow nonlinear refractive index caused by a slow (molecular) relaxation time τ_0. Using a slow detector, the transmitted signal of a probing pulse $\langle E_i^2(t)\rangle = 1/2\ E_{i0}^2 \exp(-(t^2/\tau_i^2))$ through a Kerr gate can be expressed as a function of delayed gating time τ_D:

$$S(\tau_D) = S_i^{-1} \int \langle E_i^2(t-\tau_D)\rangle \cdot G^s(t)\, dt \qquad \text{(II.2.2.2)}$$

where $G^s(t)$ is an optical transfer function with the superscript s correspond to a single stage optical Kerr gate: $G^s(t)=\sin^2(\pi L/\lambda\ \delta n(t))$. $S_i = \int \langle E_i^2(t)\rangle\, dt$ is the normalized probing pulse intensity; τ_D is the delayed gating time between the gating pulse and probing pulse; τ_i is the e^{-1} decay time of the probing pulse.

The transmission efficiency for a single stage Kerr gate was about 5-10%. The image was measured by an intensified 2D CCD camera (from VIRO and Pulnix) with gain of ~10^4 times or a cooled CCD camera (from Photomatrix). The Pulnix CCD camera has 640x480 pixles, 256 gray levels (8bit), and the real time (TV) operation version. Photometrix camera has 512x512 pixles, 65000 gray levels (16bit), and ~10 second readout time for 512x512-pixles area. For Photometrix CCD camera cooled down to -45-degree Centigrade, the detection sensitivity is ~20 photoelectron/bit. For

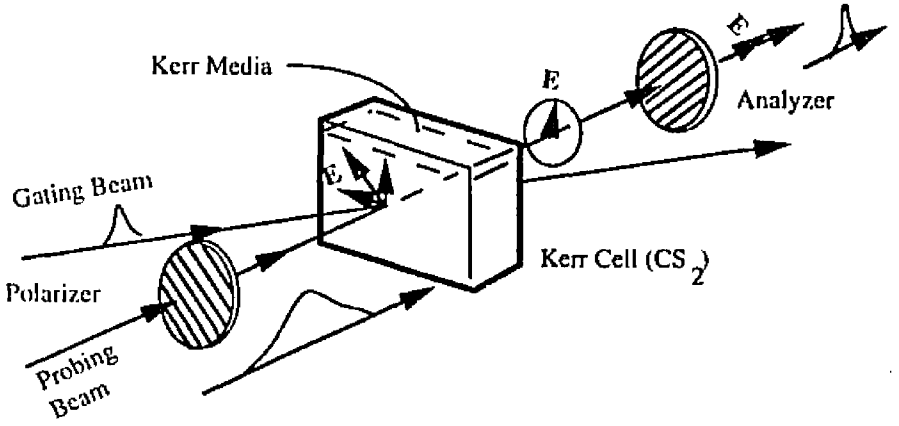

Fig.II.2.2.2a Operational principle of an optical Kerr gate.

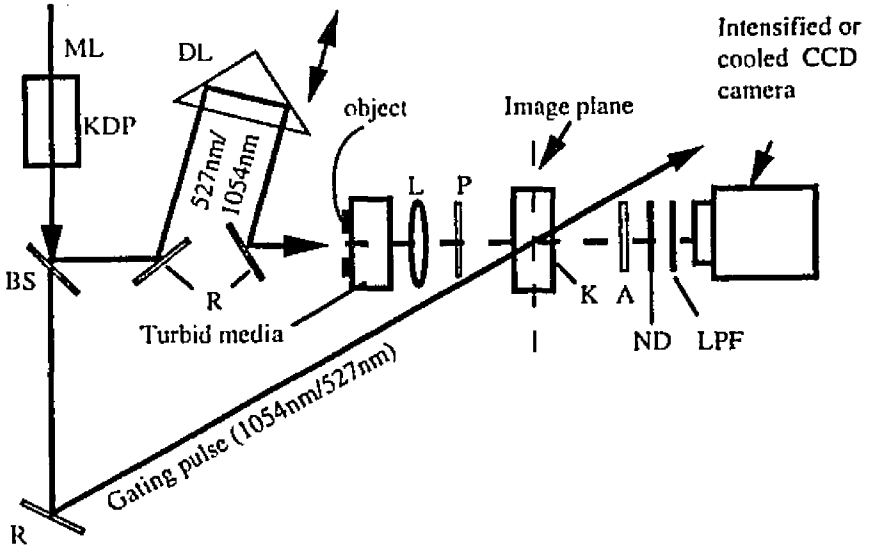

Fig.II.2.2.2b Experimental setup of single optical Kerr gate imaging system

A laser-pulse train from a mode-locked Nd:glass laser was used to study the gate, ML. The laser-energy fluctuation was ~5% from shot to shot. KDP, potassium dihydrate phosphate crystal for a SHG pulse; BS. beam splitter; S, sample; DL, delay line; P, and A, polarizer, and analyzer oriented at -45° and +45° with respect to the polarization of the probing beam. Plastic (Poloroid HN22) or calcite polarizer has been used. K, 1-cm long CS_2 Kerr cell; L, lens with focal length ~35cm - 60cm; ND, nutral density filters; NB, narrow-band filters, ICCD, image-intensified CCD camera detector with ~10^4 gain, or cooled CCD with sensitivity ~1 count/20 photons. The Kerr active medium carbon disulfide liquid in an 10mm thick optical glass cell. The whole system was controlled by a PC computer, which was triggered by the laser firing signal from the laser power supply. The transmitted signal pulse was recorded by an CCD camera. From which, the output signal was send to a PC computer to be processed
and displayed.

1054nm wavelength, quantum efficiencies ~8%. Therefore, the minimum detectable number of photons is ~250 photons. A IBM/PC computer for Pulnix CCD and a Mac II are used for Photometrix CCD camera, a frame grabber and software package were used to store and process the image data.

Temporal resolving capability of a time-resolved imaging system is an important requirement. The experimental results have shown that the system has been used in this research can resolve signals in ~3.3ps when the signal intensity varys equal to or more than 20% in 3.3ps interval. In this case, the laser output has to be kept less than 10%. When the power density of gating pulse is too high, the gate opening time would increase due to the saturation[18,19]. When the pumping intensity is to low, the detectable signal level would be limited. To match both the requirements, the Kerr conversion efficiency is kept at ~10%, that is, the 10% signal pass through the gate when the gate is "on".

When a input optical signal $E_s(t)$ passes through a Kerr gate, the intensity of the gated signal through the Kerr gate can be represented by[11-14]:

$$I(t_d) \approx \int_{-\infty \rightarrow +\infty} E_s^2(t)G(t-t_d)dt \qquad \text{(II.2.2.3)}$$

where, G(t) is the pumping pulse intensity profile:

$$G(t) = E_g^2(t) = E_0^2 \exp-(t-t_0)^2/2(\Delta t)^2 \qquad \text{(II.2.2.4)}$$

where, t_d is the gating time, and Δt is the e^{-1}-width of the pumping laser pulse.

The temporal resolution of an optical Kerr gate used in my research is ~3.3ps. That is, the intensity change of gated signal ~20% when the gating time delayed by ~3.3ps. The reason why choosing 20% is to make sure the measurement of a gated signal is stable and reliable even when the laser power fluctuates by 10%. The calculated intensity decrease of the gated signal $I(t_d)$ is ~20% if Δt is 5ps, and $t\text{-}t_0$ is 3.3ps, which is consistent with the experimental results.

The SNR mainly depends on the ratio of transmittance between a crossed and a parallel polarizers for a signal stage optical Kerr gate. Two factors must be considered: the extinction rate of polarizers, and Kerr efficient. The higher extinction rate and Kerr efficiency produce the higher SNR. The lower extinction rate will caused the more leakage of diffusive noise. The lower Kerr efficiency will cause the more loss of true signal. The extinction coefficient of a pair of polarizers corresponds to the system SNR, which is ~10^6 for calcite polarizers, and Kerr efficiency is ~10%. Which yield a SNR ~10^5 for a conventional single stage Kerr gate imaging system.

To improve the temporal resolving capability and SNR of an optical Kerr gated imaging system, a multi-stage Kerr gated system was developed, which will be described in detailed in Chapter II.3. The basic operational principle of a double-stage Kerr gated imaging system can be briefly explained using Fig.II.2.2.3a, b, and c. Output signal photons travel through the two stage of Kerr gates serially connected. The temporal positions of two time gate can be independently shifted to the earlier or later using a corresponding optical delay line, separately. The time difference between two gate, δt, depends on the position difference of each gate time with respect to the same part (it may

be the zero-point) of the signal.

In the first stage Kerr gate (refer to Fig.II.2.2.3a), only the part of signal, which arrives at the same time as the probing laser beam in the first Kerr cell, pass through the analyzer (the second polarizer) of the first stage, and enter the first polarizer of the second stage Kerr gate. This gated part of the signal is sent to the second Kerr cell to be gated by the pumping pulse, which comes out from the first Kerr cell. The arriving time of the

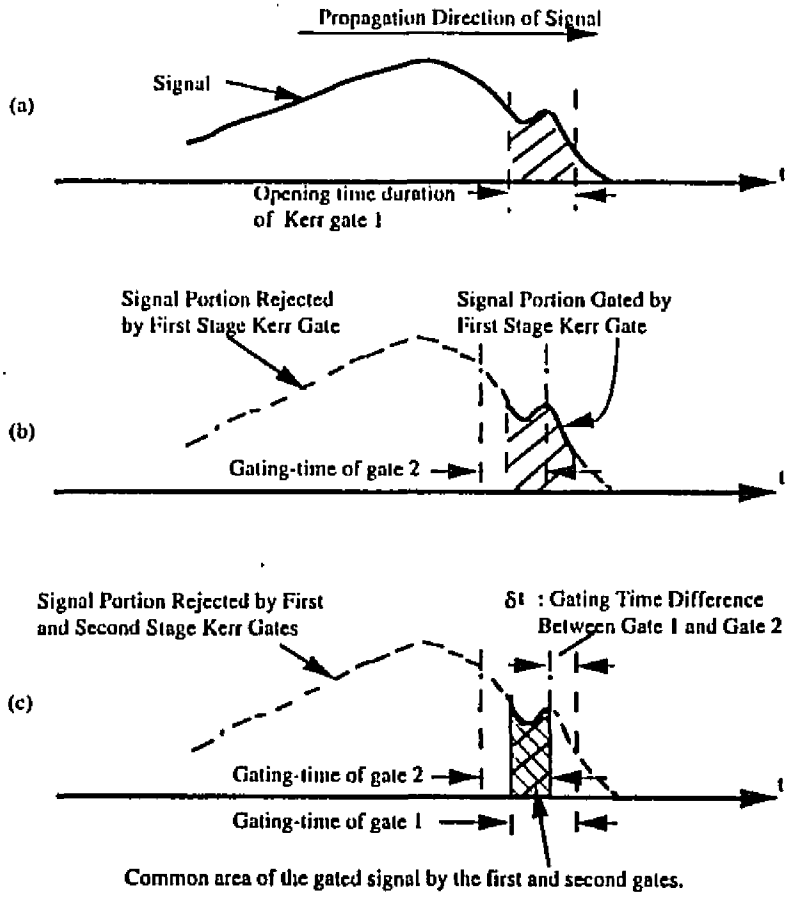

Fig.II.2.2.3 The principle of a double-stage optical Kerr gated imaging system.
δt: the time difference between two Kerr gate determined by a delay line.

pumping pulse at the second cell can be adjusted earlier or later with respect to the gated signal by an independent delay line. That means, when these two gates were opened at different times with respect to the arriving time of the signal (i.e., δt is not zero), only the portion of the signal appearing in the common range of gating time of the two gates will pass the 1st and 2nd Kerr gates and arrive at the detector, as shown in Fig.II.2.2.3c.

II.2.3 Fourier Spatial Filtering Method

When a plane wave illuminate an object, the light will be scattered into different directions in space[21-22], as shown in Fig.II.2.3.1. This scattered light represents a spatial

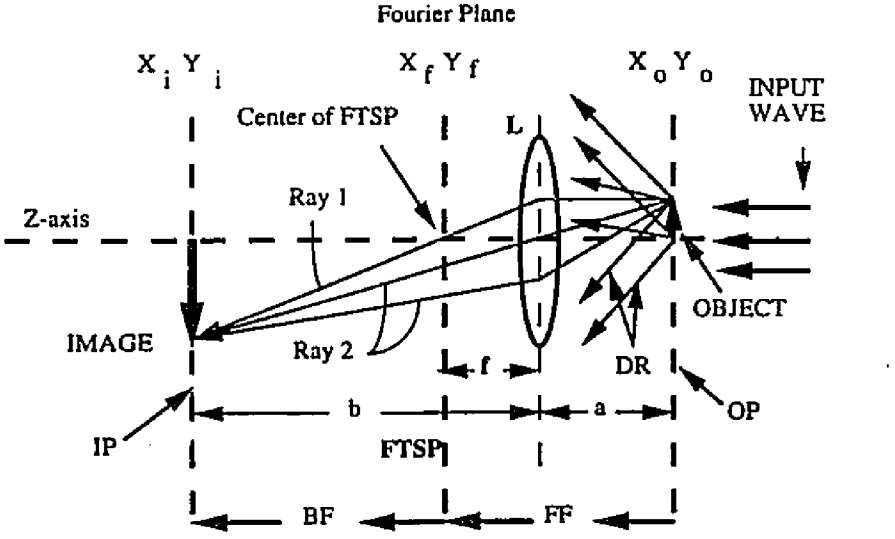

Fig.II.2.3.1 Spatial angle frequency and Fourier transform in optical imaging OP: Object plane; IP: Image plane; DR: Diffractional Ray; FTSP: Fourier transform spectrum plane; FF: Forward Fourier transform; BF: backward Fourier transform; f: Focal length; a: Object distance; b: Image distance.

angular frequency spectrum of the object shape. The angular frequency components can

be displayed on the Fourier plane. A diffraction pattern consists of a series of different spatial frequency components on the Fourier plane. The center of the diffraction pattern which comes from the collimated diffraction light represents the zero frequency DC component. The spatial region spread away from the central portion represents higher frequency components. The higher angular frequencies are located at larger radii on the Fourier plane.

The spatial frequency of an object under the forward Fourier transformation is defined to be[21]:

$$f_x = \Delta X/(\lambda\ f) \qquad \text{(II.2.3.1)}$$

where the scale unit of the f_x is lines/mm, λ is the wavelength of the illumination laser, and

f is the focal length of the lens L, and ΔX is the half width at full maximum (HWFM) of the

Fourier spectral profile of the object at the back focal plane. For an object illuminated by a plane wave, the radius of the diffraction image is equal to:

$$\Delta X = f\ \Delta\Theta \qquad \text{(II.2.3.2)}$$

here $\Delta\Theta$ is the angle of diffraction of the object. For a slit object of width D, $\Delta\Theta$ can be approximately to be

$$\Delta\Theta \sim \lambda/D. \qquad \text{(II.2.3.3)}$$

For a round object with diameter of D, $\Delta\Theta$ can be approximately to be

$$\Delta\Theta \sim 1.22\,\lambda/D. \qquad \text{(II.2.3.4)}$$

Using eqs.II.2.3.1 to II.2.3.4, the Fourier spatial frequency of an object is ~ 1/D. For example, when the width of a slit is 0.5mm, the corresponding spatial frequency at 1.06μm wavelength is $1.06\text{x}10^{-6}/0.5\text{x}10^{-3} \approx 2$ line-pairs/mm (or 2 Circles/mm).

Using Eq.II.2.3.1 and II.2.3.2, the forward Fourier transformation which forms a spatial Fourier spectrum, U_{FF} at the back focusing plane of the lens, can be expressed as:

$$U_{FF}(x_f,y_f) = A_1 \iint t_0(x_0,y_0)\cdot\exp(-j2\pi/\lambda\cdot f(x_0x_f+y_0y_f)dx_0dy_0, \qquad \text{(II.2.3.5)}$$

and the backward Fourier transformation which formed a real image, $I(x_i,y_i)$ at the imaging plane can be expressed as:

$$I(x_i,y_i) = A_2 \iint U_{FF}(x_f,y_f)\cdot\exp(j2\pi/\lambda\cdot f(x_fx_i+y_fy_i)dx_fdy_f, \qquad \text{(II.2.3.6)}$$

where, x_0 and y_0 are displacements at object plane in x & y directions; x_f and y_f are displacements at Fourier spectrum plane (back focusing plane); x_i and y_i are displacements at image plane; A_1 and A_2 are phase terms.

The major energy location in the spatial modulation spectrum is proportional to the

reciprocal of the size of spatial variation of the modulation: for the spatially larger area modulation, the higher energy density appears at the lower range of the spatial spectrum, and for the smaller area modulation, it does at the higher range of the spectrum. Any modification (filtering) of the spatial spectrum pattern by removing part of the components will change the image resolution and contrast.

To examine the spatial frequency distribution of collimated light through turbid media, the transmitted signal of turbid media has to be measured at Fourier transform spectrum plane (FTSP) in a time-resolved 4F imaging system. When collimated laser light travels through turbid media, they emerge at different directions into half-space. The ballistic/snake photons travel in a zero or small diverged angles with respect to the original laser beam path; the diffusive photons distribute in a π space angle which include the non-co-linear (large-angle) photons and the co-linear (small angle) photons. The early-arriving part (ballistic/snake component) of the small-angle photons carry the least-distortion image signal.

The spatial filter, which is based on the Fourier analysis on the transmitted signal through turbid media discussed as above, can be used to improve the image quality by filtering out the noise photons at FTSP. An example of optical filter is a circular mask, or a aperture as shown in Fig.II.2.3.2. The optical setup shown in Fig.II.2.3.2 is a 4F system, in which object is placed at front focal plane of first lens and the image is formed at back focal plane of the second lens, respectively. The co-focal plane of the two lenses in between the first and second lenses, is called Fourier spatial spectrum plane (FTSP). The first lens collected the image signal and resolves (forward Fourier-transform) them

into different spatial frequency components, displayed in a specific spatial distribution in FTSP. The second lens reforms (back Fourier-transform) the components into a real image at back focal plane. A specially designed mask can be placed at FTSP (for example, a aperture) to modify the passing signal. The circularly symmetric low-pass filter has a transfer function:

$T = 1$ if $f_x^2 + f_y^2 \leq f_c^2$, and $T = 0$, otherwise.

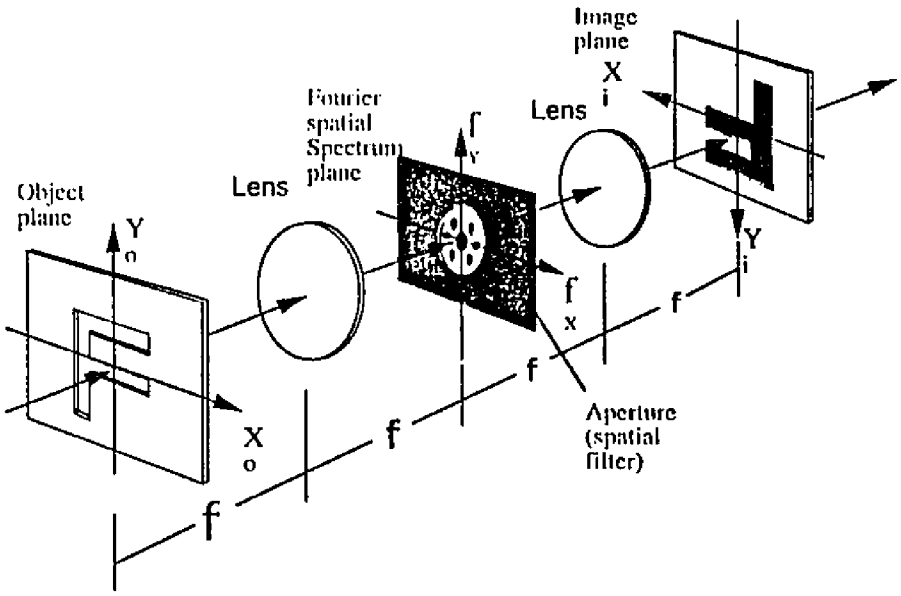

Fig.II.2.3.2 Principle of spatial filtering of a 4F imaging system.
The unit in object and imaging plane is mm, and the unit in spatial frequency is pair-line per mm. f is focal length of lens. An aperture works as a spatial filter.

where f_x and f_y are Fourier spatial frequencies in X- and Y- coordinates, and f_c is cutoff frequency, which is equal to the radius of the mask (aperture window). It passes spatial frequencies that are smaller than the cutoff frequency f_c, and blocks the higher frequencies. This filter is implemented by a mask in the form of a circular aperture of diameter D, with $D/2 = f_{x,y} \cdot \lambda \cdot L_{focal}$. For example, if D = 3mm, λ = 1.06μ, and L_{focal} =

600mm, $f_c \approx 2.5$ lines/mm. This filter eliminates spatial frequencies that are greater than f_c. The size of details in the filtered image is approximately 0.4mm.

The aperture size as a function of cutoff frequency f_c at 1054nm and 527nm at Fourier plane is shown in Fig.II.2.3.3. The high-pass filter is the complement of low-pass filter. It blocks low frequencies and transmits high frequencies. The mask is a clear transparency with an opaque central circle. The filter output is high at regions of large rate of change and small at regions of smooth or slow variation of the object. The filter is therefore useful for edge enhancement in image-processing application. The vertical-

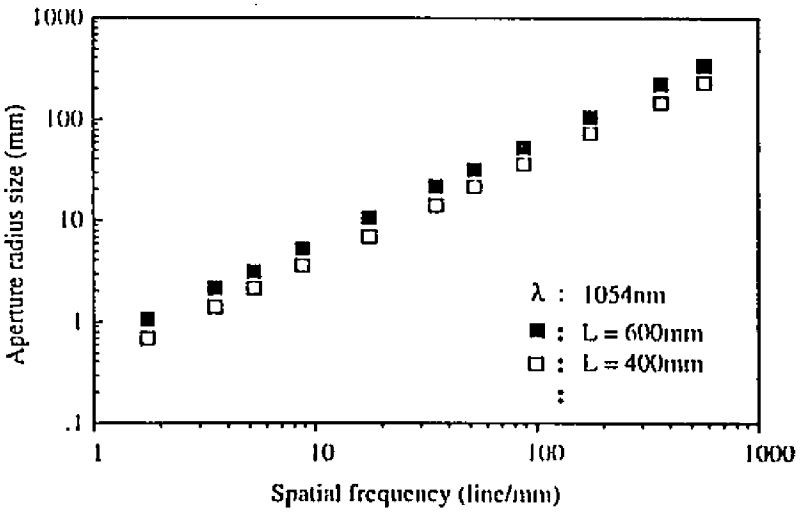

Fig.II.2.3.3 The cutoff frequency as a function of aperture size at FTSP for a coherent imaging system.

pass filter blocks horizontal frequencies and transmits vertical frequencies. Only variations in the x direction are transmitted. If the mask is a vertical slit of width D, the highest transmitted frequency is $f_y = D/2 \cdot \lambda \cdot L_{focal}$.

In the optical image signal transmitted from turbid media, the true signal is mainly concentrated at the center area of FTSP at the early time (ballistic/snake photons), while

the noise component used to be spread over larger radii area at the later time. At the late time detection, the diffusive photons at the out surface of turbid media distribute approximately uniform in a π half-space. The fraction of the diffusive noise energy, R, which is filtered out by a small size aperture set at FTSP can be calculated as shown in Fig.II.2.3.4:

$$R_s = \frac{\text{The diffusive photon noise energy leak through the aperture}}{\text{Total diffusive photon noise energy in a solid angle of } \pi}$$

$$R_s = \tan^{-1}\left\{\frac{\text{Aperture diameter } d}{\text{Focal length f}}\right\}^2/\pi = \sim \left\{\frac{\text{Aperture diameter } d}{\text{Focal length f}}\right\}^2/\pi$$

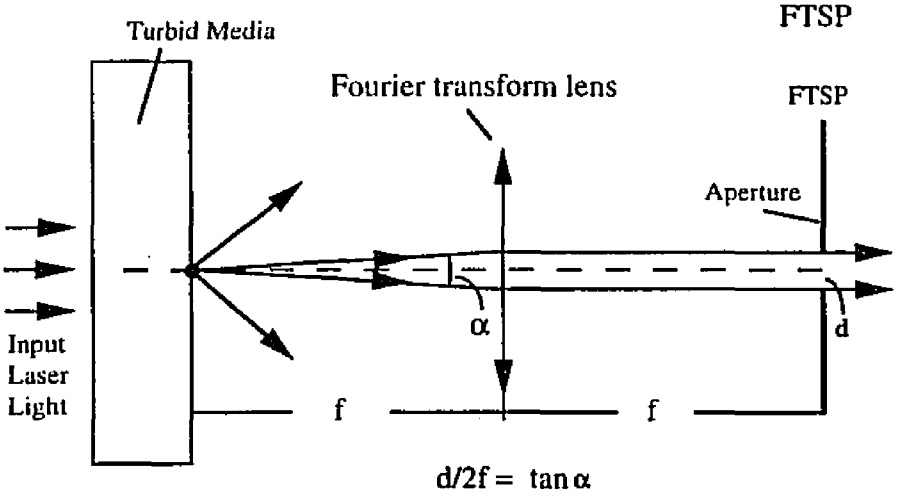

Fig.II.2.3.4 Diagram used to calculate the fraction of diffusive photons passing through the aperture set at Fourier transform spectrum plane (FTSP). d: aperture diameter; : collection angle determined by d; f: focal length; L: forward Fourier transform lens.

where R_s represents the rejection efficiency of diffusive intensity by a space filter (an aperture). For example, if the focal length of Fourier transform lens is f = 600mm, the diffusive photon noise energy leak through the aperture (at FTSP) with diameter of d = 1mm is:

$$R_s = \sim 600^{-2} / \pi = \sim (1/600)^2 \pi^{-1} \sim 10^{-6}.$$

In experiments, an adjustable aperture was chosen to work as a spatial filter because it is easy to be combined with an optical Kerr gate (refer to the principle of a continuous wave system with spatial filter (CW-F system) and a time- and space-gate imaging system are shown in Fig.II.2.3.5a and b, respectively). In Fig.II.2.3.5a, a mechanical aperture was set in Fourier plane (FTSP). In Fig.II.2.3.5b, an intensive picosecond gating pulse was focused inside the Kerr-active medium, CS_2, induced a small size soft aperture, The 8ps duration and small size aperture can provide both the early-time and collimated imaging detection. An adjustable mechanical aperture is placed at Fourier transform spectrum plane (FTSP). The sample to be detected is placed at the front focal plane of the Fourier transform lens. Due to the nature of Fourier transformation of this optical setup, the signals will be resolved into the different Fourier spatial components at Fourier transform spectrum plane (FTSP): the collimated photons (DC component) at the center point, the lower frequency component at the small-radii area around the center, and the higher frequency components appear at the larger-radii area. Only the frequency at the small-radii area around the center, and components (DC and some lower frequencies)

located at the window area of the aperture can pass through. The varying of the mechanical aperture size will determine the spatial frequency up-limitation of the input signal arriving at image detector. The advantage of Kerr-Fourier design in Fig.II.2.3.5b compared to the CW-Fourier design in Fig.II.2.3.5a is that the early-time-induced aperture in Kerr-Fourier system can provide highest signal fidelity by a more effective noise reduction. The late-arriving co-linear diffusive photons, which fly in a small diverged angle, can leak through a small-size mechanical aperture, but be rejected by an early-time detection in Kerr-Fourier imaging system.

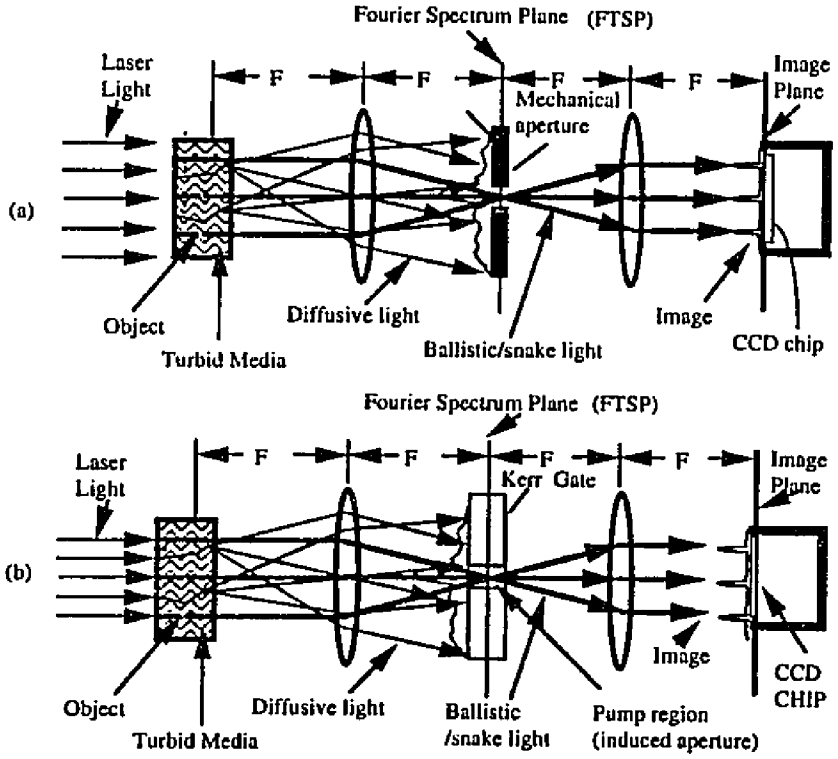

Fig.II.2.3.5 The principle of a continuous wave imaging system with a mechanical spatial filter (a), and a time- and space-gated imaging system.

The total reduction of diffusive component for a single-stage time- and space- gate system is: $R_T = R_t \cdot R_s \approx 10^{-5} \cdot 10^{-6}$, that is, $R_T = 10^{-11}$.

The rejection rate of diffusive photons provided by a single-stage space gate- (CW-collimation), time- gate, and time-space gate are displayed in Table II.2.3.1.

Gate Type	Space gate (collimated Method)	Time gate	Time- and Space-Gate
Rejection Rate	~10^6	~10^5	~10^{11}
System Specs.	Aperture size: 1mm	Calcite polarizer 10ps gating pulse	Aperture size: 1mm Calcite polarizer, 10ps gating pulse

To enhance the rejection rate to above 10^{11}, a double-stage K-F imaging system may be used. In which the diffusive photon rejection rate of ~10^{17} to 10^{19} is expected (refer to section II.3).

II.2.4 Optical Imaging Arrangements

Four experimental imaging arrangements have been used in this thesis:: 1) a regular continuous wave imaging system (CW system) is shown in Fig.II.2.4.1; 2) a conventional picosecond optical Kerr gate imaging system (Kerr system) is shown in Fig.II.2.4.2; 3) a regular continuous wave imaging system with Fourier spatial filtering (CW-F system) is shown in Fig.II.2.4.3; and 4) a picosecond Kerr-Fourier filtering imaging system (K-F system) is shown in Fig.II.2.4.4.

In Fig.II.2.4.1, the signal is directly detected by detector (CCD camera). The reduction of the noise background is mainly depends on the small collection angle of the camera and proper color filters. The SNR of the detected image is usually very poor in imaging through turbid media, such as in breast diaphnography.

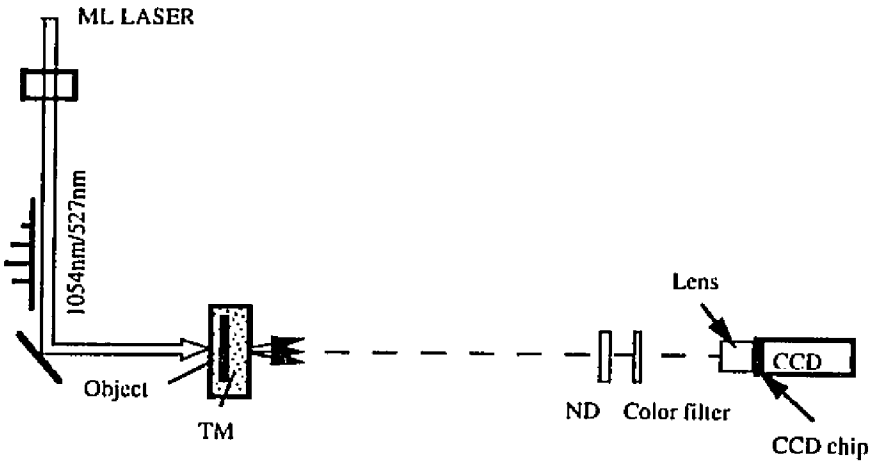

Fig.II.2.4.1 A regular CW imaging system.

In Fig.II.2.4.2, an optical Kerr gate is used to reduce the noise level by an early-time detection. When the signal passes through the Kerr gate, only the photons meeting the pumping pulse in Kerr cell pass the analyzer to be detected. A main disadvantage of a conventional Kerr gate (as shown in Fig.II.2.4.2) is the high frequency noise is mixed up with the low frequency and DC signal (i.e., the noise component is not separated from the true signal spatially) when the Kerr cell is placed in a non-Fourier spectrum plane, and the noise reduction capability is limited.

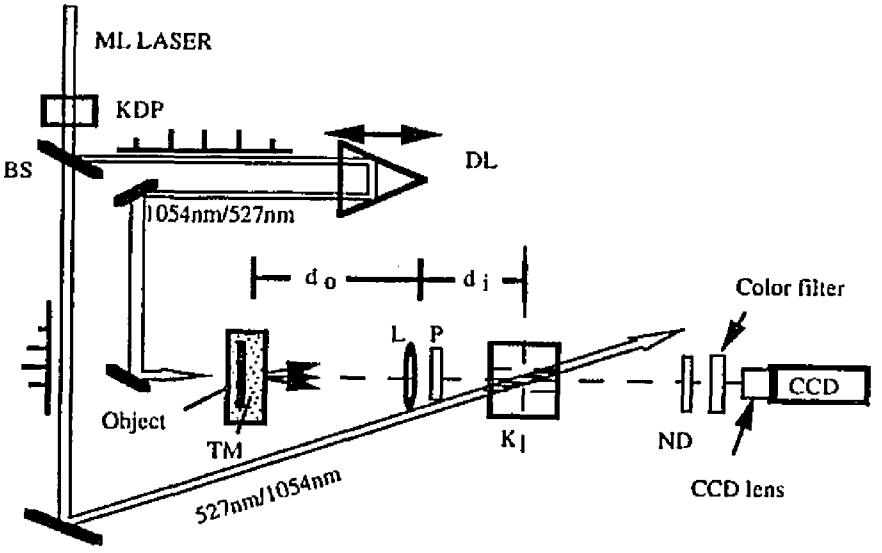

Fig.II.2.4..2. A conventional optical Kerr gated imaging system.

Fig.II.2.4.3 shows a steady-state imaging system with a spatial filter set at FTSP (CW-F system). The arrangement of the Fourier transform spectrum plane (FTSP) make the most of the scattering light noise be separated from the major part of the true image signal (concentrated at the lower frequency and DC component) in space. Due to the non-time-resolved detection, CW-F imaging system can't completely reject the late-arriving co-linear diffusive photons.

A Kerr-Fourier imaging system is shown in Fig.II.2.4.4, which combine the Kerr gate and Fourier spatial filter in a same system to create a maximum SNR improvement.

The signal is resolved into different spatial frequency components at FTSP located in the middle of the Kerr cell to be time-gated, then form the image in CCD chip. In an actual

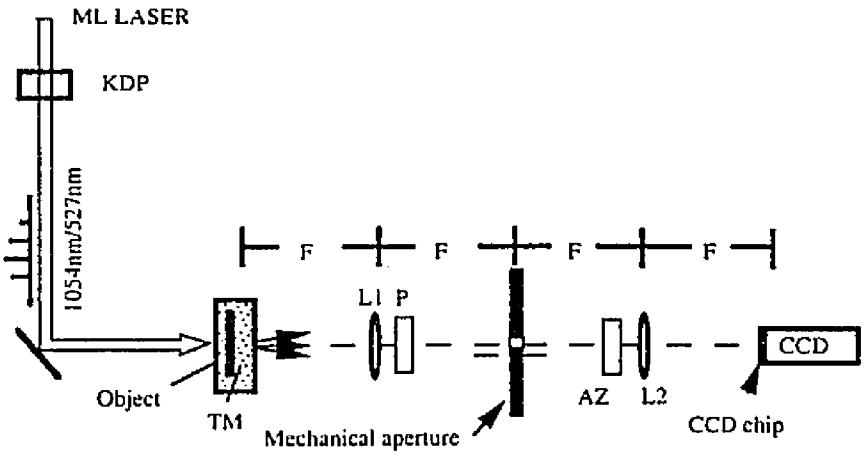

Fig.II.2.4.3 A CW-F imaging system

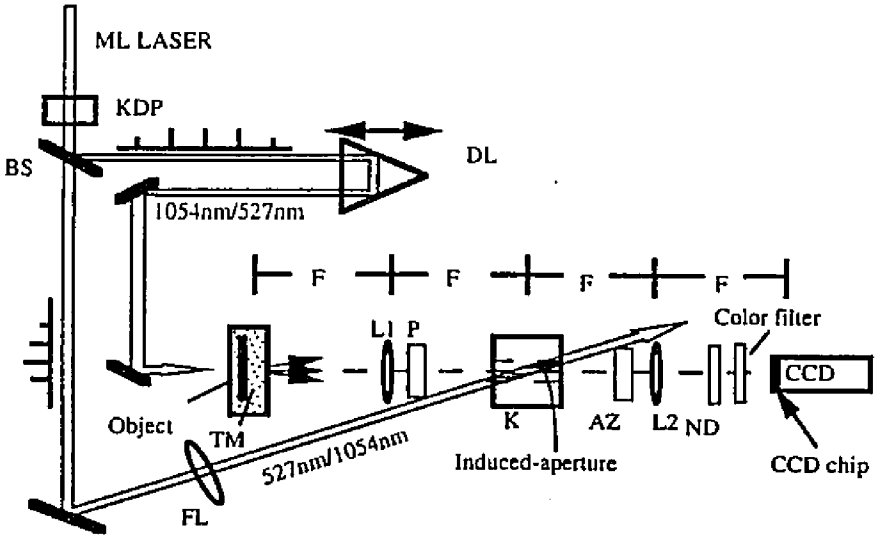

Fig.II.2.4.4 A time- and space-gated imaging system.
L1 = 60cm, L2 = 20cm

experimental setup, the focal lengths for L1 and L2 is 30 ~ 62cm, and 15-18cm, respectively. The laser beam diameter is ~ 1cm. The input collection angle is ~1°. The resolution is ~100μm in clear water.

The collimation is different from the Fourier filter used in the imaging system of this research. The former is a method used to change non-collimated light to collimated light by filtering out non-collimation component. The Fourier spatial filter used in this research is an optical signal processor by placing a space mask at Fourier plane. The mask would modify the transmittance of different frequency components of passing signal to improve image quality.

II.2.5 Modulation Transfer Function

II.2.5.1 Background

An image signal is a modulated distribution of the illumination light intensity and phase caused by the difference of optical properties in different positions of an object to be imaged. For incoherent imaging process, an image I_{out} (x,y) formed by an imaging system can be expressed as a convolution of this modulated signal intensity $I_{input}(x, y)$ and the intensity transfer response of the imaging system for a point light source, h(x,y):

$$I_{out} = A\, I_{input}(x, y) * h\,(x,y)$$

$$= A\, I_{input}(x, y) * PSF\,(x,y); \qquad \text{(II.2.5.1)}$$

$$h(x,y) = PSF(x,y);$$

where,'*' represents a convolution operation, and h (x,y) is also referred to the Point Spread Function, PSF, in imaging process.

PSF describes the spread distribution of a point source image. The Fourier transform of PSF is defined as the optical transfer function, OTF, which characterizes the performance of the imaging system in term of spatial frequency components as shown by equation II.2.5.2:

$$OTF(x_f,y_f) = A \iint PSF(x,y)\cdot\exp[-j2\pi(x_f x + y_f y]dxdy$$

$$= A \; |\, OTF(x_f,y_f) \,| \cdot\exp[-j\Phi(x_f,y_f)] \qquad \text{(II.2.5.2)}$$

where x_f,y_f are the spatial frequency defined in Fourier plane; A is normalization factor, and the is the modules of OTF; $\exp[-j\Phi(x_f,y_f)]$ is the phase of OTF. In equation II.2.5.2, the first term $|\, OTF(x_f,y_f) \,|$ can be expressed by Modulation Transfer Function, i.e., MTF:

$$OTF(x_f,y_f) = A\; MTF(x_f,y_f)\cdot\exp[-j\Phi(x_f,y_f)] \qquad \text{(II.2.5.3)}$$

MTF represents the optical intensity transfer response for a point source. The phase transmission has to be considered in an aberrated optical imaging system unless the field angle is very small[21,22]. The imaging experimental setup in this research is approximately aberration-free since the actual imaging field angle ≈ 1°. Therefore, the phase term in

equation II.2.5.3 is approximately constant 1, and then $OTF(x_f,y_f) \approx A\ MTF(x_f,y_f)$, that is only the MTF of imaging setup in my research work will be discussed in following part.

From point of view of imaging, the MTF describes the reduction of the signal modulation (contrast) as a function of the Fourier spatial frequency through an optical imaging system, which is defined as a ratio of Fourier spectrum of the image intensity distribution to the object radiance distribution:

$$MTF(x_f,y_f) = (\text{Image Contrast})/(\text{Object Contrast}) \qquad \text{(II.2.5.4)}$$

where x_f,y_f is the spatial Fourier frequency. MTF gives a measurement of change of contrast arising from the attenuation of spatial frequency component of the image signal in term of contrast (and the summation of contrast loss of all spatial frequency components result in the image distortion). For example, if $C_{Image}=0.81$, $C_{Object}=0.9$ at 5-Cycle/mm (~0.1mm resolution), and MTF = 0.9, which means 10% of the 5-Cycle/mm component of the image signal would be lost in the transmission, and the image resolution would be decreased. If the modulated signal is transmitted through an imaging optics and detected by a detector without distortion, a perfect image would be obtained, and $MTF(x_f,y_f) = 1$. In this case there is no loss of information, that is, all frequency components are transmitted without any loss. In an actual imaging experiment, the transmittance is different for different frequency components. Some of components lose, and cause the reduction of the image quality. In my research work, this difference is caused usually by the limitation of the diameter of lens, aperture and the scattering in

turbid media.

Theoretical analysis on MTF through turbid media has been obtained by Zardecki, Ishimaru and other authors in CW measurement condition[23-28]. They have shown that the image in turbid media would be seriously blurred due to the rapidly decay of the higher frequency component of MTF with turbid media existing. However, the MTF of the highly scattering media detected in the early time could be much wider than that in the late time according to the time-resolved spatial spectrum measurement[17].

II.2.5.2 Determination of MTF from measured contrast

Modulation Transfer Function of an imaging system may be determined by two calculation methods using experimental data: 1) Fourier transform of a Point Spread Function (PSF), which is actual measured intensity profile of a single-point-source image, and 2) sinusoidal transform of Contrast Transfer Function (CTF), which is a measured intensity profile of bars with different pair-line per millimeter.

In the PSF method, a Fourier transform of PSF was performance by substituting the measured image intensity profile of a signal point source into Eq.II.2.5.1 to II.2.5.3.

In the second method to determine MTF, a measured distribution of contrast as a function of the bar resolution (pair-line per millimeter) is regarded as a CTF(f)). Then the Fourier-transform-based conversion of the CTF is used to calculate MTF(f), where f_x, f_y are replaced by f for the convenience:

$$MTF(f) = \tfrac{1}{4}\pi[CTF(f) + \Sigma^{\infty}_{n=2}(-1)^n (2n-1)^{-1}CTF[(2n-1)f]$$

$$= \tfrac{1}{4}\pi[CTF(f) + 1/3\ CTF(3f) - 1/5\ CTF(5f) + \dots] \qquad \text{(II.2.5.2.1)}$$

where ¼π is a normalization factor, f represents the fundamental Fourier spatial g frequency, while (2n-1)f is the $(2n-1)^{th}$ harmonic of f. Fourier spatial frequency is defined as the pair numbers of bars per millimeter. CTF(f) is a measured contrast distribution as a function of the bar resolution in an Air Force testing target. Only odd terms are contained in Eq.II.2.5.2.1 since the expansion of a black/white bar chart contains only the odd harmonics of the fundamental frequency according to the Fourier analysis on a periodic rectangular square wave distribution.

The determination of MTF(f) can be performed by substituting the Fourier expansion of each of the CTF(f), CTF(3f), ..., CTF[(2n-1)f] into Eq.II.2.5.2.1. Where, CTF(f), CTF(3f), ..., CTF[(2n-1)f] are measured contrast values of bars with f, 3f,..., (2n-1)f pair-lines per millimeter as indicated by Air Force testing target. The Fourier expansions of the contrast of different bars are:

$$\begin{aligned}
n=1:\quad & CTF(f) = MTF(f) + \Sigma^{\infty}_{m=2}(-1)^{m+1}\,(2m-1)^{-1}MTF[(2m-1)f \\
& = MTF(f) - 1/3\ MTF(3f) + 1/5\ MTF(5f) + \ldots] \\
n=3:\quad & CTF(3f) = MTF(3f) + \Sigma^{\infty}_{m=2}(-1)^{m+1}\,(2m-1)^{-1}MTF[(2m-1)3f \\
& = MTF(3f) - 1/3\ MTF(9f) + 1/5\ MTF(15f) + \ldots] \qquad \text{(II.2.5.2.2)} \\
n=5:\quad & CTF(5f) = MTF(5f) + \Sigma^{\infty}_{m=2}(-1)^{m+1}\,(2m-1)^{-1}MTF[(2m-1)5f \\
& = MTF(5f) - 1/3\ MTF(15f) + 1/5\ MTF(25f) + \ldots]
\end{aligned}$$

.....

Substitution of these expressions in Eq.II.2.5.2.2 into Eq.II.2.5.2.1 gives MTF(f) since all the terms are canceled out to each other except the first term of n=1 expression. For the MTF(2f), MTF(3f),....., MTF(NF), the similar procedure can be carried out.

The measured distribution of contrast as a function of bar resolution, i.e., CTF, and the calculated MTF with and without turbid media for 1054nm wavelength is shown in Fig.II.2.5.1.

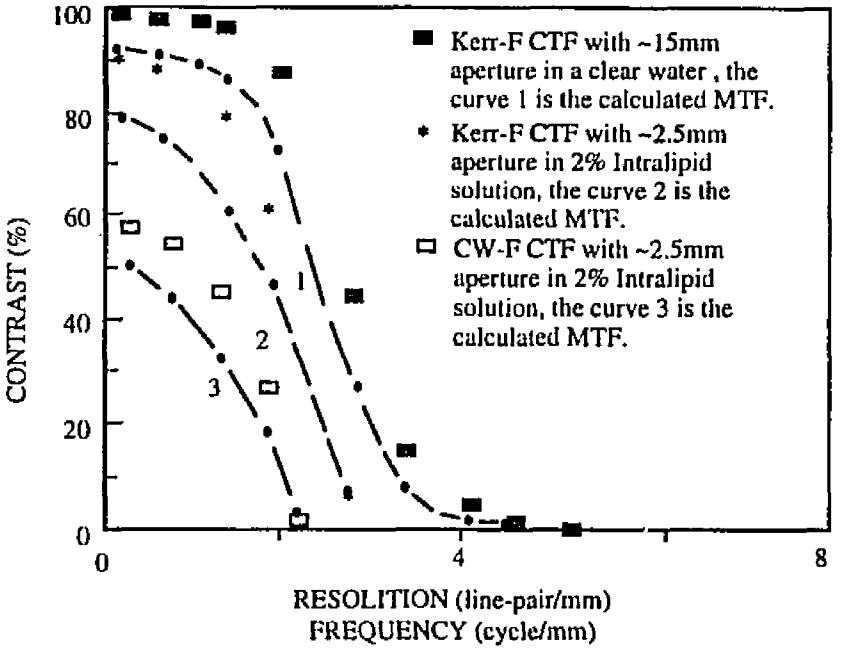

Fig.II.2.5.1. Contrast transform function of Kerr-F in a clear water (■) and 2% Intralipid solution (*); CW-F in 2% Intralipid solution (□) as a function of spatial resolution with wavelength 1054nm illumination. Curves are corresponding modulation transform functions (MTF).

In Fig.II.2.5.1, the black square data and curve 1 are the measured distribution of contrast as a function of bar resolution (CTF) detected at T=0, and the calculated MTF for a Kerr-F imaging system through a clear water with an induced aperture size of ~15mm, respectively. The cutoff frequency is about 4 pair-line/mm (corresponding to $\sim(4x2)^{-1}$ = 125μm resolution). This is the highest performance of the system at 1054nm wavelength with maximum aperture size of 15mm. The decay at the higher frequency is mainly due

to the intensity decrease of pumping laser beam at larger radii. The black-star data and curve 2 is the measured CTF and the calculated MTF of Kerr-F imaging system through a 2% diluted Intralipid solution filled in a 50mm cell with an induced aperture size of ~2.5mm detected at T=0. The contrast drops rapidly at a lower cutoff frequency of ~3 pair-line per millimeter caused by the decrease of the induced aperture to 2.5mm. The square data and the curve 3 is CTF and the calculated MTF through 50mm-thick 2% Intralipid solution by a CW-F imaging system with a aperture size ~2.5mm. Due to the effect of scattering noise in a non-time detection, the contrast decreased at the higher frequency more than Kerr-F system shown by curve 2. At the low frequency range (≤3 pair-line per millimeter), both CTF and MTF of a Kerr-F system are obviously higher than a CW-F system. The relationship between aperture size and maximum resolution can be understood using an example. The cutoff frequency f_c are defined as:

$$f_{c,c} = d/(2L_f\lambda), \text{ for coherent imaging system} \qquad \text{(II.2.5.5a)}$$

$$f_{c,i} = 2d/(2L_f\lambda) \text{ for incoherent imaging system} \qquad \text{(II.2.5.5b)}$$

In my research work, only the incoherent imaging process has been considered. Therefore, for L_f = 600mm, wavelength λ=1054nm, and aperture diameter d(mm) = 2.5mm, the f_c = 4.2 lines/mm, which corresponds to a resolution ~0.24mm. With the same conditions, the distribution of spatial resolution as a function of diameter of an aperture placed at Fourier transform spectrum plane is shown in Fig.II.2.5.2.

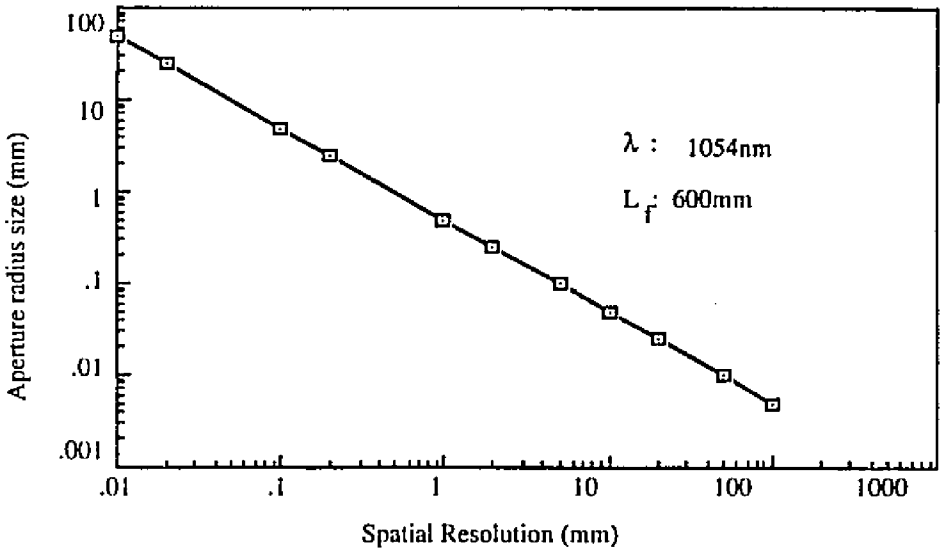

Fig.II.2.5.2 The distribution of maximum resolution as a function of diameter of an aperture placed at Fourier Transform Spectrum plane (back focal plane of Fourier transform lens).

It can be seen from Fig.II.2.5.2 that when the aperture size decreases, the maximum spatial frequency component passing the aperture (cutoff frequency), f_c, decreases, and the spatial resolution decreases. For the imaging system used in this research, f_c is ~2 line=pair/mm, which corresponds ~0.25mm resolution.

II.2.6 Optical Properties of Biomedical Media

II.2.6.1. Introduction

The scattering parameters of breast tissues and Intralipid solution will be discussed in this chapter. Knowledge of the optical properties of normal and disease breast tissues are key parameters needed for developing optical imaging techniques for mammography and tomography. There are four major optical parameters: the absorption length l_a,

transport mean free path l_t, scattering mean free path l_s, and mean cosine of scattering angle g. These parameters will be discussed.

The loss of the ballistic photons in turbid media can be estimated by scattering parameters of turbid media from Equation II.2.6.1.1:

$$I_b = I_i \exp-(w/l_a + w/l_s), \qquad \text{(II.2.6.1.1)}$$

where w is the thickness of the turbid medium, l_0 is the input photons intensity, l_a is the mean absorption length, defined as a mean distance before a photon was absorbed by turbid media, and l_s is the scattering mean free path, defined as a mean distance between two neighbor scattering events for a photon. The parameters l_a and l_s are the reciprocal of the absorption coefficient μ_a and scattering coefficient μ_s, respectively:

$$l_a = \mu_a^{-1}; \text{ and } l_s = \mu_s^{-1} \qquad \text{(II.2.6.1.2)}$$

It was found experimentally that the intensity of snake light in time Δt is:

$$I_s(\Delta t) = A \exp[-bZ/l_t] \qquad \text{(II.2.6.1.3)}$$

where b is parameter depending on Δt, $b \approx 0.8$ averaged. The snake is portion of earliest arriving photons from diffusive photons after ballistic component.

The transport path length, l_t, is defined as the distance in which a photon is fully

randomized (" forgotten its original direction of motion ") after infinitely collisions of l_s by the multi-scattering. The mean free transport path It is average distance travelled in the original direction by photons after infinite number of collisions. The relationship between l_t and l_s is related to l_t by g factor:

$$<l_t> = \Sigma\, l_t\, \mathbf{n},$$

where **n** represents the vector displacement of a photon in turbid media. To calculate the relationship:

$$<l_t> = < l_s + l_s \cos\Theta + l_s \cos^2\Theta + l_s \cos^3\Theta + \cdots + l_s \cos^n\Theta + \cdots > \quad \text{(II.2.6.1.4)}$$

From equations:

$$<l_t> = l_s/(1-<\cos\Theta>) \quad \text{(II.2.6.1.5)}$$

or $$<l_t> = l_s/(1-g), \quad \text{(II.2.6.1.6)}$$

where $g = < \cos \Theta >$ is the mean cosine value of scattering angle of photons Θ, which describes the scattering anisotropy of the turbid medium.

For a given wavelength, l_s and l_t can be calculated by:

$$l_s = (n\sigma_s)^{-1}, \text{ and } l_t = [n\sigma_s\,(1-g)]^{-1} \quad \text{(III.1.7)}$$

where n is the volume concentration, and σ_s is the scattering cross section.

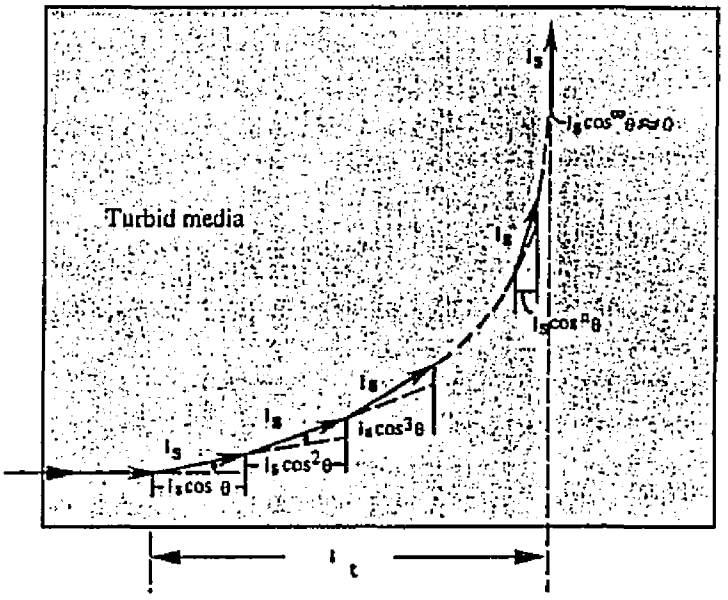

Fig.III.1.1. Mean free scattering distance l_s, mean free transport distance l_t, and mean value of cosine function of scattering angle, g, which are related from each other by:
$< l_t >=< l_s (\cos\theta + \cos^2\theta + \cos^3\theta + \ldots + \cos^n\theta + \ldots .)>= l_s/(1-<\cos\theta>) = l_s/(1-g)$

When the scattering is uniformly distributed in any directions for a single collision, $l_s \approx l_t$, and when scattering angle is highly forward-peaked $l_t >> l_s$, which means a photon would carry some information of its original motion until traveling through a much longer distance than l_s. This depends on g factor. For example, g~0 for a small particle, and g~1 for a large particle at a wavelength. The g as a function of size of particle calculated by Mie's theory, and the values of l_t to l_s are shown in Fig.II.2.6.1.2 and Fig.II.2.6.1.3, respectively. In Fig.II.2.6.1.2, it can be seen that the g factor greatly depends wavelength, especially at the diameter less than ~2 μm, which is close to the wavelength 0.527um and 1.054nm. For the Intralipid solution, the particle diameter is at order of 0.5μ, which corresponds g=~0.9 and 0.6 for 527nm and 1054nm, respectively.

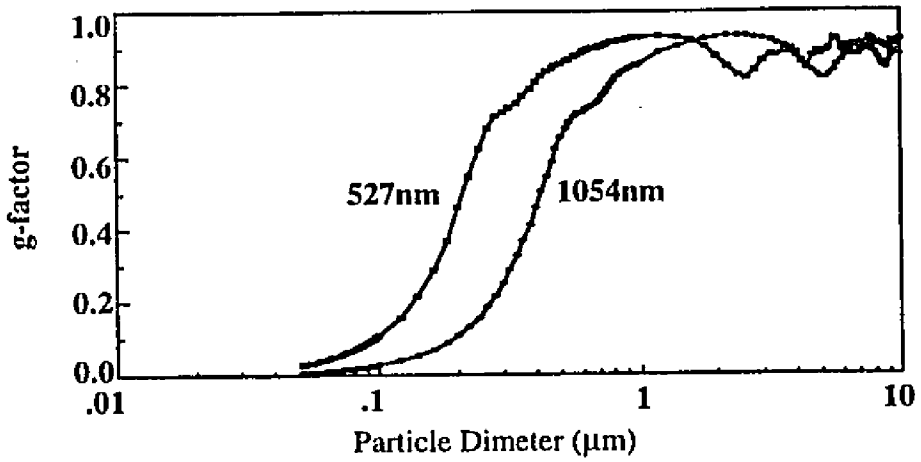

Fig.II.2.6.1.2 The calculated values of g factor as a function of particle diameter d μm).

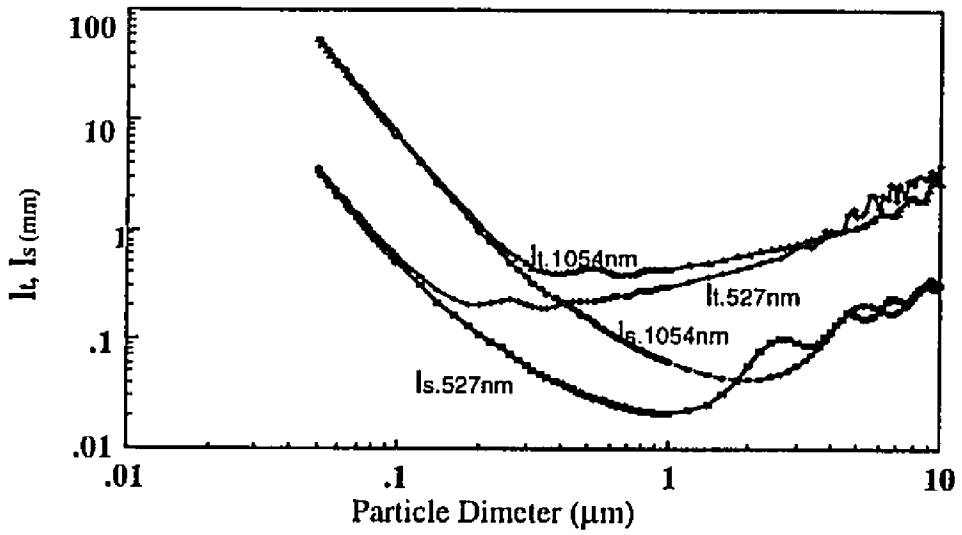

Fig.II.2.6.1.3 The values of l_t to l_s as a function of particle diameter d (μm) with a 10% diluted Polystyrene solution.

At larger diameters, the g factor oscillates about 0.85 by a deviation of ~5% for 1054nm wavelength. While g factor increases up to ~0.9 for the larger diameters for 527nm.

In Fig.II.2.6.1.3, the calculation was performed for 1% (volume density) bead solutions (10% in stock). The vertical scale is the values of l_t to l_s (mm), the horizontal scale is the diameter of particle (μm). Due to the wavelength dependence, there are smaller difference between l_t and l_s for the particles with the smaller diameter. When the

diameter increases, the difference decreases. When diameter is more than 3μm, the difference between two wavelengths are increases for both l_t and l_s.

II.2.6.2 Scattering Coefficient in Breast Tissue

Tissue scatters light strongly in the forward direction, the g value was ~0.9. A value of g=0.9 makes $l_t = 10l_s$. Intralipid suspension has been widely used as a model to simulate the bio-medical tissues. Which g is ~0.8, and 0.6 for 530nm, and 1054nm[1] respectively, and with lower absorption coefficient. For imaging experiments performed in this research, a 2% diluted solution from stock-10% Intralipid has been used to simulate a checked breast tissue. This sample was used to be simulated to a homogenized human breast. This is a assumed model for test imaging approximation. The particle size distribution of Intralipid solution is shown in Fig.II.2.6.2.1.

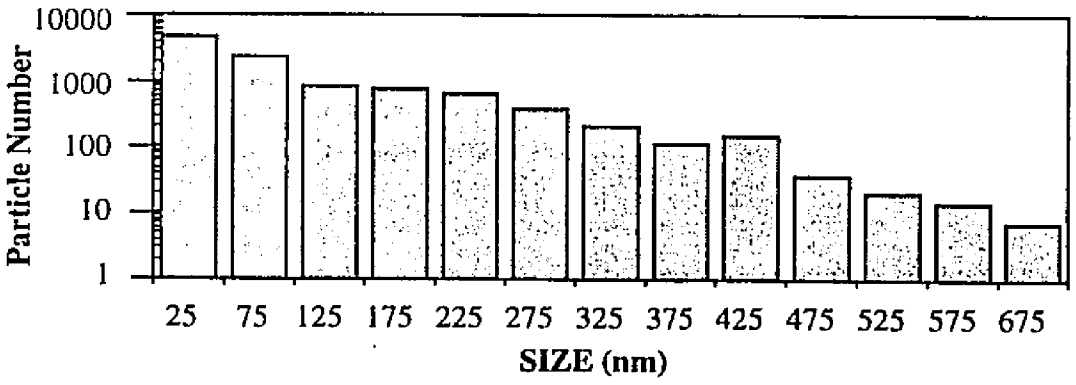

Fig.II.2.6.2.1 The particle size distribution of Intralipid solution (Mos et al, Appl. Opt. Vol.28 No.12, 1989)

Associated optical parameters of 2% Intalipid soluiton and human breast tissues at visible and IR wavelengths are shown in Table II.2.6.1. Intralipid-10% suspension

contained[30] 50-gm soya bean oil, 6-gm phospholipid, 11.25-gm glycerol, and the 2% concentration solution was done by diluting Intralipid-10% with distilled-water.

It can be seen from the data in Table II.2.6.2.1 that the transport mean free path

Tissue type and 2% Intralipid	Transport mean free path l_t (mm)	Absorption length l_a (mm)	Mean cosine value of Scattering angle, g	Mean free Path l_s (mm)	Wavelength (nm)
Glandular	1.25[2] 0.8[3]	17[2]	0.91[3]	67μm[3]	1064[2] 700[3]
Adipose (fatty breast)	0.7[1] 1.2[2] 0.77[3] 1.0[7] 1.3[7]	155[1] 10[2] 100[3] 100[7] 130[7]	0.95[3]	40±6μm[3]	620[1] 1064[2] 700[3] 633[7] 800[7]
Carcinoma	1.21[2] 0.5[3] 0.6[2] 0.54[7] 0.96[7]	230[2] 155[2] 24[7] 62.5[7]	0.88[3]		1064[2] 700[3] 620[2] 633[7] 800[7]
Benign	2.6[1]	30[1]			620[1]
Fibroadinoma	2.08[2] 1.55[2]	13[2] 100[2]			1064[2] 620[2]
2% diluted of Stock Intralipid-10%	3.0[1] 10[1] 3.4-5.0[5] 6.6[5] 5.0[5]	500[1] 500[1]	0.5[1] 0.71-0.8[5] 0.5[5] 0.64[5]	1.0[5] 3.3[5] 1.83[5] 2.3[4] 1.23[6]	620[1] 1064[1] 633[5] 1064[5] 800[5] 1054[4] 527[6]

Table II.2.6.2.1. Optical properties of human breast tissues and 2% Intralipid solution
References for the data in this table are following:
(1) F.Liu, Ph.D Thesis, CUNY, New York, 1992; B. B. Das, Ph.D Thesis, CUNY, New York, 1993. (2) Peters et al, Phys. Med. Biol, 1990, Vol.35, No.5 1371-1334 (Homogenized tissue model)[31]. (3) Key et al, Phys. Med. Biol. 1991, Vol.36, No.5 579-590[32]. (4) See next section III.2 of this chapter. (5) Staveren et al, Appl. Opt. Vol.30 No.31 1991[30]. (6) Determined by the same method as in (4), not described in III.2 of this chapter. (7) Amir H. Gandjbakhche, R. Nossal, Roya Dadmarz, Douglas Schwartzentruber, Robert F. Bonner, "Expected resolution and detectability of adenocacinoma tumors within human breast in time-resolved images", SPIE, 2387-18(1995)[33].

and absorption length of 2% diluted Intralipid solution, l_{tr} is ~3.4mm-5mm, 5mm, and 6.6mm at 630nm, 800nm, and 1064nm, respectively[30]. In the early-time-detection $l_{KF.s}$ = 2.3mm, and l_t = 4.6mm if g=~0.5 at 1054nm. The l_a = ~500mm from 620nm to

1064nm. For breast tissues, l_t = ~0.5mm - ~2.6mm at 620nm to ~1.2mm - ~2.1mm and l_a = ~100mm. For the mean cosine of scattering angle, g, there is a difference between real breast tissue and Intalipid solution. The g_{tissue} is from 0.88 - 0.95, while $g_{Intralipid}$ is from 0.5 - 0.83, which was calculated from Mie's theory (refer to Fig.II.2.6.1.2).

The optical parameters of tissues and 2% diluted Intralipid solution have been measured and estimated by us and several groups. One need to be take care of is accuracy of these values. Table II.2.6.2.2 is ours and table II.2.6.2.3 by Peters, et al, show the major measured results.

Random Media	Transport mean free path l_t (mm)		Absorption length (mm)	
	1064nm	620nm	1064nm	620nm
Benign human breast	~5.1*	2.6±0.2		30±5
Fatty human breast	~1.4*	0.7±0.1	200	155±50
Chicken breast	4.9±0.3	2.5±0.5	70±10	60±30
Chicken fat	0.74±0.1	0.6	230±70	155
Pork breast	3.5±0.5	1.2±0.2	70±10	70±8
Pork fat	0.58±0.05	0.35±0.05	400±60	300±50
Whole milk (25%)		1.0±0.1		253±50
2% solution of stock Intralipid-10%	10±1, 4.4**	3.0±0.1	500±50	500±50

Table II.2.6.2.2. Transport mean free paths and absorption lengths with standard deviations for various random media at 620nm and 1064nm measured using time-resolved transmission and diffusion approximation (F.Liu, Ph.D Thesis, CUNY, New York, 1992; B. B. Das, Ph.D Thesis, CUNY, New York, 1993). (*: Estimated by $\mu_{t\text{-IR}} \approx 0.5\mu_{t\text{-Visible}}$; **: Estimated $\mu_{t\,1054nm}$ from data of Chapter III in this thesis.)

For 2% diluted of stock Intralipid solution, the scattering mean free path at λ=1054nm $l_s \approx$ 2.2mm and $l_t \approx l_s/(1\text{-}0.5)$ = 4.4mm has measured by a K-F imaging system in this thesis (refer to Chapter III.2, Scattering Attenuation Coefficient in Intralipid Solution). This is much smaller than the l_t =10mm (by Feng Liu's Ph.D ref.) displayed in Table II.2.6.2.2.

Breast tissue consists of fat, fiber, glandular, and blood. The mean free transport path and the absorption coefficients of four different breast tissues at 1060nm, 800nm, and 625nm obtained by Peter et al are displayed in Table II.2.6.2.3. These values were estimated from experimental data using Monte Carlo numerical method.

Tissue types	1060nm		800nm		625nm	
	l_t (mm)	l_a (mm)	l_t(mm)	l_a(mm)	l_t(mm)	l_a(mm)
Normal glandular	1.25	17	0.84	25	0.60	20
Normal adipose	1.2	10	1.4	14	1.28	13
Fibroadinoma	2.08	13	1.55	100	1.04	17
Ductal cacinoma	1.21	7	1.14	33	0.79	8

Table II.2.6.2.3. Transport mean free paths and absorption lengths with standard deviations for various random media at 620nm and 1064nm measured by Peters et. al. Phys. Med. Biol. 1990, Vol. 35, No.9 1317-1334 (These samples were compressed homogenized and chopped up), which I believe have more scattering effect than whole breast. The number of $l_t(\lambda)$ was from 1 to 3mm depending on λ.

The l_t for fat and glandular tissue are listed in Table.II.6.2.3. Some values (for instance l_t of adipose (fat) in Table II.2.6.2.3 are different from that in Table II.2.6.2.2. The main reason for which is that samples used by Peters were compressed homogenized tissues, in which the sample no longer possessed any natural structure. The value in Table II.2.6.2 were obtained from samples in vitro. It can be seen from Table II.2.6.3 that the mean free transport path of the normal glandular is strongly dependent of wavelength, which falls with the increase of the wavelength.

The absorption of different chromophores in tissue, such as H_2O, and HbO_2b as a function of wavelength is shown in Fig.II.2.6.2.4. The curves in Fig.II.2.6.2.4 shows the range from ~700nm to 1350nm may be the better wavelength band for the optical mammography since there is lower absorption by H_2O, which is a major component of

tissues. Attenuation curves of a distill water and the 2% diluted Intralipid in stock

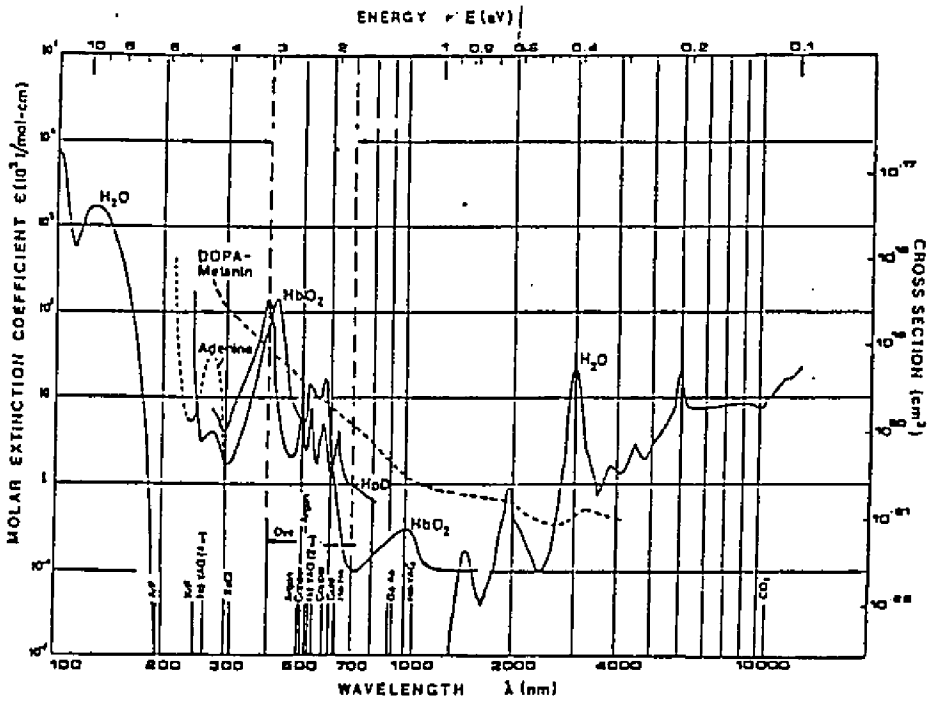

Fig.II.2.6.2.4 Absorption curves for tissue constituents (Svanberg, *Atomic and Molecular Spectroscopy, Springer Verlage Published*, 1991)

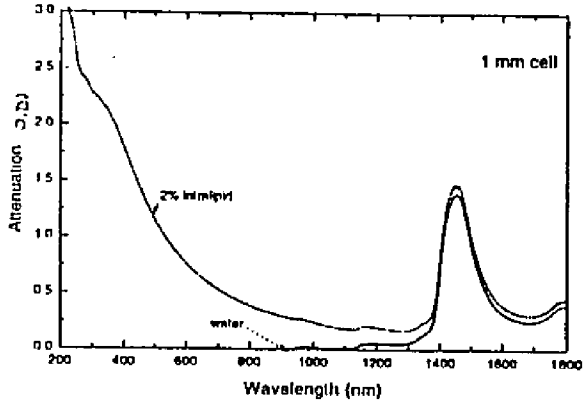

Fig.II.2.6.2.5 Attenuation of water and 2% diluted Intralipid.

solution in 1mm-thick cell are shown in Fig.II.2.6.2.5. The curve shows that the attenuation ratio for wavelength greater was than 800nm. A peak at~1370nm was dominated by water in Intralipid. In which range, the absorption of water appeared at ~900nm, ~1200nm and longer. The attenuation for 0.5mm-thick motor oil (10W40) is shown in Fig.II.2.6.2.6. These are absorption peaks at ~1200nm, which may help in defining the state of tissues. The total attenuation

coefficient for 5mm-thick fatty breast tissue, and fibroglandular tissue are shown in Fig.II.2.6.2.7. They show there is no considerable absorption peak caused by water because the samples are dry. The transmission for 5mm-thick carcinoma (thin curve) and the surrounding tissue (solid curve) are shown in Fig.II.2.6.2.8[32]. It shows that the attenuations at range from 500nm - 600nm were caused by oxyhaemoglobin (around 540, 577nm), and deoxyhaemoglobin (555nm), where there is a larger difference between carcinoma and tissue. In the longer visible and IR wavelengths, the difference is lessened, where the absorption of water dominated the attenuation (at ~1200nm, ~1450nm). These chromophores may play a important role to separate cancer from and normal tissues.

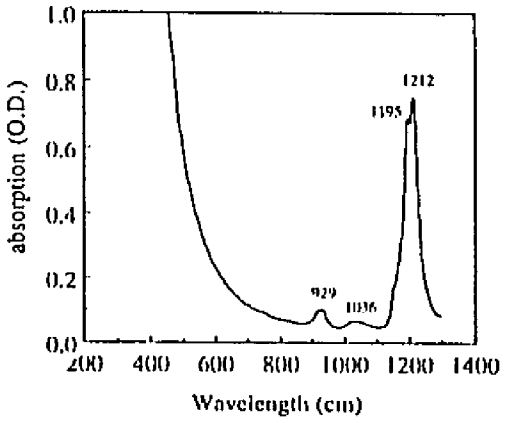

Fig.II.2.6.2.6 Attenuation of motor oil

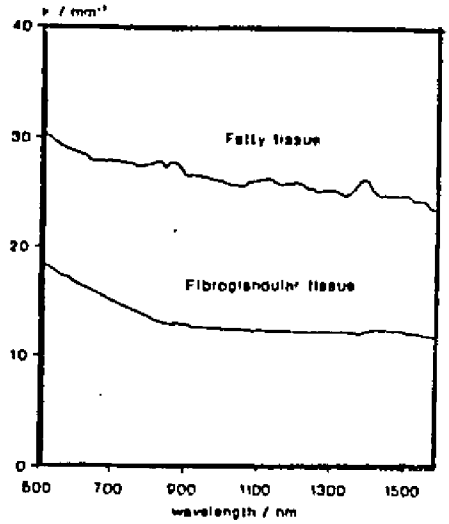

Fig.II.2.6.2.7 Attenuation of fatty tissue and fibroglandular (Key et al, Ref.32).

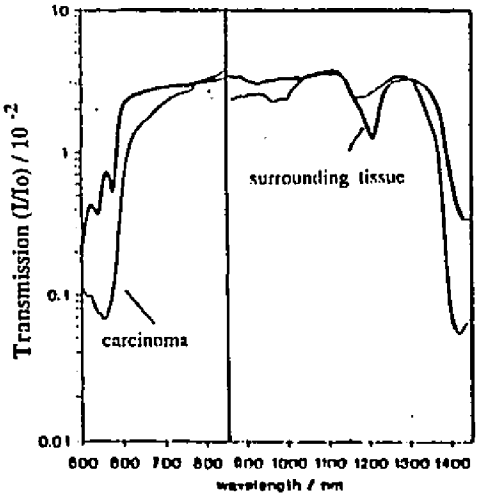

Fig.II.2.6.2.8 Transmission of carcinoma and surrounding tissue (Key et al, Ref.32).

II.2.7 Detection Sensitivity

The detection sensitivity is a first important parameter for an imaging system. Which determines the minimum detectable signal level and the maximum detectable thickness (depth) of samples. In practical imaging applications, such as biomedical diagnosis, the illumination energy is usually limited by the safety requirements and the maximum illumination power of light source, which results in a limitation of the maximum number of transmitted photons. in this section, the these key problems will be discussed.

II.2.7.1 Sensitivity of Image Detector

The minimum detectable photon numbers of the detector of the imaging system is determined for the maximum sensitivity. Two types of detectors have been used in this research: (1) Intensified CCD camera, and (2) Cooled CCD detector.

(1) Intensified CCD camera

The optical magnification of the intensifier is of the maximum ~$4x10^3$. The wave length response is ~80% at 527nm and ~10% in 900nm. The pixel area is ~$17x17\mu m^2$. The minimum detection level for VIRO-Pulnix ICCD assembly provided by the specification is ~ 1 Lux/cm^2, or $3.3x10^{-6}$lux/ pixel. The measured value of the detectable optical energy is ~$1x10^{-8}$ Joule per cm^2, or $3x10^{-14}$Joul/pixle. The dark noise level is ~1 count. The maximum gray level of bits is $2^8 = 256$ with the 640 x 480 = 307200 pixels in total chip area ~12mmx9mm.

The ICCD is used in the detection at visible wavelength due to the IR response

limitation of the intensifier. In my research, the ICCD camera has been used in imaging at the 527nm wavelength. Since the effect of the thermal noise in the intensifier, the maximum detectable thickness is lower than a cooled CCD camera. The noise data has not been provided by the manufacture. The overall noise background for intensified CCD camera was tested to be ~2 counts when the working time of the CCD camera was not over ~5 seconds.

(2) Cooled CCD detector

The cooled CCD detector works in -45 C° (Centigrade) with the maximum readout gray level of bits 2^{16} = 65,536. The measured dark-noise-back-ground is ~1030 counts over detection area. Because of the dark noise is quiet stable by ≈±1 count, the minimum value of the effectively readout is ~2 count. The pixel size (the maximum spatial resolving distance of the CCD chip) is ~15umx15um, and maximum detection area is ~8mmx8mm. The total number of pixels is 512x512 = 262,144. The wavelength response is ~ 55% at 527nm and ~8% at 1054nm. The minimum detectable photon energy provided from Photometrix specification is:

2 count (Effective readout) x $0.3x10^{-18}$ Joule (photon energy) / 20 (photons) / 8%

= ~$1.5x10^{-16}$ joule /pixel at 1054nm, which corresponds to a 500 photons/pixel.

The measured results is ~$2.4x10^{-16}$J/pixel, in term of the minimum number of photons, this corresponds to that ~800 photons can be detected for each pixel of CCD chip at 1054nm wavelength. For a turbid medium with l_t = 2mm and thickness of 50mm and 1J/cm^2 illumination, the transmitted energy is ~10^{-11}J. If imaging magnification is 1:1 and pixel size is 20μm, the energy collected at each pixel is $4x10^{-15}$J/pixel, which

corresponds to ~1300 photons, and 3 count.

II.2.7.2 Photon Count for One CCD Pixel

The early-arriving ballistic/snake photons are to be used to form a clear image. The number of the ballistic/snake transmitted through tissue sample can estimated by[34]:

$$I(\Delta t) = I_0 A \exp[-bd/l_t] \qquad \text{(II.2.7.2.1)}$$

where Δt is a opening duration of a time gate; parameters $A = 10^{-4}$ and $b = 0.8$ for Δt = 50ps, tissue thickness d= 50mm. Under the illumination of the laser pulses with 5mJ at 1000Hz, in 60 second, the number of photons transmitted through 50mmx50mmx50mm-thick random media(12J/cm^2) with three different transport mean free paths are displayed in Table II.2.7.2.1. The sizes of illuminated area of object and image on CCD chip are assumed as 25cmx25cm and 10mmx10mm, respectively. The pixel size of CCD chip is ~20μm. Therefore, the spatial resolution is 5cm/(10mm/20μm) =0.1mm. The experimental setup is shown in Fig.II.2.7.2.1.

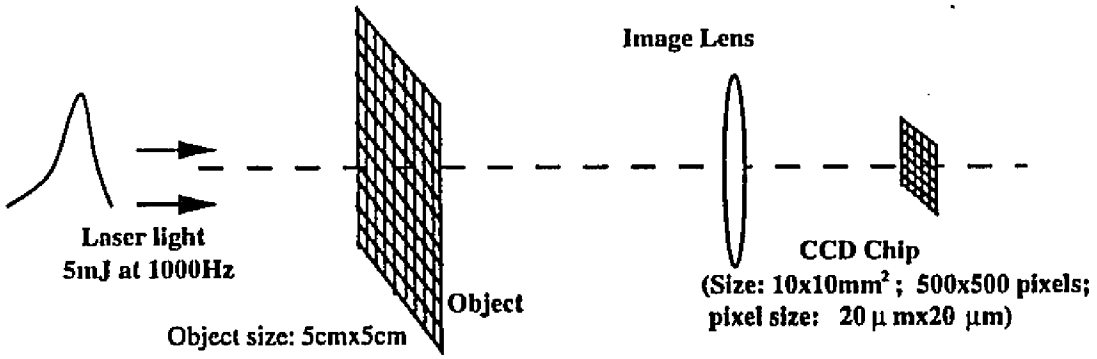

Fig.II.2.7.2.1 The imaging set up to calculate the photon number detected at each pixel of CCD chip.

In Fig.II.2.7.2.1, the total energy of illumination laser at 1054nm is 5mJ at 1000 Hz for 60 seconds. The transverse area of an object illuminated by laser light is 5cmx5cm. The imaging magnification factor is M = (image size/object size) = 0.2, that is, the image that is the larger image size, will produce the better resolution when pixel size is known. size is de-magnified by 5-times. Without limitation from imaging optics, the maximum spatial resolution is determined by the pixel-size of CCD chip. Therefore, the bigger M, On the other side, when the M is smaller, that is, the image size is smaller, the image signal intensity will be higher (equivalent to the higher sensitivity) since more photons will be concentrate in each pixel, which can improve the SNR of the image. In this calculation, two different resolution, 0.1mm, and 1mm (which corresponds to the image size of $10x10mm^2$, and $1x1mm^2$ at CCD chip, respectively), will be set to determine photon numbers.

Taking a detection time period of 60 seconds, the detectable photon number per CCD pixel for 1054nm wavelength can be calculated using Eq.II.2.7.2.1:

$$n_{1054nm}(60\ \text{seconds}) = 12Jcm^{-2}\cdot 3\cdot 10^{18}J^{-1}\cdot 10^{-2}\cdot 10^{-4}\cdot \exp[-0.8\cdot 50mm/l_t mm]$$

where, l_t = 1.5mm, 2mm, and 4mm, respectively. The results are shown in Table II.2.7.2.1.

Resolution	Number of Photons Detected Per Pixel		
	l_t: 1.5mm	l_t: 2mm	l_t: 4mm
0.1mm	1.92	$1.54x10^3$	$3.43x10^7$
1.0mm	192	$1.54x10^5$	$3.43x10^9$

Table II.2.7.2.1 Numbers of transmitted photons through 50mm random media with l_t =1.5, 2, and 4mm.

The data in Table II.2.7.2.1 represents maximum detectable photon number per pixel of

a CCD chip. For 1mm spatial resolution and l_t > 1.5mm, the result gives hope for time-resolved transillumination detection technique for breast scanning. To estimate the actual CCD output image signal level, the quantum efficiency and the CCD sensitivity have to be taken into account. For a Photometrix CH250 CCD head, the quantum efficiency is ~5% at 1054nm and ~20 photons/pixel produce one count signal level with gain ~1.0. In actual measurement, the Kerr efficiency of ~5-10% has to be taken into account to estimate the maximum sensitivity. For tissue data is displayed in Table II.2.6.1, the detectable photon number for the same conditions shown in Fig.II.2.7.2.1 for 60 second are shown in Table II.2.7.2.2.

50-mm Thick Random Media	Detectable Photon Number Per Pixel for 1-mm Resolution			
	1064nm		620nm	
	l_t	Photon Number	l_t	Photon Number
Benign human breast	~5.1*	$1.4x10^{10}$	2.6	$4.5x10^{7}$
Fatty human breast	~1.4*	14	0.7	0
Chicken breast	4.9	$1.02x10^{10}$	2.5	$2.43x10^{6}$
Chicken fat	0.74	0	0.6	0
Pork breast	3.5	$5.28x10^{8}$	1.2	0
Pork fat	0.58	0	0.35	0
Whole milk (25%)			1.0	0
2% solution of stock Intralipid-10%	10, 4.4**	$6.6x10^{11}$ $6x10^{9}$	3.0	$3.48x10^{7}$

Table II.2.7.2.2 The numerical results of the number of photons transmitted through 50-mm thick tissue sample with the transport mean free path lengths at 620nm, and 1064nm displayed in Table II.2.6.2.2. The photon number for 1-J at 620nm, and 1064nm are $1.8x10^{18}$, and $3x10^{18}$, respectively. The thickness of tissue is 50mm. The achieved spatial resolution is 1-mm. Input ligh energy is 5mJ/cm^2 at 1000Hz for 60seconds. (*: Estimated by $\mu_{t\text{-IR}} \approx 0.5\mu_{t\text{-Visible}}$; **: Estimated $\mu_{t,1054nm}$ from data of Chapter III in this thesis.)

For different types of 50-mm-thick tissue using Peter's data of l_t shown in Table II.2.6.2.2, the number of detectable photons per pixel of CCD chip in an early-60-second

period can be calculated using Equation II.2.7.2.1. The results are shown in Table II.2.7.2.3. In the calculation, all simulation conditions are same as that discussed in Fig.II.2.7.2.1.

Tissue types (50mm-Thick)	Number of Detected Photons Per Piexl (1-mm Resolution)					
	1060 nm		800 nm		620 nm	
	l_t (mm)	Photon Number	l_t(mm)	Photon Number	l_t(mm)	Photon Number
Normal glandular	1.25	0.46	0.84	0	0.6	0
Normal adipose	1.2	0.12	1.4	10.6	1.28	0.58
Fibroadenoma	2.08	1.6×10^{5}	1.55	168	1.04	0
Ductal carcinoma	1.21	0.16	1.14	0	0.79	0

Table II.2.7.2.3 The numerical results of the number of photons transmitted through 50-mm thick tissue sample with the transport mean free path lengths at 620nm, 800nm, and 1064nm displayed in Table II.2.6.2.3. The photon number for 1-J at 620nm, 800nm, and 1064nm are 1.8×10^{18}, 2.265×10^{18}, and 3×10^{18}, respectively. The thickness of tissue is 50mm. The achieved spatial resolution is 1-mm. Input ligh energy is $5mJ/cm^2$ at 1000Hz for 60seconds. The values of l_t were from Peter's data which I believe are smaller than true values since these samples were compressed homogenized and chopped up.

II.3 Multi-stage Optical Kerr Gate Imaging Arrangements

II.3.1. Introduction

Optical Kerr gate[12,35,38,39] has been used as a simple ultrafast switch to measure the ultrafast events and relaxation processes in biology, chemistry, and physics. In some cases, it can be used as a fast shutter for digital communication[39] and computation[40].

For a single-stage optical Kerr gate[12,35,37,38] (SOKG), which uses a pair of plastic sheet polarizers, the S/N ratio ~2×10^{3} and the gate-opening time~8-16 picoseconds for the

different pumping power has been commonly obtained from a 10 picosecond mode-locked glass laser. However, in some applications, such as time-gated optical imaging[21,41-44] in biological and medical samples, the higher dynamic range $>10^{10}$ and the shorter opening time ~1ps are needed.[44,45] In this paper, we present the experiments results and analysis of a double-stage optical Kerr gate (DOKG) system for the improvement of the dynamic range, S/N and temporal behavior. The shorter gating time was achieved in a DOKG, due to the non-synchronized overlapping of two independent delay times: t_1 and t_2. These two gating times can be either the same or different. When $t_1 = t_2$, it is called the synchronized double-stage optical Kerr (SDOKG), and when $t_1 = t_2$, it is called the non-synchronized double-stage optical Kerr gate (NDOKG). In both SDOKG and NDOKG, ~500 times S/N ratio improvement than that of a SOKG system has been achieved. In addition, for NDOKG system, FWHM ~3ps shutter time can be obtained.

For a single-stage optical Kerr gate (SOKG), which uses a pair of Calcite polarizes, the S/N ratio $\sim 2\times10^5$ and the gate-opening time~8-16 picoseconds for the different pumping power has been commonly obtained from a 10 picosecond mode-locked glass laser. In double-stage Kerr gate system, there are two independent delay times: t_1 and t_2, which correspond to gated portions of probing signal in two stages, respectively. These two delay times can be either the same, which mean the same portion is gated twice, or different, which means two gated portions are not same (they can be overlapped in part, or completely separated, based on how different the two gating pulse arrive times are). When $t_1 = t_2$, it is called the synchronized double-stage optical Kerr (SDOKG). When $t_1 = t_2$, it is called the non-synchronized double-stage optical Kerr gate (NDOKG). In

comparison to a single-stage Kerr gate, >3 times reduction of the gate-opening and 500 times improvement in signal-to-noise ratio has been achieved in the double-stage Kerr gate.

II.3.2 Analysis of DOKG

An picosecond optical Kerr gate is a time-varying nonlinear device, in which, the optical transmission characteristic is dominated by the interaction of the gating pulse and Kerr active medium. When an intensive linearly polarized laser pulse passed through a Kerr active medium, the difference of the induced indices of refraction parallel and perpendicular to the polarization direction of the orienting laser field can be written as[36-39]:

$$\delta n(t) = n_2^e \langle E_g 2(t) \rangle + (n_2^0/\tau_0) \cdot \int \langle E_g^2(t) \rangle \exp(-(t-\tau)/\tau_0) d\tau \qquad (II.3.2.1)$$

where $\langle E_g^2(t) \rangle$ is the time averaged gating laser pulse intensity function which is assumed to be a Gaussian temporal profile $\langle E_g^2(t) \rangle = 1/2\ E_{g0}^2 \exp(-t^2/\tau_g^2)$ in this paper, τ_g is the pulse width defined as e^{-1} decay time of the pulse envelope, n_2^e is the fast nonlinear refractive index caused by fast relaxation mechanisms such as electron cloud distortion; and n_2^o is the slow nonlinear refractive index[46-48] caused by a slow (molecular) relaxation time τ_0. Using a slow detector, the transmitted signal of a probing pulse $\langle E_1^2(t) \rangle = 1/2\ E_{10}^2 \exp(-(t^2/\tau_1^2))$ through a Kerr gate can be expressed as a function of delayed gating time τ_D:

$$S(\tau_D) = S_I^{-1} \int <E_I^2(t-\tau_D)> T^{s,d}(t)\, dt \qquad (II.3.2.2)$$

where $T^{s,d}(t)$ is an optical transfer function with the superscript s,d correspond to a SOKG system $T^{s}(t)=\sin^2(\pi L/\lambda\ \delta n(t))$ and a DOKG system $T^{d}(t)=\sin^2(\pi L_1/\lambda\ \delta n(t_1))\ \sin^2(\pi L_2/\lambda\ \delta n(t_2))$,

respectively (refer to Appendix). $S_I = \int <E_I^2(t)> dt$ is the normalized probing pulse intensity ; τ_D is the delayed gating time between the gating pulse and probing pulse; τ_I is the e^{-1} decay time of the probing pulse. Other parameters n_2^0, n_2^e, τ_0 and L are set to be the same for both Kerr cells.

When the intensity increased, the transfer function broadened and became oscillatory[45,48] for both SOKG and DOKG, however, it narrowed for NDOKG. This due to the non-synchronous overlapping of two induced phase shift in the Kerr cell. The partial overlapped opening time of these two gates lead to a significant reduction of the gating time. The shape, width and the transmission efficiency of the transmitted pulse signal are all the transferring functions T(t). Using a slow response detector, the gating and probing pulses are convoluted through the integration of Eq.II.3.2.2 at a particular delay time τ_D.

II.3.3 Experimental Method and Setup

Schematic diagrams of experimental setup of DOKG and a conventional SOKG are shown in Fig.II.3.3.1. A laser pulse train from a mode-locked Nd:glass laser was used to study the gate. A mode-lock Nd:glass laser with wavelength 1054nm and 10ps

duration was used as the orienting light source. The peak intensity for the Kerr gating pulse was adjusted from ~0.1 to ~2GW/cm^2. A potassium dihydrogen phosphate crystal was used for the SHG. The average pulse duration was obtained by using streak camera for 527nm (Ref.13) and the two-photon absorption induced fluorescence[46] for 1054nm. active medium carbon disulfide liquid in an 10mm thick optical glass cell was situated between a polarizer and a analyser (Poloroid HN22). The 1054nm beam was splitted by a half-reflection mirror into two orienting beams and passed through these two Kerr cells with independent time controls. The whole system was controlled by a PC computer,

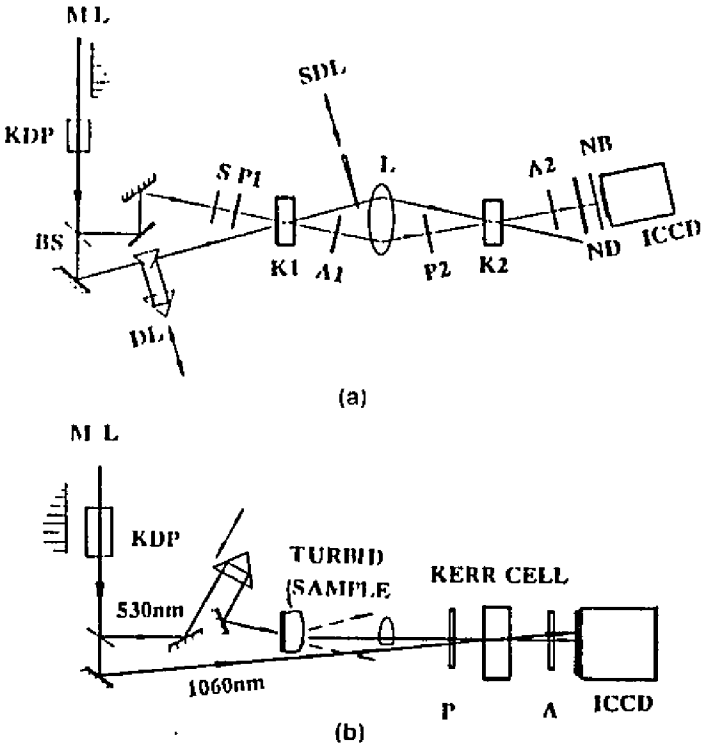

Fig.II.3.3.1 (a) Experimental setup of DOKG. A laser-pulse train from a mode-locked Nd:glass laser was used to study the gate. The laser-energy fluctuation was ~5% from shot to shot. ML, mode=locked picosecond laser-pulse train; KDP, potassium dihydrate phosphate crystal for a SHG pulse; BS, beam splitter; S, sample; DL, delay line; P1, polarizer oriented at +45° and -45° with respect to the polarization of the 527-nm beam, respectively. A1, A2, analyzer oriented at -45° and +45° with respect to the polarization of the 527-nm beam, respectively. K1, K2, 1-cm long CS_2 Kerr cell; L, lens; SDL, stacked glass slides for the time delay control of the second stage; ND, neutral density filters; narrow-band filters, ICCD, image-intensified CCD camera detector with ~10^4 gain. (b) A SOKG set up.

which was triggered by the laser firing signal from the laser power supply. The transmitted 527nm signal pulse was recorded by an ICCD camera. From which, the output signal was send to a PC computer to be processed and displayed.

The signal profile was obtained by sampling the delay time τ_D. Each sampling step was 0.25mm (~1.67ps). Each data point was obtained by averaging of ~6-10 shots and calibrated for the nonlinear response of ICCD camera and the power fluctuation of the The temporal distribution of the 527nm can be fitted as a Gaussian function[44]. The Kerr incident laser pulse. The maximum overall system S/N is defined to be $S(\tau_D=0)/S(\tau_D=\infty)$, where $S(\tau_D=0)$ is the gated signal when the orienting and the probing pulses met in the Kerr cell at the same time, and $S(\tau_D=\infty)$ is the gated signal when the arrival time for the orienting and probing pulses is different by infinite time from each other. The system extinction ratio, ε, was defined as $I_{parallel}$(polarizer and analyzer were oriented at the same direction) / I_{cross} (polarizer and analyzer were crossed). ε represents the ability to reject the leakage noise. For a pair of crossed HN22 polarizers, the measured ε was ~2.5×10^3 for (633nm and 527nm). In the SOKG, the measured leakage intensity readout was adjusted to be ~ 2±1 counts (~5×10^{-9}J) and the camera background noise was ~ 1±1 counts. In the DOKG, the maximum ε was ~7×10^5 at the input total 527nm pulse energy to be ~1mJ.

The laser-energy fluctuation was ~5% from shot to shot. ML, mode-locked laser-pulse train; KDP, potassium dihydrate phosphate crystal for a second-harmonic-generation pulse; BS, beam splitter; S, sample; DL, delay line; P1,P2, polarizers oriented at +45 and -45 with respect to the polarization of the 527-nm beam, respectively; A1,A2, analyzers

oriented at -45 and +45 with respect to the polarization of 527-nm beam, respectively; K1,K2, 1-cm-long CS_2 Kerr cells; L, lens; SDL, stacked glass slides for the time delay control of the second stage; ND, neutral-density filters; NB, narrow-band filters; ICCD, imaging intensified CCD camera detector with ~10^4 gain.

II.3.4 Experimental Results and Discussion

Fig.II.3.4.1 displays the typical measured transmitted signal as a function of the

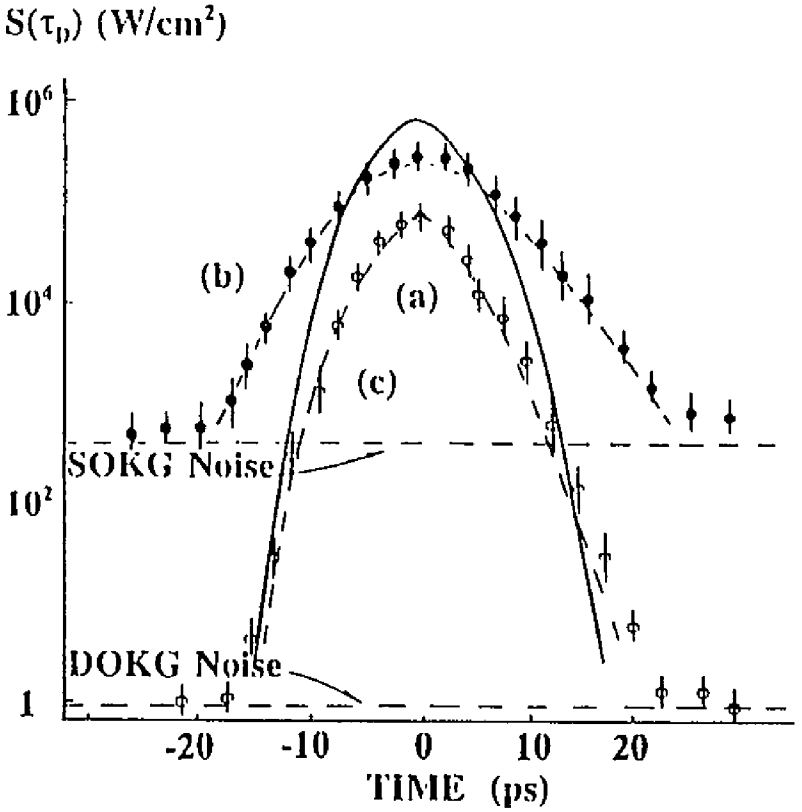

Fig.II.3.4.1. Gated transmitted signals as a function of gating time τ_D for NDOKG (a) and SOKG (b). The vertical scale is the transmitted probing beam intensity, and the horizontal scale is the delayed gating time in ps. The time zero was chosen to be the maximum transmitted signal, which was an ~2 ps difference between SOKG and NDOKG. The standard deviation for the measured signal was ~ 10%. For SOKG the gating intensity was ~ 0.2GW/cm², the exp(-1)decay time was ~ 8 ps, the leaking noise level was ~ 700, and the maximum transmission efficiency was ~60%. For NDOKG the gating intensity of the first Kerr cell was ~ 1.2 GW/cm², and the second Kerr cell was 11 ps, the exp(-1) decay time was ~ 5.6 ps, and the maximum transmission efficiency was ~10%. The noise level of DOKG was ~2 counts at the input probing pulse intensity of ~10^6W/cm². The solid curve (a) is calculated from a laser-pulse profile that is a Gaussian function, 10^6V/cm² exp(-t^2/δ^2). The dashed curves (b) and (c) are calculated from Eq.(2) for SOKG and NDOKG, respectively. To align the peak transmitted signals of (a), (b), and (c), the time axis was shifted for (c) by ~5.5 ps.

gating time from a SOKG and a DOKG. Due to the limitation of 256 counts dynamic region of the detection system used, some of the transmitted signal were attenuated by $4x10^3$ times. The flat broken line represents the noise level caused by the light leaking in the SOKG system. The noise level for the DOKG, plotted at the ground line in Fig.II.3.4.1, was very small. The measured S/N for the SOKG and DOKG were $1.5x10^3$ and $5x10^5$ respectively. The e^{-1} decay time width of the gated pulse signal as a function of the orienting intensity. o (SOKG), o (SDOKG) and x (NDOKG) are experimental results . The experimental results of NDOKG were detected at four different δt: 4ps ,9ps, 12ps and 16ps. (a) , (b) and (c) are calculated curves for SOKG, SDOKG and NDOKG, using Eq.II.3.2.2, respectively.

In Fig.II.3.4.1, signal profiles is a function of gating time τ_D for a SOKG(o) and a DOKG(o). The vertical scale is the transmitted probing beam intensity and the horizontal scale is the delayed gating time in picosecond. The standard deviation for the measured signal was ~10%. For SOKG, the gating intensity was ~0.2 GW/cm^2, e^{-1} decay time was ~16ps and the leaking noise level was ~700; and the maximum transmission efficiency for was ~60%. For NDOKG, the gating intensity of the first Kerr cell was ~1.2 GW/cm^2, the second Kerr cell was ~ 0.8 GW/cm^2. the gating time difference δt of two Kerr gates was ~12ps, the e^{-1} decay time width was ~11ps, the maximum transmission efficiency was ~10%. The leaking noise level of DOKG was 2±1 counts (ICCD camera internal noise) at the input probing pulse intensity of ~10^6 W/cm^2. The solid line of (a) is a calculated curve of laser pulse which is a Gaussian function: 10^6 V/cm^2 $\exp(-t^2/5^2)$. The

$\tau_g = \tau_1$ =5ps, τ_0 = 1.8ps, n_2^0 =1.6x10^{-11} esu, n_2^e = 0.25n_1^0, $<E_g^2(t)>$=~0.2GW/cm^2, $<E_{g,1}^2(t)>$=~1.4GW/cm^2, $<E_{g,2}^2(t)>$=~0.9GW/cm^2. Background noise level of SOKG =~700, Background noise of DOKG =~1. Due to the nonzero τ_0, the transmitted pulse profiles were asymmetry with a slightly longer delay at the positive time region.)

The calculated e^{-1} gating time widths of the gated signals from SOKG, SDOKG and NDOKG as a function of the gating pulse intensity are shown in Fig.II.3.4.2. For NDOKG, measured gating width from four gating time difference, δt =4 ps, 9 ps, 12ps

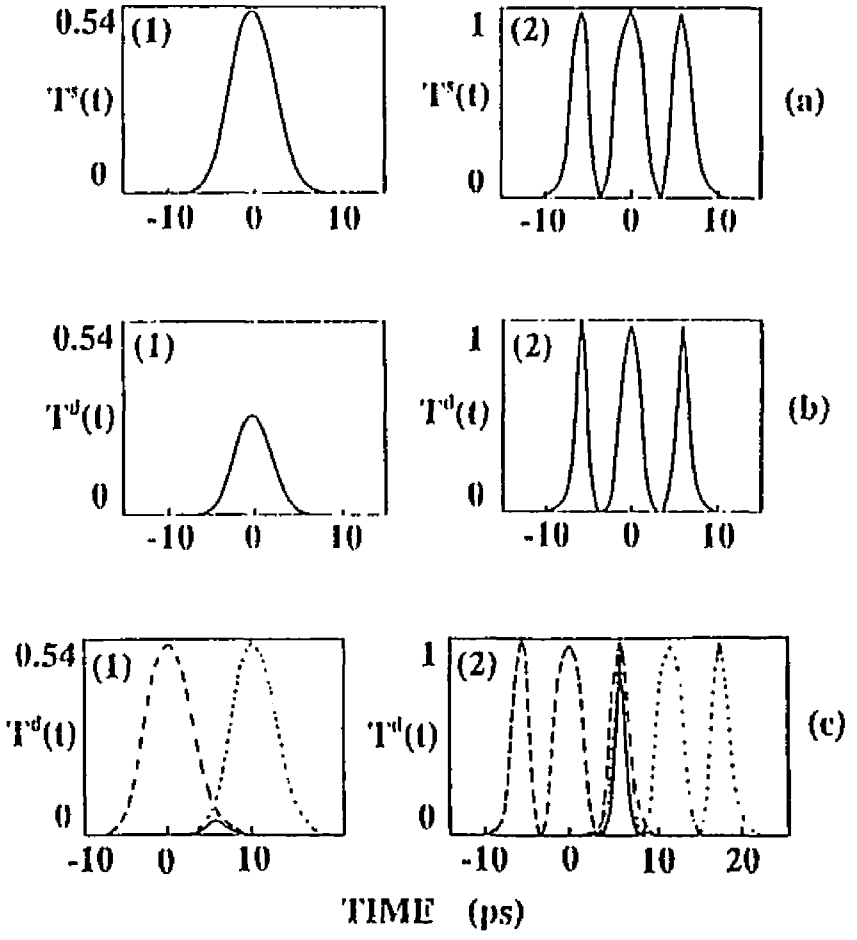

Fig.II.3.4.2. Calculated temporal profiles (solid curves) of optical transfer function T(t) from Eg.II.3.2.2 at two gating intensities: (1) 270MW/cm^2 and (2) 1.6GW/cm^2 for different gates: (a)n SOKG, (b) SDOKG, and (c) NDOKG with τ_g - 5ps, τ_0 = 1.8ps, n_2^0 = 1.6x10^{-11} esu and n_2^e = 0.25 n_2^0; δt = 11 ps for NDOKG. The dashed and dashed-dotted curves in (c) are the transfer functions from the individual gates 1 and 2, respectively. The peak of the NDOKG shifts to 5.5 ps, which is equal to one half of δt (=11 ps).

and 16ps are displayed. In all cases, the gating time width of DOKG is shorter than that of SOKG. The salient feature of the measurements indicated that when the gating pulse became more intensive, e^{-1} gating time width increased for both SOKG and SDOKG, but decreased for NDOKG under a proper selection of δt. When the intensity was ~1 GW/cm^2, e^{-1} width was ~27ps for SOKG, ~24ps for SDOKG. When the gating pulse intensity was ~1.2 GW/cm^2 for the first Kerr cell and ~0.8 GW/cm^2 for the second Kerr cell with δt~4ps, 9ps, ~12ps and 16ps e^{-1} decay time width of gated signal was obtained from NDOKG.

Calculated temporal profiles of optical transfer function T(t) from Eq.II.3.2.2 at two orienting intensities (a) SOKG, (b) SDOKG and (c) NDOKG when τ_g = 5ps, relaxation time of CS_2 τ_0 =1.8ps, n_2^0 = 1.6X10^{-11} esu and $n_2^c = 0.25n_2^0$. In (a) SOKG and (b) SDOKG, three different gating intensities were used: (1) 0.2 GW/cm^2; (2) 0.45 GW/cm^2 and (3) 0.7 GW/cm^2. In (c) NDOKG, the corresponding orienting pulse intensity and δts are (1) 0.6 GW/cm^2, 4ps; (2) 0.8 GW/cm^2, 7ps; (3) 1.2 GW/cm^2, 9ps.

Fig.II.3.4.3 shows the calculated transfer function profiles of SOKG, SDOKG, NDOKG caused by the 1054nm orienting pulse at three different intensities in a 1cm long CS_2 medium. When the intensity increased, the transfer function became broaden and oscillating[36,47,48] for both SOKG and DOKG, but narrowed for NDOKG. This dramatic change of the temporal distribution of T(t) in a NDOKG due to the non-synchronized overlapping of two induced phase shift in Kerr cell. The partial overlapped opening time of these two gates lead the significant reduction of the gating time as shown in Fig.II.3.4.3c and Fig.II.3.4.2. The T(t) can strongly influence the shape, width and the

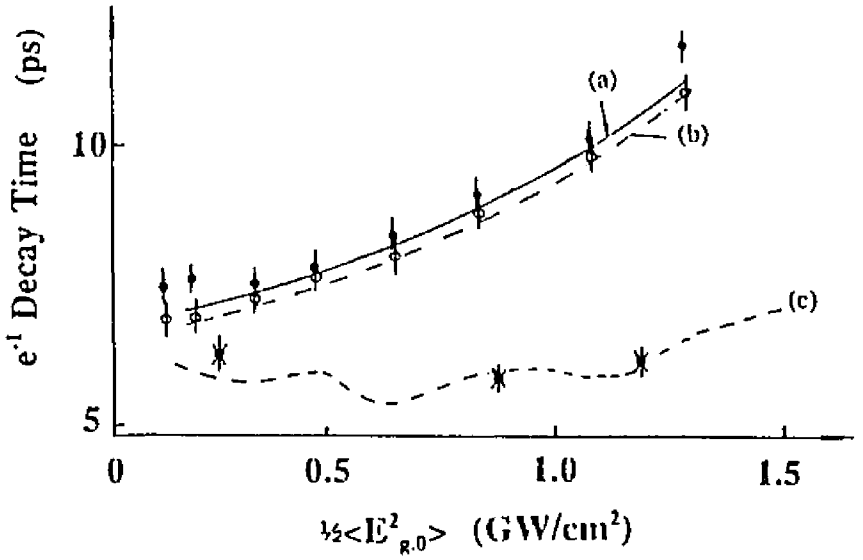

Fig.II.3.4.3. Experimental results for the measured convoluted exp(-1) decay time of the gated transmitted pulse signal as a function of the gating intensity: o, SOKG; o, SDOKG; X, NDOKG (δt = 11 ps). (a), (b), (c): calculated curves from Eq.(2) for SOKG, SDOKG, and NDOKG (δt = 11 ps, respectively.)

transmission efficiency of the transmitted pulse signal. When measured by a slow response detector, the gating and probing pulses are convoluted through the integration of Eq.II.3.2.2 at a particular delay time τ_D. At lower orienting intensity (induced phase change « π), the transmission efficiency is approximately proportional to the intensity of the gating pulse. When the gating pulse is more intense, the gating time will be broadened[47,48] (see Fig.II.3.4.2, a2 and b2) and the transmission efficiency is higher. The temporal profile of the transmitted probing pulse signal will experience significant change. For a SOKG, the maximum measured transmission was ~60% when the orienting pulse (1054nm) reached ~0.5 GW/cm^2 in a 1cm CS_2 cell. This is consistent with our previous theory and experiments[36,47,48] of the broadened and oscillating Kerr gate. When the e^{-1} decay time of the gating profile increased, the e^{-1} width of $S(t_D)$ would also increase. Due to the convolution of probing pulse and $T^{s,d}(t)$ in Eq.II.3.2.2, the measured gating times

of DOKG shown in Figs.II.3.4.3b & 3c were only slightly narrower (~10-50%) than the gating time of SOKG. When the gating pulse intensity is ≥ 0.5 GW/cm^2, the e^{-1} decay time of the gated signal is approaching that of the input probing pulse. However, from the calculated transfer function of NDOKG shown in Fig.II.3.4.3c, the true gating time is much smaller than the convoluted transmitted signal shown in Fig.II.3.4.2c, measured and calculated from Eq.II.3.2.2. In principle, the reduced gating times of Fig.II.3.4.3C can be measured using a shorter probing pulse or a transient detection system. The temporal width of the transient probing signal (directly proportional to T(t)) is much narrower than the integrated transmitted signal. The true gating width from a NDOKG is 3 times smaller than that of the input orienting pulse. This is a breakthrough for the ultrafast shutter technology.

A calculated curve of the transient gating time for the transfer function $T^d(t)$ of a NDOKG is plotted in Fig.II.3.4.4 as a function of integrated gating time of $S(\tau_D)$ decay profile at a selected gating pulse intensity of 1GW/cm^2. When the gating time difference δt between these two cascaded Kerr gates is increased, the overlapping time of the transient gating transfer function $T^d(t)$ with oscillating profiles is reduced. In this manner, both the integrated and the transient gating time are reduced. The limitation on the integrated gate decay time is the probe pulse decay time(5-ps), and for the transient decay time, it is 0.

Another factor that affects the shortening of two overlapped oscillating Kerr gates is the relaxation time (damping)) of the Kerr medium. In my experiment and theoretical fittings the gating pulse width. τ_g = 5 ps, and the reorientational relaxation time of CS_2,

τ_0 = 1.8ps, were used. Because of the fast Gaussian pulse decay, as long as the damping factor $\tau_0 < \tau_g$, there is no significant difference between the oscillatory overlapping time

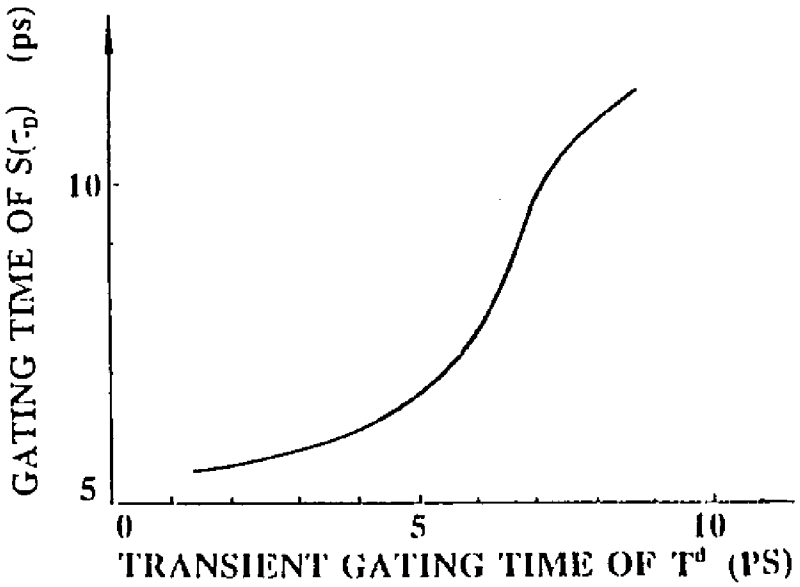

Fig.II.3.4.4. Calculated transient gating time [exp(-1) time $T^t(t)$ as a function of the integrated Kerr gating time [exp(-1) time $S(\tau_D)$ of a NDOKG. In the calculation gating pulse τ_g = 5 ps, probing pulse τ_t = 5 ps, and the gating intensity for both gates is 1 GW/cm^2. The variation of the exp(-1) time T^t (t) displayed on the horizontal axis depends on the overlap time between the two cascaded gates.

and that of an damped gate. When $\tau_0 > \tau_g$, such a nitrobenzene Kerr gate with τ_{00} ~ 32ps, the oscillating period is slower and the gating time is wider. The advantage of DOKG will be reduced in the long damping case.

II.3.5 SUMMARY

For an OKG system, several factors can introduce the system noise and reduce S/N: a) the leakage from the crossed polarizers; b) multi-photon effects such as the transient gating in the Kerr active medium; c) stray light scattered and reflected from optical components; d) optical and electronic noise from the detector. In my measurements, the leakage through the crossed polarizers was the major noise source for both SOKG and

DOKG systems. The maximum system S/N for a SOKG system was ~$1.5x10^3$, which was limited by the extinction ratio $2.5x10^3$ of crossed polarizers. For an DOKG system, the S/N was ~$5x10^5$, which was limited by the extinction ratio of a series set of two pair crossed polarizers (~$7x10^5$).

The theoretical analysis and experimental results of a double-stage optical Kerr gate system have shown a significant improvement of the S/N and the gating time than that of a single-stage Kerr system. The dynamic range of a DOKG has been improved by ~500 times with the transmission efficiency ~10%. A transient gate-opening time of ~3ps was obtained from the experimental deconvoluted data and ~1.9ps from the calculations. The NDOKG can considerably improve the gate-opening time by ~5 times narrower than the orientation pulse. For a m-stage optical Kerr gate system, the overall dynamic range may increase a factor by $(500)^m$ and the gate-opening time can be reduced further. However, due to the increase of the stray light noise caused by the scattered or reflected light and other system noise, further increasing of the number of the Kerr stage number may not bring the same amount of the dynamic range improvement. A multi-stage ultrafast optical Kerr gate system can be adapted for the time-resolved high dynamic range optical switching and imaging measurements, such as time-resolved scattering and fluorescence imaging for biological or chemical samples and optical tomography. Experimental results and theoretical analysis on a double-stage picosecond Kerr shutter are presented. In comparison to a single-stage Kerr gate, >3 times reduction of the gate-opening and 500 times improvement of better signal-to-noise ratio has been achieved in the double-stage Kerr gate.

References

1. A. Edward Profio and Glenis A Navarro,"Scientific basis of breast diaphanography", Med Phys. 16(1), 60-65 1989

2. D. J. Watmough,"Diaphanography, Mechhanism responsible for the images",Acta Radiological Ocology 21 11-15 (1982)

3. Royal J. Bartrum, Jr. and Harte C. Crow,"Transillumination lightscanning to diagnose breast cancer: a feasibility study", AJR 142, 409-414 (1984)

4. S. Webb, "The Physics of Medical Imaging", (IOP Publishing, New York 1990).

5. Irving M. Ariel and Joseph B. Cleary, "Breast Cancer", published by McGraw-Hill, New York (1987)

6. B. Ohlsson, J. Gundersen, and Dag-Martin Nilsson,"Diaphanography: A method for evaluation of the female breast", World J. Surge.,4 701-708, (1980)

7. G. Eric Geslien, J. Ronald Fisher, C. Delaney,"Transillumination in breast cancer detection: screening, failures and potential", AJR 144, 619-622, 1985

8. John J. Gisvold, Larry R. Brown, Ronald J. Raygor, Nancy Dickerson, Marie K. Ranfranz,"Comparison of mammography and transillumination light scanning in the detction of breast lesions", AJR 147, 191-194 (1986)

9. V. Marshall, David C. Williams, Kenneth D. Smaith,"Diaphanography as a means of detecting breast cancers", Radiology, 150 339-343, (1984)

10. Edward A. Sickles,"Breast cancer detection with transillumination and mammography", AJR 142 341-344, (1984)

11. Christian J. M. Mose, Martin C. van Germert, Jan van Marle, William M. Star,

Jonhannes P. A Marilnissen, and Scott A. Prahl, "Measurements and calculations of the energy fluence rate in a scattering and absorbing phantom at 633-nm", Appl. Opt. 12, 2292-2296 (1989)

12. M. A. Duguay and J. W. Hanson, Appl. Opt. 10 2162 (1971)

13. M. A. Duguay and J. W. Hanson, Appl. Phys. Lett., 15 6 (1969)

14. M. A. Duguay and J. Hansen, "An ultrafast light gate", Appl. Phys. Lett. 15, 192-194 (1969)

15. P. P. Ho and R. R. Alfano, Phys. Rev. A17 2170 (1978)

16. P. P. Ho, Y. Liu, R. R. Alfano, J. Chem. Phys. 74 1605 (1981)

17. L. Wang, P. Ho, C. Liu, G. Zhang, R.R. Alfano, Science, 253, 769 (1991)

18. L. Wang, P. P. Ho, R. R. Alfano, "Time-resolved Fourier spectrum and imaging in highly scattering media", Appl. Opt. 26, 5043-5048(1993)

19. P. P. Ho and R. R. Alfano, "Optical Kerr effect in liquids", **Phys. Rev.** A20, 2170-82 (1979).

20. P. P. Ho and R. R. Alfano, Phys. Rev. A20, 2170 (1979)

21. Y. Kusa, A. Ishmaru, A. P. Bruckner, "Experiments on picosecond pulse propagation in a diffusive medium", J. Opt. Soc. Am. 73, 1812-1815 (1983)

22. J. Goodman, "Introduction to Fourier Optics", McGraw-Hill Book Co., New York (1968)

23. Jack D. Gaskill, "Linear System, Fourier Transform, and Optics", (Published by John Wiley & Sons, Ins, 1979 New York)

24. R. J. Zdrojkowswi and R. L. Longini, "Optical transmission through whole blood",

J.O.S.A. Vo.59, 898-904 (1969)

25. A. Ishimaru,"Limitation on image resolution imposed by a random medium"' Appl. Opt. 17, 348 (1978)

26. R. F. Lutomirski, "Atmospheric degeneration of electrooptical system performance"' Appl. Opt. 17, 3915(1978)

27. N. S. Kopeika, S. Solomon, and Y.Gencay,"Wavelength variation of visible and near in-fared resolution through the atmosphere: dependence on aerosol 2nd meteorological conditions" J. Opt. Soc. Am. 71, 892 (1981)

28. N. S. Kopeika, "Spatial frequency dependence of scattered background light: the atmospheric modulation transfer function resulting from aerosol" J. Opt. Soc. Am. 72, 548 (1982)

29. A. Zardecki, Siegfried A. W. Gerstl, and Janon F. Embury, "Mutiple scattering effects in spatial frequency filtering", Appl. Opt. 22, 4124-4131(1984)

30. Hugo J. van Staveren, Christian J. M. Mose, Jan van Marle, Scott A. Prahl, and Martin J. van Gemert, Appl. Opt. Vol.30 No.31, 4507-4514 (1991)

31. Peters et al, Phys. Med. Biol. Vol.35, No.5 1371-1334 (1990)

32. Key et al, Phys. Med. Biol. Vol.36, No.5 579-599 (1991)

33. Amir H. Gandjbakhche, R. Nossal, Roya Dadmarz, Douglas Schwartzentruber, Robert F. Bonner, "Expected resolution and detectability of adenocacinoma tumors within human breast in time-resolved images", SPIE, 2387-18(1995)

34. F. Liu, K. M. Yoo, and R. R. Alfano, "Transmitted photon intensity through biological tissues within various time windows", Opt. Lett., **10**, 740-742 (1994)

35. K. Sala and M. C. Richardson, Phys. Rev. A12, 1036 (1975)

36. P. P. Ho and R. R. Alfano, Phys. Rev. A20, 2170 (1979)

37. D. Hulin, A. Mysyrowicz, A. Antonetti, A. Migus, W. Masselink, H. Morkoc, and H. Gibbs, N. Peyghambarian, Phys. Rev. B33 4389 (1984)

38. D. McMorrow, W. T. Lotshaw, G. A. Kenney-Wallace, IEEE J. Quantum Electron. 24 433 (1988)

39. T. Morioka and M. Saruwatari, Opt. Eng. 29 200 (1990)

40. Y. Li, G. Eichman, R. R. Alfano, Appl. Opt.25 209, (1986)

41. A. P. Bruckner, Appl. Opt. 17 3177 (1978)

42. L. Wang, P. P. Ho, Y. Liu, R. R. Alfano, SPIE 1431 97 (1991)

43. P. P. Ho, L. Wang, R. R. Alfano, SPIE 1599 (1991)

44. K. M. Yoo, Q. Xing, R. R. Alfano, Opt. Lett. 16, (1991)

45. J. A. Giordmaine, P. M. Rentzepis, S. L. Shapiro and K. W. Wecht, Appl. Phys. Lett., 11 216,(1967)

46. Q. X. Li, T. Jimbo, P. P. Ho, R. R. Alfano, Appl. Opt. 25 1869 (1986)

47. P. P. Ho, P. Y. Lu, R. R. Alfano, Phys. Rev. A21, 1730 (1980)

48. P. P. Ho, Y. Liu, R. R. Alfano, J. Chem. Phys. 74 1605 (1981)

Chapter III

Scattering Attenuation Coefficient in Intralipid Solution

III.1 Introduction

The scattering coefficient, $\mu_s = l_s^{-1}$, is one of the most important parameters to characterize the state of a turbid medium. Intralipid solutions have been widely used[1-4] as a model system in optical imaging research for the development of a breast cancer screening system. The scattering coefficient of Intralipid solution was measured by several groups in visible and infrared[1-3] spectral regions using CW-transillumination method[1-3]. In these experiments to avoid the effect of the noise caused by the diffusive or stray light, spatial filtering methods are employed by a collimator with a small spatial aperture or a single-mode fiber. The ability to separate the collimated photons from diffusive photons traveling collinearly with small-diverged angles in the forward direction can seriously limit the accuracy of using the CW transillumination method. When these forward scattered diffusive photons leak into the detector, the measured transmitted intensity is increased and the accuracy of the measured attenuation coefficient or scattering coefficient can be greatly reduced from its true value. It is our opinion that underestimated values of the scattering coefficient μ_s have been measured using the conventional CW approach.

When an ultrashort laser pulse propagates through a turbid medium, the optical paths of the scattered light consist of [4-7]: ballistic, snake, and diffusive components as shown

in Fig.III.1. One major difference between the forward scattered diffusive photons to

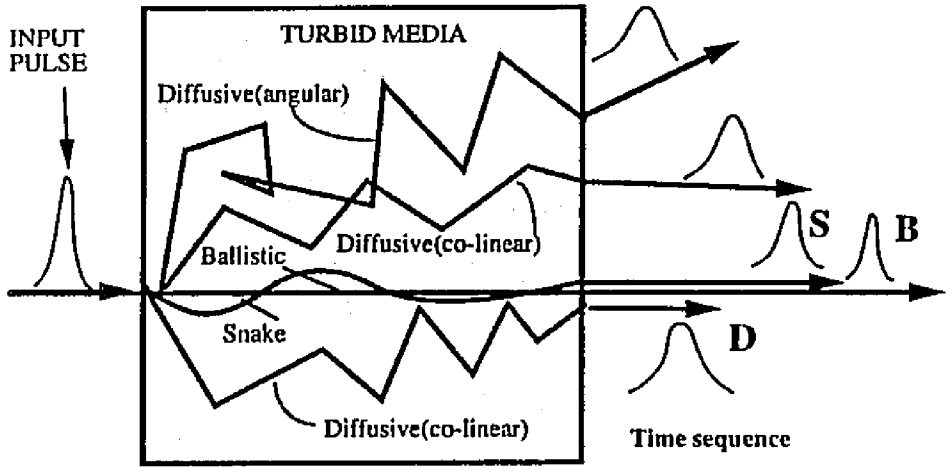

Fig.III.1 A schematic of the forward scattered ballistic, snake, and diffusive photons propagating through a turbid medium. B: ballistic; S: snake; D: diffusive.

the ballistic or snake photons is the arrival time. Diffusive photons emerge at small and large angles. Both of these diffusive photons arrived the detector at the later time due to the multi-scattering in the turbid medium. Time-resolving techniques[4-17], such as a time and a spatial gating[8,9], can provide a noise rejection of diffusive photons with a signal to noise ratio up to 10^{10} to determine the "true" scattering coefficient of a turbid medium with the improved accuracy. The attenuation coefficient of the turbid matter is deduced from the transmitted light intensity of the ballistic component (Eq.III.1.1) which varies as ~ $\exp(-\mu_t z)$.

In this chapter, the true scattering and attenuation coefficients of turbid media using various diluted Intralipid scattering solutions are measured for the first time using the

Kerr-Fourier (KF) imaging method. The differences of the measured scattering coefficients obtained from the time-resolved approach and the traditional CW collimation method[1-3] are compared and described.

Intralipid-10% suspension contains 50-gm soya bean oil, 6-gm phospholipid, 11.25-gm glycerol. The Intralipid solution actually used in this section was diluted with distilled-water to the desired concentration. Using a picosecond time-resolved imaging 'true' scattering (l_s^{-1}) and attenuation coefficients of turbid matter have been determined more accurately. The scattering coefficient measured by the conventional CW collimation method was found to yield smaller attenuation coefficient values in comparison to the attenuation coefficient obtained from the ballistic light component using the early time-sliced photons. Here, I discuss how to measure the "l_s" = μ_s^{-1} by time-resolved ballistic light transmission more accurately.

III.2 Experimental Method

The experimental setup of the time-resolved KF method is shown in Fig.III.2.1. A picosecond gate with the gate-opening time of ~ 10-ps has been used to reject later arrival diffusive photons for an optical path difference of ~ 3.3-mm. The 1054-nm pulse generated from a mode-locked glass laser system was used as the probing beam and its SHG 527-nm pulse was used as the gating beam of the KF system. The CW transillumination detection was performed using the same KF setup of Fig.III.2.1 except the gating pulse was blocked and two crossed polarizers were set parallel to each other.

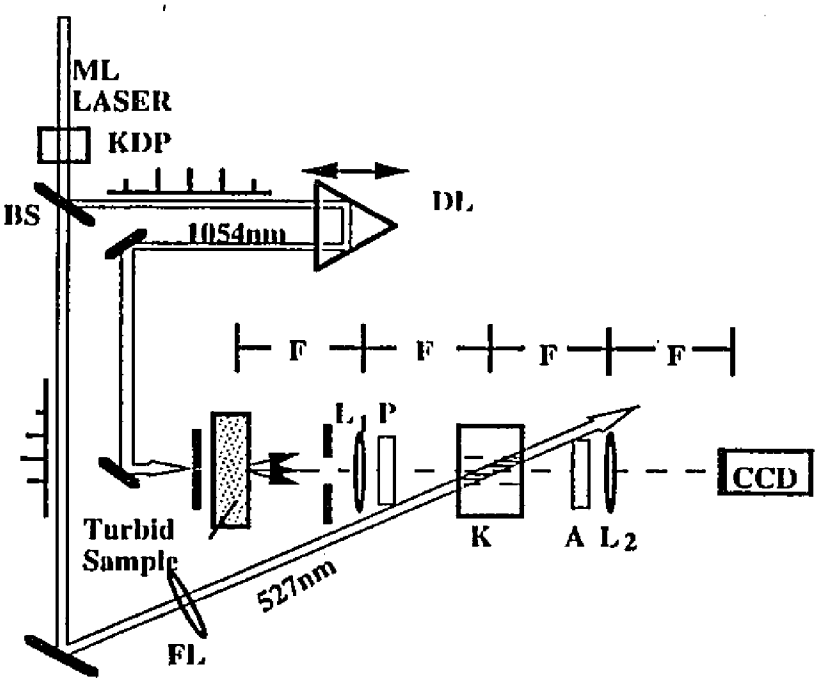

Fig.III.2.1. Time-resolved Picosecond Kerr-Fourier imaging system. The diameter of the gating beam was 2-mm which corresponded to 0.09° = ~1.7-mrad half-angle. For comparison, the same sample has been tested by the CW-F imaging system. The dynamic range of the CCD detector was ~65,000 count. The measured sensitivity at 1054-nm is ~200-photons/count at 1054-nm. The angle between the pumping and probing beams was ~4° and the Kerr transmission efficiency was ~7%. The extinction ratio of a pair of calcite polarizers was ~$1x10^6$. AP: 1-mm input aperture; ML: mode-locked laser-pulse train with the pulse energy fluctuation of ~5% from shot to shot. KDP: potassium dihydrate hosphate crystal for the second-harmonic-generation 527-nm pulse; BS: beam splitter; DL: delay line; P: polarizer oriented at +45° with respect to the polarization of the 1054-nm beam; A: analyzer oriented at -45° with respect to the polarization of 1054-nm beam; K: 1-cm long CS_2 Kerr cell; L_1, L_2: Fourier transform lens with focal length = 60-cm, and 30-cm, respectively. In the CW imaging, the diameter of a mechanical aperture was set to be the same as the beam waist of the gating pulse for the induced aperture in Kerr-Fourier measurement.

Two lenses L_1 and L_2 were set apart by a 2F distance. The sample was placed at the front focal point of L_1 and a cooled CCD camera was set at the back focal point of L_2. The gating 527-nm laser pulse induced a "soft-aperture" in the CS_2 Kerr cell. This induced-aperture worked as a spatial filter to further remove diffusive photons[8,9]. A 10-

mm thick glass cell filled with a diluted Intralipid suspension was used as the sample holder.

III.3 Experimental Results

A typical measured temporal KF intensity profile of the 1054-nm transmitted signal through a 2% diluted Intralipid solution is shown as the solid line in Fig.III.3.1. To calculate the scattering attenuation coefficient, a prompt reference KF signal from a clear water sample is also plotted as the dashed line in Fig.III.3.1. The KF signal through a 1-cm thick 2% Intralipid solution extended to ~70-ps. Neglecting the absorption coefficient (~ 1/500-mm) of the Intralipid solution at 1054-nm wavelength, the attenuation

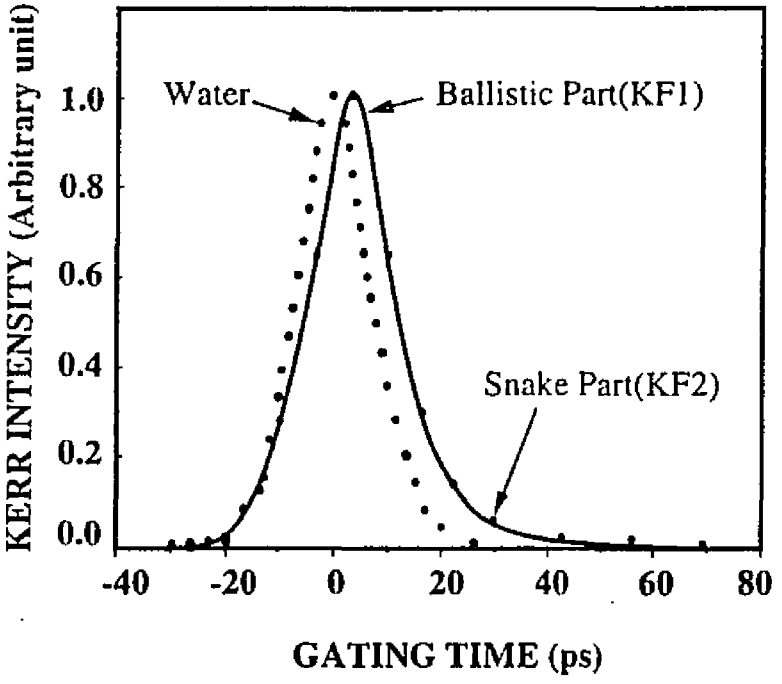

Fig.III.3.1 Temporal intensity profile of the transmitted signal of a 10-ps 1054-nm pulse through a 2% Intralipid solution. Sample cell thickness: 10-mm; probe wavelength: 1054-nm. The dotted line is the Kerr temporal intensity through a 1-cm thick water sample as a reference prompt curve. To compare with the normalized water reference KF signal, the normalized Intralipid KF signal was multiplied by a factor of 74.

of the transmitted signal through a diluted Intralipid solution is mainly attributed to the

scattering process. Using the value of ~2-mm from the KF induced aperture, the ballistic (coherent forward) and snake (early-small-angle forward) scattered photons within the cut-off angle $\alpha = \tan^{-1}(1\text{-mm}/600\text{-mm}) = \sim 0.09°$(air), and ~0.06°(inside the Intralipid solution) can be filtered through the spatial gate. The temporal intensity profile of a laser pulse through a 2% Intralipid solution shown in Fig.III.3.1 consists of ballistic photons arrived at 0±20-ps and early snake photons appearing from 20-70-ps.

The time-resolved ballistic scattering attenuation coefficient, $\mu_{s,KF1}$, of various diluted Intralipid solutions measured by the KF method at T=0-ps is displayed as the square in Fig.III.3.2. The conventional CW scattering attenuation coefficient, $\mu_{s,CWF}$, measured

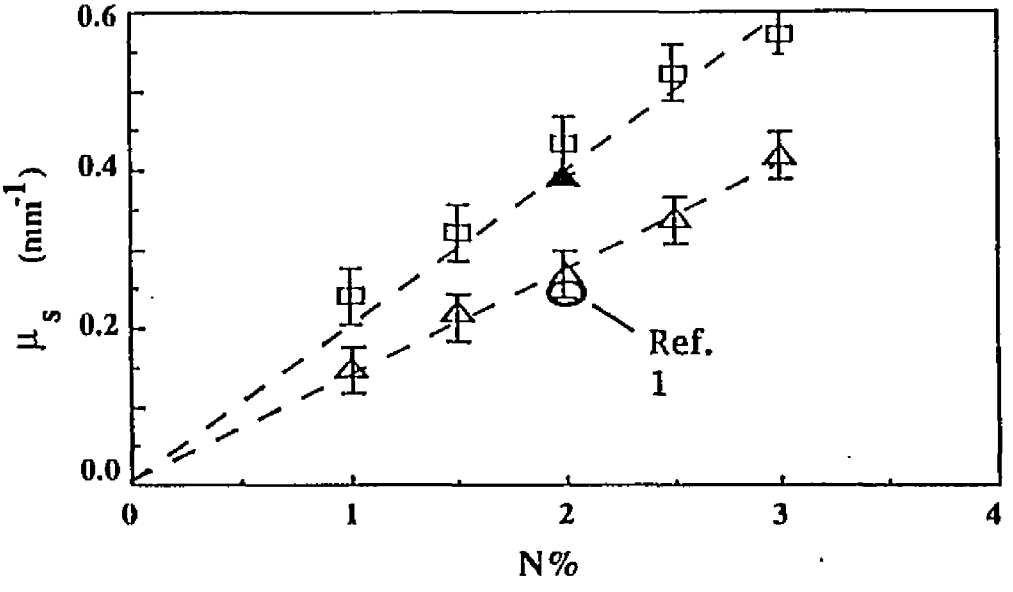

Fig.III.3.2 Scattering Attenuation coefficient μ_s(mm^{-1}) at 1054-nm as a function of the concentration of diluted Intralipid-10% suspension. Sample cell thickness: 10-mm. □: Measured attenuation coefficient of various diluted Intralipid solution from the ballistic KF1. ▲: Measured attenuation coefficient of a 2% diluted Intralipid solution using the time-integrated KF1+KF2. Δ: Scattering attenuation coefficient of various diluted Intralipid solution measured from CWF. o: Scattering coefficient of a 2% Intralipid solution calculated from Ref.1 by CW method.

by the CWF method is displayed as the triangle in Fig.III.3.2. The KF attenuation coefficients displayed in Fig.III.3.2 were determined by the Beer's law using the

transmitted intensity ratio of photons through a 2% diluted Intralipid solution, which arrived at the Kerr gate at T=0-ps (Full Width at Full Maximum of ~40-ps) and that in a clear water. The rest part of the late-arrival snake photons from 20-70-ps shown in Fig.III.3.2 was rejected. The CWF data in Fig.III.3.2 which includes all ballistic, snake diffusive photons coming within 0.09° forward angle was also determined by comparing the intensity ratio with the reference water CW signal. Furthermore, a black triangle shown in Fig.III.3.2 was our deduced ballistic (denoted KF1) and snake (denoted KF2) attenuation coefficient, $\mu_{s,KF1+KF2}$, extracted from a 2% Intralipid solution calculated from the integration of the total Kerr temporal intensity profile of KF1 and KF2 shown in Fig.III.2.1. A circle data point was the scattering coefficient μ_s measured from the conventional CW collimation method as per ref.1.

The scattering attenuation coefficient for KF1 and KF2, $\mu_{s,KF1+KF2}$ obtained from the time-integration of both the ballistic and snake components is different from the $\mu_{s,KF1}$ measured for the ballistic measurement alone. For a 2% Intralipid solution, the integrated intensity ratio from the entire signal profile of KF1+KF2 to the ballistic component of KF1 was 1.26. The transmitted energy measured from the KF1 was 26% less than that KF1+KF2 with the time integration from 0 to 80-ps. This 26% difference in transmitted intensity introduces a 5.3% difference of the scattering attenuation coefficient, i.e.: $\exp[\mu_{s,KF1+KF2}Z]/\exp[-\mu_{s,KF1}Z) = 1.26$. Where the thickness is Z = 10mm. For a 2% diluted Intralipid solution, using the deduced value of $\mu_{s,KF1} = 0.43mm^{-1}$, giving the $\mu_{s,KF1+KF2} = 0.43\ mm^{-1} - \ln(1.26)/10mm = 0.43mm^{-1} - 0.123 = \sim 0.407\ mm^{-1}$.

For the CWF measurements, the deduced scattering attenuation coefficient of a 2%

diluted Intralipid solution is much less: $\mu_{s,CWF}$ ~ 0.28 mm^{-1} as shown by the triangle in Fig.III.3.2. This $\mu_{s,CWF}$ value is close to the scattering coefficient of 0.26 mm^{-1} shown as the circle in Fig.III.3.2 measured by the conventional collimation approach. The relative difference between the ballistic attenuation coefficient to the CW scattering coefficient: $[\mu_{s,KF1} - \mu_{s,CWF}]/\mu_{s,KF}$, is 0.15 mm^{-1}/0.43 mm^{-1} ~ 0.35. This 35% error difference between $\mu_{s,KF1}$ to $\mu_{s,CWF}$ and the 5.3% increment difference between $\mu_{s,KF1}$ to $\mu_{s,KF1+KF2}$ are attributed to the actual size of the Kerr-induced aperture which is less than the 2-mm diameter of a mechanical aperture used in the CWF measurement. Furthermore, using time-resolved diffuse profile measurements, the transport reduced scattering coefficient, μ_{tr} or $\mu_s' = (1-g)\mu_s$ can be determined. The time-resolved $\mu_s'$was found to be larger[16] than the steady-state μ_s'. The results obtained here can be an explanation for these underestimated values.

The measured $\mu_{s,KF1}$ and $\mu_{s,CWF}$ shown in Fig.III.3.2 can be fitted by a linear function on the concentration of Intralipid solution as: $\mu_{s,KF1}$ = 0.19 N mm^{-1} and $\mu_{s,CWF}$ = 0.14 N mm^{-1}, where N is the concentration of the diluted Intralipid solution varying from 0 to 3%. The 0.14 slope from CWF measurement was in good agreement with the slope of 0.13 obtained by other group[1] using conventional collimation approach. The Table III.3.1 shows relevant number results for 2% diluted Intralipid solution.

Methods	μ_{KF1}	$\mu_{KF1} + \mu_{KF2}$	$\mu_{s,cwF}$	$\mu_{s,cw}$(Ref.1)
μ-results	0.43mm^{-1}	0.407μmm^{-1}	0.28mm^{-1}	0.26mm^{-1}

Table III.3.1 The relevant numbers of scattering coefficient μ_s using different method.

This time gating approach can be used to determine an accurate scattering

coefficient of turbid medium. Differences of the scattering attenuation coefficient, μ_s, deduced from the time-resolved to the CW transillumination measurements are accounted for by the later-arrived snake and diffusive photons within the collection angle of the detector. About 20% - 30% error can be obtained to CW measuring method. Time- and space- gated imaging methods provide a significant reduction of the diffusive photons from the conventional collimation transillumination approach to determine the **true scattering coefficient**, μ_s, of a turbid medium.

Reference

1. Hugo J. van Staveren, Christian J. M. Mose, Jan van Marle, Scott A. Prahl, and Martin J. C. van Gemert, "Light scattering in Intralipid-10% in the wavelength range of 400-1100nm", Appl. Opt. 4507-4514 (1991).
2. Christian J. M. Mose, Martin C. van Germert, Jan van Marle, William M. Star, Jonhannes P. A Marilnissen, and Scott A. Prahl, "Measurements and calculations of the energy fluence rate in a scattering and absorbing phantom at 633-nm", Appl. Opt. 12, 2292-2296 (1989)
3. I. Driver, J. W. Feather, P. R. King, and J. B. Dawson, "The optical properties of aqueous suspensions of Intralipid, a fat emulsion", Phys. Med. Biol. 12, 1927-1930 (1989)
4. R.R. Alfano, X. Liang, L. Wang, P. Ho, "The time-resolved imaging of translucent droplets in highly scattering turbid media", Science, 264, 1913-1915 (1994).
5. L. Wang, P. Ho, C. Liu, G. Zhang, R.R. Alfano, "Ballistic 2-D imaging through

scattering walls using an ultrafast Kerr gate", Science, 253, 769-771 (1991)

6. K. M. Yoo and R. R. Alfano, "Time-resolved coherent and incoherent components of forward light scattering in random media", Opt. Lett. 15, 320-322 (1990)
7. B. Das, K. Yoo, R. R. Alfano,"Ultrafast time gated imaging", Opt. Lett., 18, 1092 -1094 (1991)
8. L. Wang, X. Liang, P. P. Ho. R. R. Alfano, "Fourier-Kerr imaging in thick turbid media", Opt. Lett. 18, 241-243 (1993)
9. L. Wang, P. P. Ho. R. R. Alfano, " Time-resolved Fourier spectrum and imaging in highly scattering media", Appl. Opt. 26, 5043-5048 (1993)
10. D. Benaron, D. Stevenson, "Optical time of flight absorbance imaging of biomedical media", Science, 259, 1463-1466 (1993)
11. L. Izatt, M. Hee, D. Huang, E. Swanson, C. Lin, J. Schuman, C. Puliafito, Fujimoto, "Micro resolution biomedical imaging", Opt. & Phot. News, 4, No.10, 14-19 (1993)
12. H. Chen, Y. Chen, D. Dillworth, E. Leith, J. Lopez, J. Valdmanis, "Two dimensional imaging through diffusive media using 150 fs gated holographic technique", Opt. Lett., 16, 487-9 (1991)
13. M. Duncan, R. Mahon, L. Tankersley, J. Reintjes, "Spectral & temporal characteristic of spontaneous Raman scattering in the transient regime", Opt.Lett., 16, 1868-1870 (1991)
14. M. S. Patterson, B. Chance, B. C. Wilson,"Time-resolved reflectance and transmittance for the noninvasive measurement of optical properties", Appl. Opt. 28,

2331-2336 (1989)

15. M. A. Duguay and A. T. Mattick,"Ultrahigh speed photography of picosecond laser pulses", Appl. Opt. 10, 2162-2170 (1971).

16. S. J. Madsen, B. C. Wilson, M. S. Patterson, Y. D. Park, S. L. Jacques, Y. Hefetz, "Experimental test of a simple diffusion model for the estimation of scattering and absorption coefficients of turbid media from time resolved diffusive reflectance measurements", Appl. Opt. 31 3509-17 (1992)

17. Hanli Liu, Andreas. H. Hielscher, C. Dean Kurth, S. L. Jacques, and Britton Chance, "Time-resolved photon migration in a heterogeneous tissue-vessel model", **SPIE**, 2389, (1995).

Chapter IV

Spatial Resolution Determination Through Turbid Media By Time-resolved Imaging of A Point Light Source

IV.1 Introduction to Spatial Resolution

High spatial resolution is a major issue for an optical transillumination imaging to determine the size of object in highly scattering media, such as biomedical samples. When the collimated photons travel through the turbid media, besides the diffusive scattering, the spatial variation of the optical properties of the media (such as refractive index n, absorption parameter, and scattering parameters) will modulate the intensity, speed, and traveling direction of the input photons. The spatial variations of these parameters will be greatly effected by the multi-scattering, especially fine spatial changes, which represented the details of image, that is, the higher resolution part of image signal. Degrading of resolution will limit the sensitivity of a transillumination imaging technique. This effect has been happening in the transillumination imaging of breast, where a tumor with diameter < 1cm often goes undetected unless they lie near the surface. The degrading of resolution has been studied using non-time-resolved imaging methods[1-9]. In those experiments, the intensity spatial profile of image of a point object has been measured and analyzed. These results have shown that the degrading was due to the loss of the higher spatial frequency components. The theoretical analysis and numerical

simulation of spatial resolution have shown that spatial resolution of diffusive photons is limited to ~0.2Z in diffusion limit[9], where Z is size of the thickness of turbid media. For 50mm thick tissue, the spatial resolution is about ~1cm

To investigate the change of spatial resolution in turbid media, a point spread function (PSF) transmission need to be determined. The image signal of an ideal point source (object) is a spatial intensity distribution of δ-function. Based on Fourier transform. Fourier spatial spectrum profile of a δ-function is a infinite horizontal line with an unit height all over the whole spatial frequency coordinate, as shown in Fig.IV.1.1. After transmitting through an imaging system, any distortion of this flat spectrum profile will reflects the effect caused by the imaging optics, detector, object to be imaged, and the media surrounding the object. Usually, the higher frequencies are easily attenuated in a actual imaging system, which results the spread of the image of the δ-function, as shown in Fig.IV.1.2. Therefore, the intensity profile of a point source is easy to use to determine the transmission of the spatial resolution.

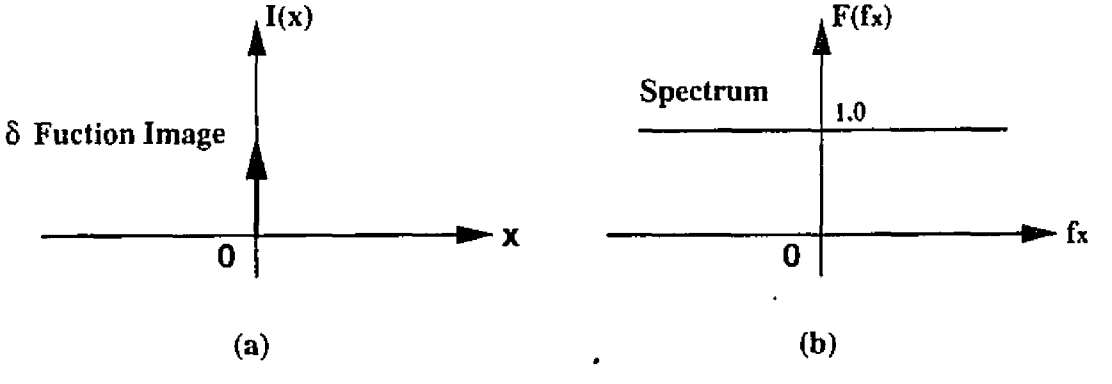

Fig.IV.1.1 δ-function (a) and its Fourier spectrum (b).

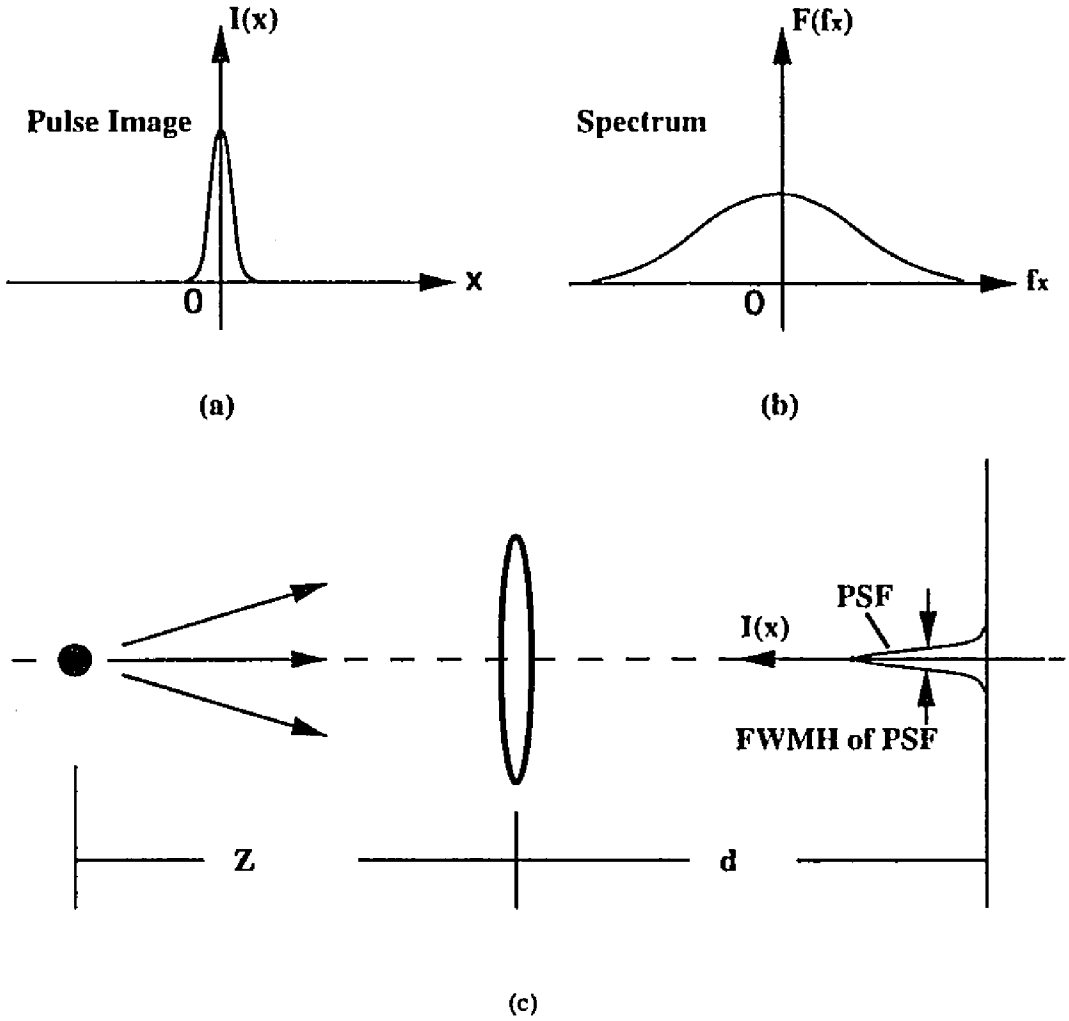

Fig.IV.1.2 Actual PSF (a), its Fourier spectrum (b), and an experiemntal setup to determine PSF. Z is the distance of a point source; d is the imaging distance, and f is focus length of imaging lens.

The image of a point source can be regarded as a simplest object or an element of an object, and the width of intensity profile of a point source represents a spatial resolution response of an imaging process. The image of a point source is generally characterized by 2D intensity distribution, which is called Point Spread Function, PSF(x,y), where x-y plane is perpendicular to the photon propagating direction. PSF(x,y) describes the spread out of a point image transmitted through an imaging system. For a

symmetrical distribution in x-y plane, a 1D intensity profile may be used, PSF(x) or PSF(y).

The image of an object is related to a point spread function, PSF, by a convolution of PSF and the intensity distribution of the object:

$$I_i(x,y) = \int\int PSF_o(x,y)I_o(x'-x, y'-y)dx'dy' = PSF_o * I_o, \quad \text{(IV.1.1)}$$

where, I_i and I_o are intensity distributions of the image and object, respectively, and $PSF_o(x,y)$ is the Point Spread Function, representing the spatial response of an optical imaging system without turbid media. The x' and y' are the coordinates in the object plane, and x and y are in image plane. The "*" represents a convolution operation. When a turbid medium exists, the overall spatial response, PSF, is modulated by optical properties of turbid medium, which is the determined by the convolution of PSFs of the imaging system, PSF_o, and turbid media, PSF_t :

$$PSF = PSF_o * PSF_t, \quad \text{(IV.1.2)}$$

where, PSF_t is determined by a turbid medium, and PSF is an overall PSF of an imaging system with turbid media. When the PSF_0 is a δ-function (for a perfect imaging system), the overall PSF is related PSF_t by:

$$PSF = PSF_o * PSF_t = \delta * PSF_t = PSF_t, \quad \text{(IV.1.3)}$$

Then, an image I_i is formed by a convolution of an overall PSF and the object intensity distribution:

$$I_i = PSF * I_o = PSF_o * PSF_t * I_o. \qquad (IV.1.4)$$

In an actual imaging system, the PSF_0 is a pulse-like profile with finite FWMH instead a δ-function, as shown in Fig.IV.1.2a. However, the effect of PSF_0 may be neglected when FWMH of PSF_0 is much less than that of PSF_t. In this case, $PSF = PSF_o * PSF_t \approx PSF_i = PSF_t$. For example from our actual data, as shown in Fig.IV.2.1.3, the late-time spatial resolution is about 5 to 6mm for a 0.2% solution of 0.45μm Polystyrene particle at 527nm, which is much more than the FWMH = ~0.08mm of PSF_0 of the imaging system. In this case, the FWMH of 5~6mm can be regarded as the PSF_t, i.e., FWMH of $PSF_t \approx$ 5~6mm.

However, for the early-time detection, the measured FWHM of PSF is about 0.5mm, which must be regarded as the effect of both PSF_0 and PSF_t in the measuring determination of spatial resolution shown in next section.

The intensity profile of a point source, which is made of focusing the laser beam onto a scattering glass, will be used as a PSF. Due to the diffraction of the lens, the diameter of focusing point is limited about 0.2mm (instead of δ-function). To take the effect of this finite diameter into account, measured PSF shown in Eq.IV.1.3 has to be modified as:

$$PSF = PSF_p * PSF_o * PSF_t \qquad (IV.1.5)$$

where PSF_p is the intensity profile of the focusing point source, which is approximately a Gaussian function with FWMH of ~0.2mm in my research work.

The PSF_t can be obtained by deconvolution of the Eq.IV.1.5 if measured PSF, PSF_p, and PSF_0 are known. However, in the spatial resolution determination (as discussed in next section), the FWMH instead of the profile of PSF_t is the major problem to be answered. In this case, FWMH of PSF_t can be easily estimated according to the convolution property (refer to *Linear System, Fourier Transforms, and Optics*, J. D. Gaskill):

$$\text{FWMH of PSF} \approx \text{FWMH of } PSF_p + \text{FWMH of } PSF_0 + \text{FWMH of } PSF_t \quad \text{(IV.1.6)}$$

The Eq.IV.1.5 is valid only if PSFs profile is limited in a finite duration.

When a highly scattering media exists between input illumination light and output signal, the shape and amplitude of overall PSF would be strongly affected by the scattering media. The actual images of a point source through the 50mm-thick 0.088% Polystyrene particle solution at 527nm detected by a conventional optical Kerr gate imaging system are shown in Fig.IV.1.3[11]. The PSF images were obtained at T=0, (a); T=10ps, (b); T=20ps, (c); and T=40ps, (d). The digitized profiles on the top-right is the measured PSF for each different gating time. The PSF is spreading out (FWHM of a point image increased) caused by scattering of the particle solution with the delay of the imaging time, as shown in Fig.IV.1.4. For different scattering media, the broadening of PSF will be different as shown in the following section of this chapter. Therefore, the

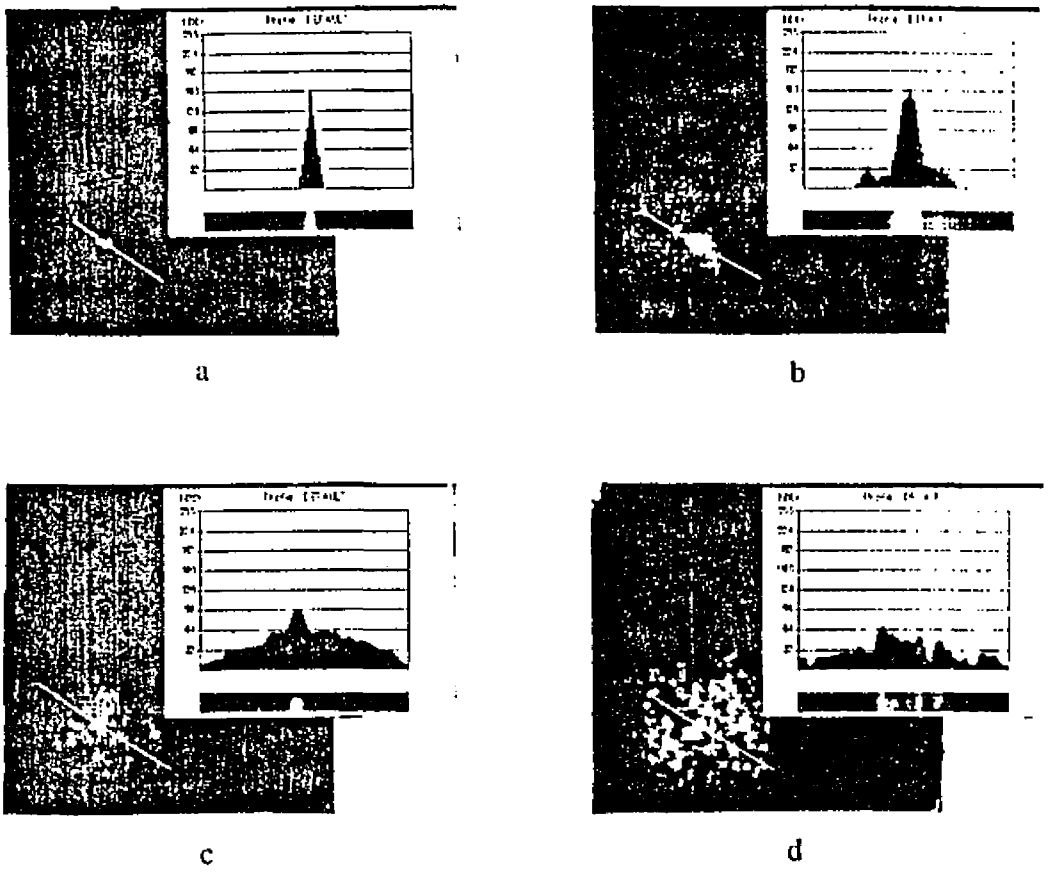

Fig.IV.1.3 Time-resolved images of a single point source behind a 0.45μm Polystyrene particle solution with volume density 0.088%. Turbid medium cell thickness: 50mm; wavelength: 527nm. (a) T=0, PSF ~0.2mm; (b) T=6.6ps, PSF ~0.35mm; (c)T=19ps, PSF ~0.9mm; (d)T=40ps, PSF ~1.6mm.

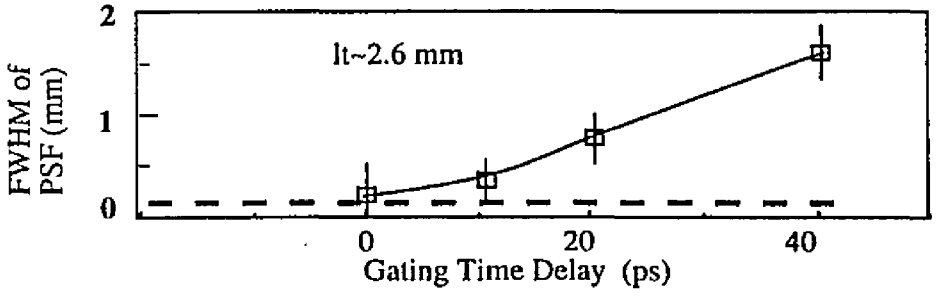

Fig.IV.1.4 Spatial resolution (FWHM of a Point Spread Function) as a fuction of the gating delay time in ps. Squares data: in 0.46μm Polystyrene particle solution with 0.088% concentration (g~0.9); Dashed line: in clear water. Wavlength : 527 nm; Glass cell size:5x5x5cm

measurement of FWMH of the PSF can be used to investigate the degrading of spatial

resolved distance of image, i.e., the spatial resolution, which is explained in Fig.IV.1.5. When there is no turbid media exist (refer to the top part of Fig.IV.1.3), PSF appears sharp peak with narrow width (where PSF is not a δ-function to simulate an actual imaging condition due to the limitation by the resolving capability for an imaging system). When turbid media exists (refer to the bottom part of Fig.IV.1.3), the point

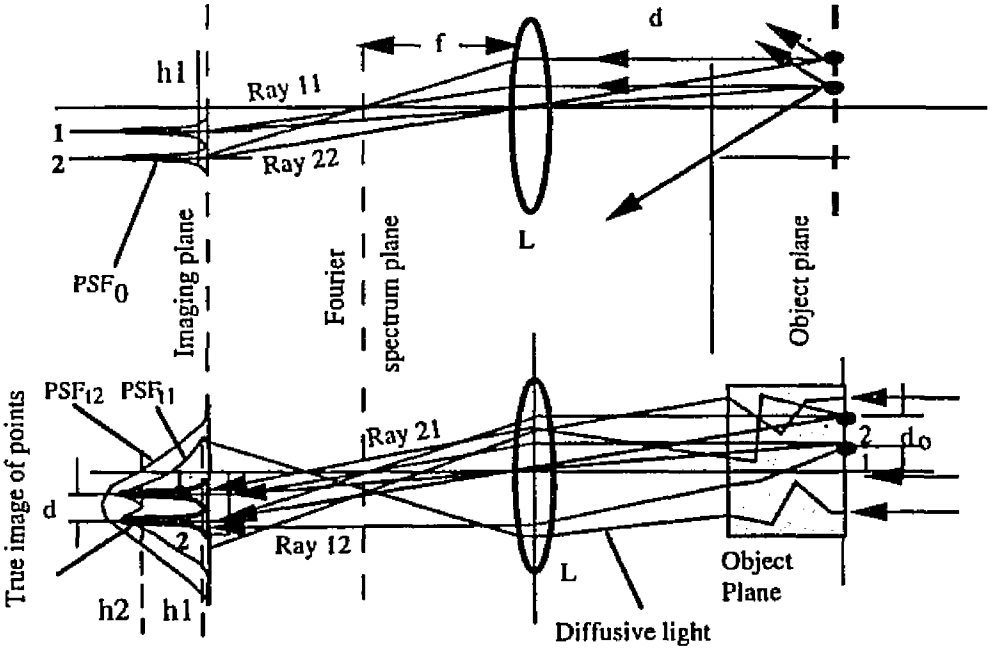

Fig.IV.1.5. Imaging of a double-point source with / without turbid media existing. R11: path of photons from point 1 of object onto point 1 of image; R22: path of photons from point 2 of object onto point 2 of image; R12: path of photons scattered from point 2 of object onto point 1 of image; R21: path of photons scattered from point 1 of object onto point 2 of image. L: imaging lens; d: separation distance between two points in image plane; PSF_0: point spread profile without turbid media existing; PSF_{t2}, PSF_{t1} : point spread profiles with turbid media existing; h1, h2: gap-depths in between two points in image plane.

images were broadened since some photons diverged from their original paths due to multi-scattering in turbid media. The broadness of PSF would result in: (1) the decrease of image contrast, resolution and SNR.

The resolution decrease caused by PSF broadness can be explained by the bottom part of Fig.IV.1.3: the increase of the width of PSF, as shown by PSF_{t1}, caused the more overlap of the profiles in between two points, which result in the reduction of gap depth, which was equivalent to the contrast decrease. When the width of PSF increased up to make gap vanished, as shown by PSF_{t2}, these two points were not resolved. To resolve these two points, the separation in between these two points has to be increased that is, the resolution decreased.

The SNR decrease was caused by the crosswalk of signals among different image areas and spoiled at the imaged point. Through the crosstalk, diffusive photons irregularly arrived at anywhere of a detected image, distorted true intensity distribution, and increased the level of noise background

Recent imaging research[10-15] has determined that the image information is carried by the ballistic or snake-like photons within Δ t window. The image will not or slightly be distorted in the propagation in turbid media. Meanwhile, the part of image information carried by diffusive photons will be lost due to the total distortion of traveling direction and intensity of the photon. The image with highest resolution and contrast will be formed only by early-arrival ballistic and snake photons. However, the ballistic photons in visible and IR wavelength through thick biomedical tissues is actually undetectable due

to the extremely high attenuation. Consequently, the early-arrival "small-angle" photons in Δ t, i.e., the snake photons have to be the main component to be detected to improve the image spatial resolution. To determine the temporal distribution of resolution degrading in turbid media, an ultrafast time-resolved optical imaging system has to be used within Δ t. In the next section, the temporal distribution of resolution will be presented, where, a single-point and a double-point sources have been measured using a picosecond time-resolved imaging system shown in the next section.

IV.2 Temporal Distribution of Resolution of Snake and Diffusive Photons Through Turbid Media

The spatial resolution through highly scattering media is possibly improved using early-time detection. Due to the difference of the arrival time of the ballistic/snake and the diffusive photons, the PSF and SNR will be a function of the detection time. At the early-time detection, the late-arrival diffusive photons were filtered out, and the higher resolution would be achieved. The spread out of a point image would be none or slight, (i.e., the more narrow PSF) and lower noise background (i.e., the higher SNR). At the later time, the more diffusive photons appeared in the signal of detected image, which result in lower resolution (a more-diverged PSF) and poor SNR. The demonstration of these concept is shown in the following experiments by imaging the a point-source and a double-point source through turbid media by a time-resolved imaging system.

IV.2.1 Propagation of a Single-point Image Signal Through Turbid Media

In this experiment, a conventional picosecond optical Kerr gate imaging system was used as the experimental setup and a 4F imaging system have been used in this experiment as shown in Fig.IV.2.1.1a and 1b.

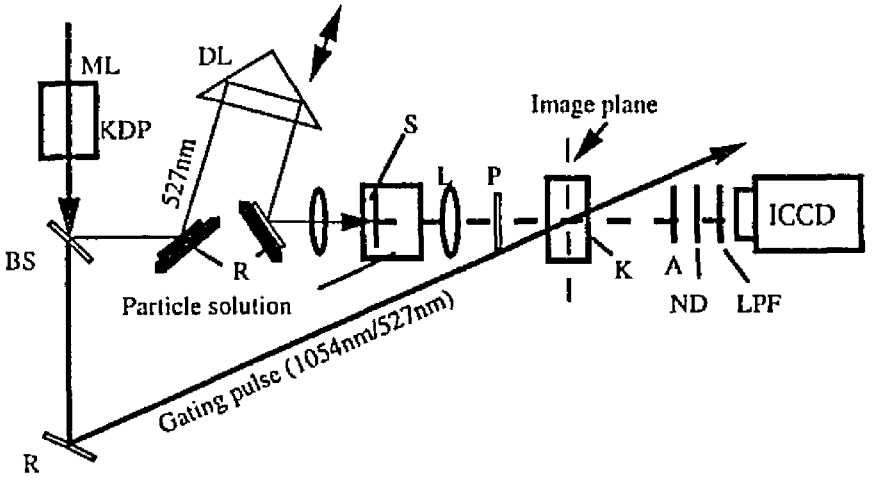

Fig.IV.2.1.1a A conventional Kerr gate imaging system used to determine the resolution distribution at 527nm as a function of gating time. ML, mode-locked laser-pulse train; the laser-energy fluctuation was ~5% from shot to shot. KDP, potassium dihydrate phosphate crystal for a second-harmonic-generation pulse; BS, beam splitter; DL, delay line; The extinction ratio of the pair of calcite polarizers was ~10^6: P, polarizer oriented at +45 with respect to the polarization of the 527-nm beam; A, analyzer oriented at -45 with respect to the polarization of 527-nm beam; K, 1-cm-long CS_2 Kerr cells; L, lens; ND, neutral-density filters; NB: 527nm narrow-band filter; CCD: -45°-cooled CCD camera with a sensitivity of ~1count/20photons at 527nm. The changes of the detection time was done by adjusting a optical delay-line in pumping beam path.

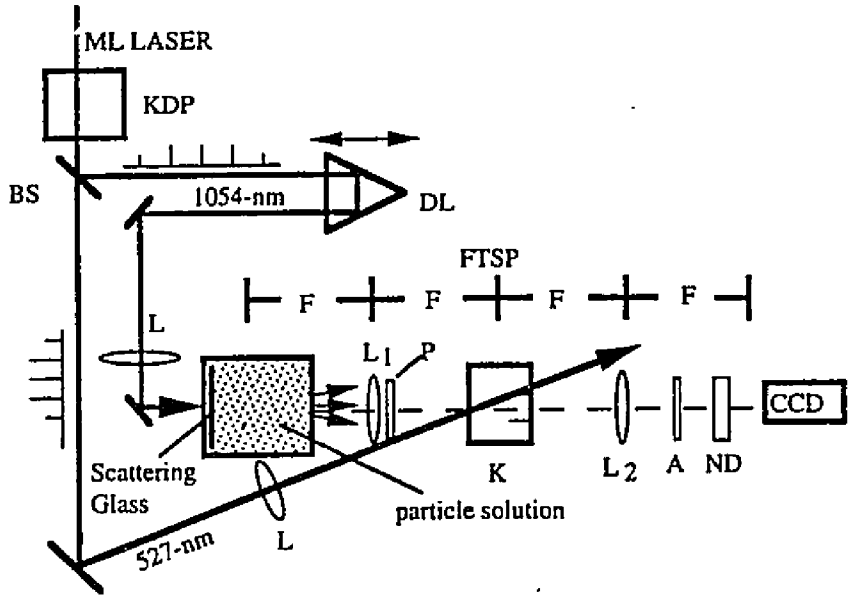

Fig.IV.2.1.1b Experimental setup of the optical Kerr-Fourier imaging system to determine the resolution distribution at 1054nm as a function of gating time.

To avoid the anisotropic scattering pattern, the 10-ps 527nm/1054nm laser pulses was focused on a piece of scattering glass to simulate a single-point source. The spot size was ~0.3mm. The scattering glass was placed illumination side inside 50x50x50 mm^3 glass cell, which was filled with 0.45μm Polystyrene particle solution at the 0.1% and 0.2% of 10%-stock.

The transport cross section coefficient of a single particle can be calculated by

$$l_t = (N\sigma_t)^{-1} = 4\pi a^3/(3f\cdot\sigma_t) = 2.125/f, \qquad \text{(IV.2.1)}$$

where f is volume concentration, $\sigma = 2.26 \times 10^{-2}$ μm^2, a is the radius of the particle ball. The concentration = 0.1%, 0.2% of stock 10% solution for 527nm test, and 0.4% of stock 10% solution for 1054nm test. The calculated l_t for three different concentrations are: 21.2mm, 10.6mm for 0.1% and 0.2% at 527nm, and 5.3mm for 0.4% at 1054nm respectively.

The time-resolved FWHM of PSF and the intensity profile of a point source image with three different l_t, l_t = 21.2mm, l_t = 10.6mm, and 5.3mm, are displayed in Fig.IV.2.1.2, Fig.IV.2.1.3, and Fig.IV.2.1.4 respectively. The first two tests were done at 527nm, and last test was done at 1054nm. First two tests were finished using a conventional Kerr imaging setup shown in Fig.IV.2.1.1a. The third test was finished with the 527nm pumping of ~2.5mm diameter (~2.5mm diameter space gate) in 4F imaging system (shown in Fig.IV.2.1.1b), and 1054nm probing laser beam.

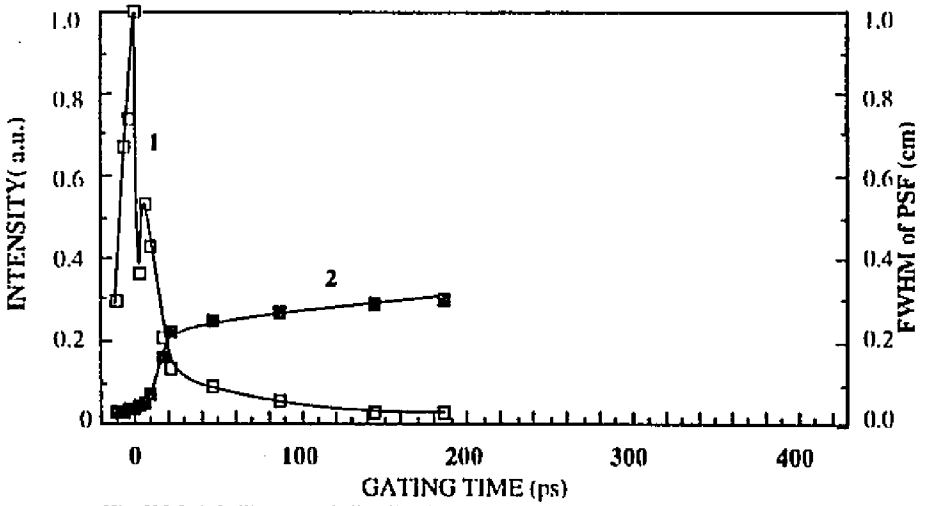

Fig.IV.2.1.2 Temporal distribution of intensity , curve 1,and FWMH , curve 2. of a point source at 527nm as a function of gating time using setup (a). Concentration of 0.45 μm Polystyrene particle: 0.1% of 10% stock. l_t = 21.1mm. g = 0.9.

The data of 0.1% Polystyrene particle solution at 527nm is shown by solid squares

in Fig.IV.2.1.2. Due to the less concentration, the first intensity peak at T=0 consisted of ballistic rapidly decrease of ballistic/snake photons and the increase of diffusive photons. The second intensity peak at ~7ps consisted of diffusive photons and some snake photons. When T > 7ps, the number of snake photons decreased, which caused the resolution rapid reduction. Ballistic photons with the smallest PSF size of ~0.3mm arrived in the range from ~-10ps to +10ps. In the range from ~10ps to ~16ps, the quickly broadening of PSF from ~0.3mm up to ~0.65mm shows the increase of diffusive photons.

The data of 0.2% Polystyrene particle solution at 527nm is shown in Fig.IV.2.1.3: at T=0, the ballistic peak was not shown mainly due to the limitation of detection sensitivity and temporal resolution of the imaging system. Because of the higher

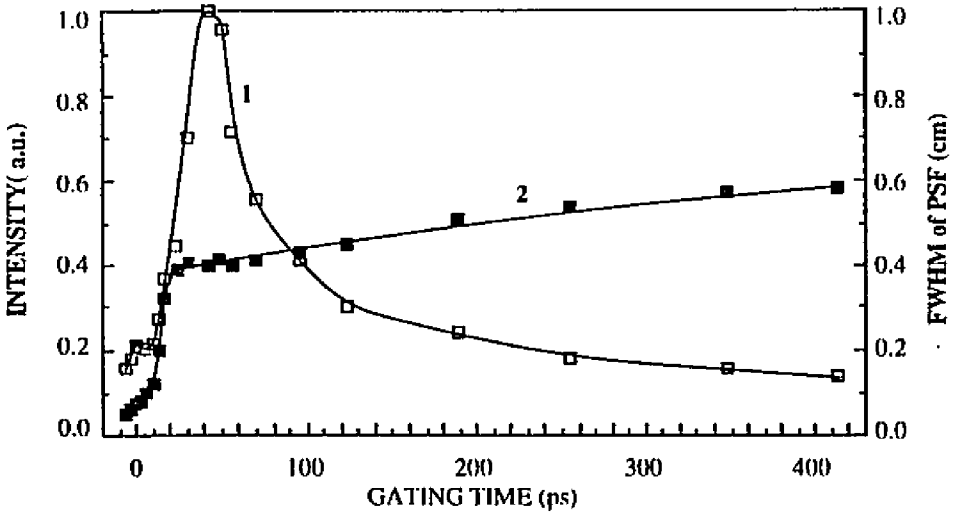

Fig.IV.2.1.3 Temporal distribution of intensity , curve 1, and FWMH, curve 2, of a point source at 527nm as a function of gating time using setup (a). Concentration of 0.45 μm Polystyrene particle: 0.2% of 10% stock. l_t = 10.6mm. g-0.9.

concentration, the FWHM of PSF at early-time range from -5ps to 5ps was ~0.5mm,

which was larger than that in the 0.1%-concentration experiment. At T=20ps, FWHM of 4mm is obtained. In the diffusive range with T > ~50ps, the FWHM of PSF increased to ~6mm comparing to the resolution in diffusion limit was ~10mm. The main reason for the difference is that the optical distance of ~5l_t was still not saturated at a real diffusion limit condition.

CW results of FWHM in both the above tests have been measured, which was ~2.6mm and ~6mm for 0.1% and 0.2% solution experiments. The $FWHM_{0.1\%} \approx 2.6$mm is less than the FWHM of late-arrival diffusive portion because that the CW FWHM included all parts of signal: early-time-high-resolution part, and late-time-low-resolution part, where the first part was the domination to make the overall FWHM less than that of diffusive FWHM. Meanwhile $FWHM_{0.2\%} \approx 6$mm is approximately equal that of the diffusive portion because the late-time-low-resolution diffusive photons dominated overall FWHM due to the denser concentration in this experimental condition.

In the 1054nm experiment, the resolution and intensity profile of a 0.4% diluted particle solution at 1054nm detected is shown in Fig.IV.2.1.4. Where, the horizontal coordinate is 40ps instead 430ps as in Fig.IV.2.1.2 and Fig.IV.2.1.3. Due to the rejection of small induced aperture (~2.5mm diameter) to the diffusive component, the curve distributed in about 40 ps range. The FWHM of measured PSF is less than 1mm throughout the whole range. In this experiment, a CW imaging has been done to compare the result from 4F system. It is found that CW FWHM was about 5.5mm diameter, comparing the K-F FWHM of <1mm upto 40ps shown in Fig.IV.2.1.4. At early-time T=0, the measured FWMH of PSF was ~0.4mm. Considering FWMH of $PSF_0 \approx 0.08$mm

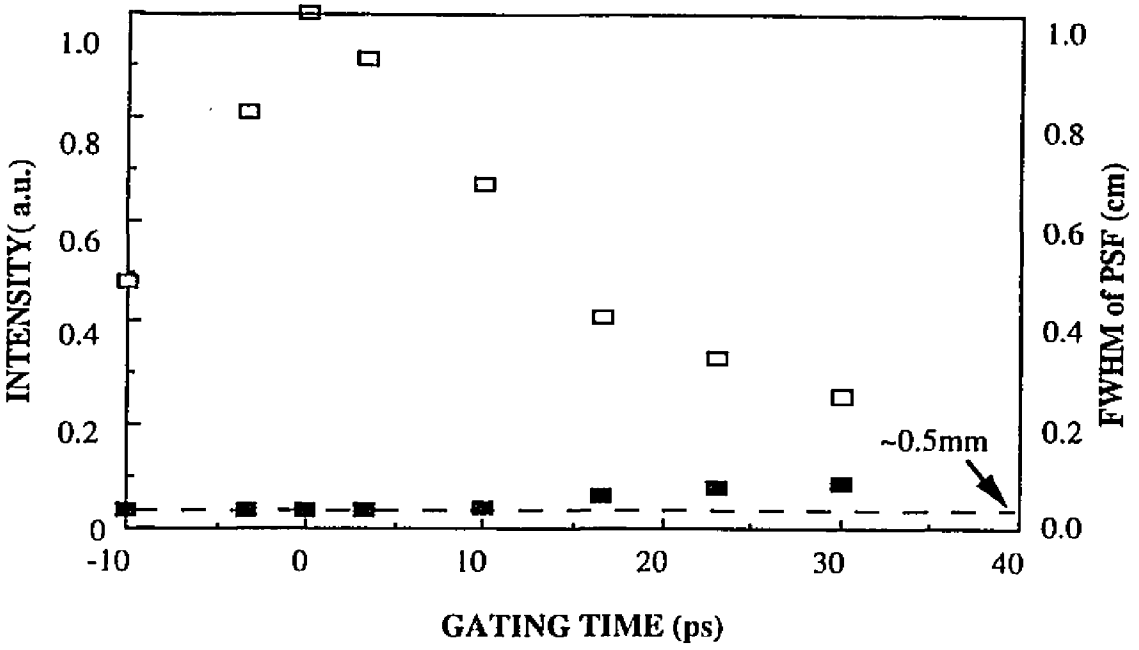

Fig.IV.2.1.4 Temporal distribution of intensity and FWMH of a point source at 1054nm as a function of gating time using setup (b). Concentration of o.45 m Polystyrene particle: 0.4% of 10% stock. l_t = 5.3mm. g=0.6.

(the minimum resolvable distance of the imaging system used in this experiment was calibrated to be ~0.08mm), and FWMH of $PSF_p \approx 0.2$mm, FWMH of PSF_t of 50mm-thick 0.4% Polystyrene particle solution is estimated as ~0.12mm.

IV.2.2. Double-Point Source imaging

To demonstrate the reduction of image contrast and resolution caused by the broadening of PSF, a double-point source imaging experiment has been prepared by time-resolved and a CW imaging systems separately. In this experiment, the determination of the contrast and spatial resolution as a function of the detection time was done by imaging a double-point fluorescence source through a turbid medium. A double-point

source imaging system is shown in Fig.IV.2.2.1. Where, the pair of point simulated two adjacent points on an object surface. The double-point source was made by focusing 527nm laser beam onto a 0.1mm thick PDA film was used as an object detected through a turbid medium cell. The size of point was ~200μm and the separation between them was ~400μm, which approximately represented ~0.4mm resolved distance of the object (double-point source). The NσZ for the turbid medium was ~0.74. A 527nm beam was used as an illumination light source and 1054nm laser beam was used as a pumping pulse.

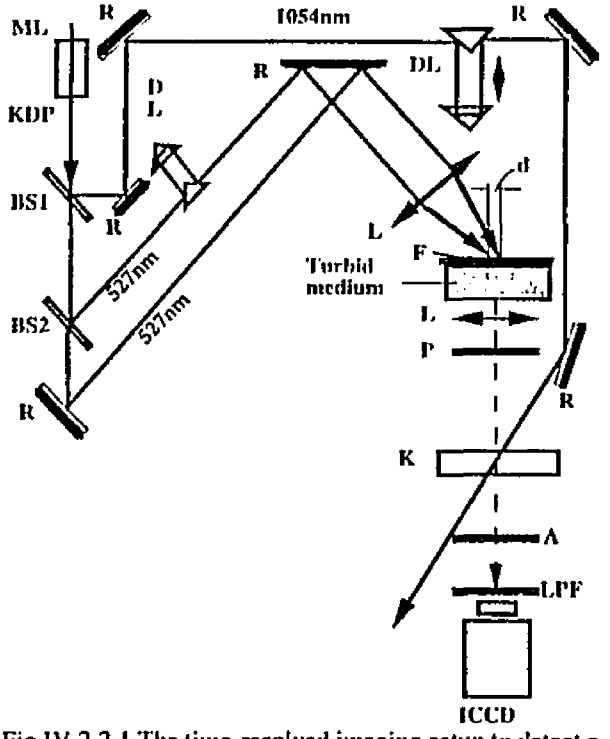

Fig.IV.2.2.1 The time-resolved imaging setup to detect a fluorescence double-point source through Polystyrene particle solution.

The Kerr image at T=0 and CW image[11] are shown in Fig.IV.2.2.2 a and b, respectively.

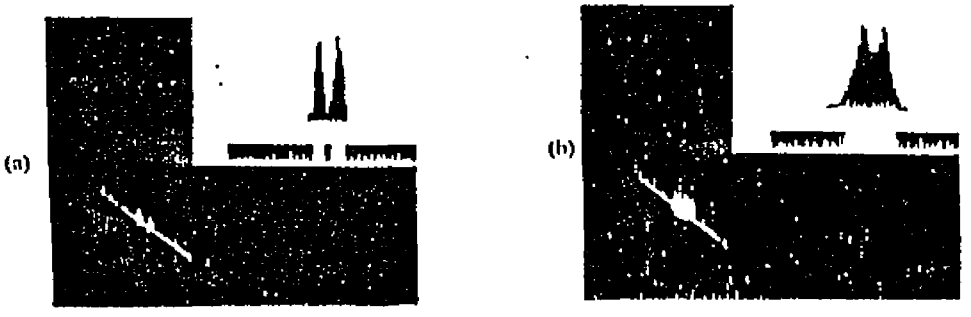

Fig.IV.2.2.2 The time-resolved image of a fluorescence double-point source through Polystyrene particle solution.
a) Time-resolved image detected at T=0; b) CW image

In CW detection, the gap between two points almost disappeared because too wide foots of both point overlapped together. The decrease of the gap depth implied the contrast decreased, which used happen in CW imaging.

The imaging method discussed at above has been used to image an Air Force testing bar chart at different gating times in turbid media. The images detected are shown in Fig.IV.2.2.3.The bar width was 100μm. The bar contrast was 100% tested with the turbid

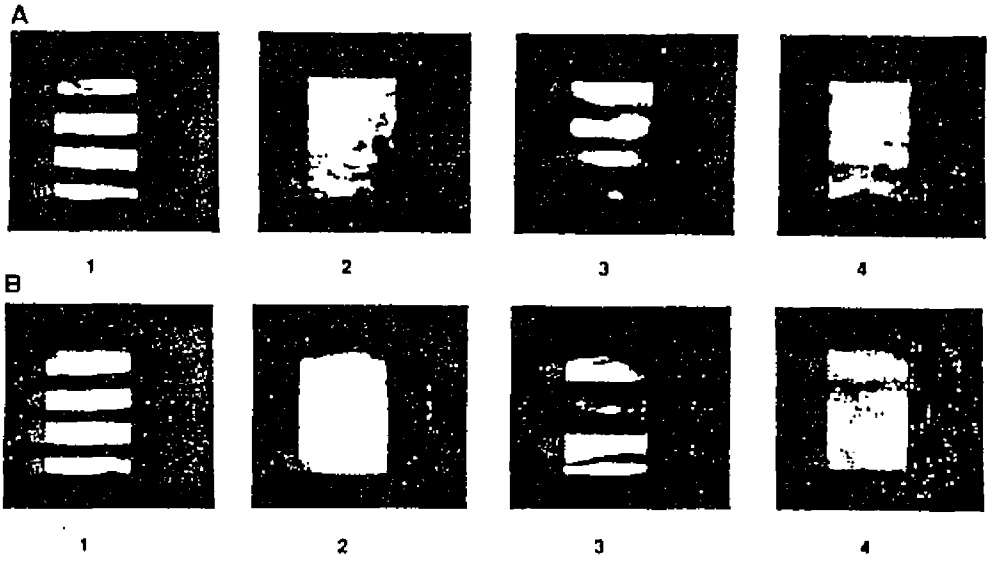

Fig.IV.3.2.2 Two-dimensional images of the test chart behind (A) 3.5-mm thick human breast tissue and (B) 3-mm-thick chicken breast t issue illuminated by 8-ps, 527nm laser pulses. The test object is a five line pairs per millime ter target from an Air Force bar test chart. Dark bars are the object, and the white area is the transparent background, The width of each bar is ~100um. (1) Reference image (tissue removed), (2) No time gate (standard transillumination), (3) t_D=0, time gate at zero dely time, (4) t_D =22ps, time gate at 22-ps delay time. A 200um spatial resolution has been obtained in both photographs of (3) from the time-gated ballistic imaging. The image contrast is poor at a later delayed gate time as shown in (4). Without the time gate in (2), the image was totally blurred Because of the high fiber constant of chicken breast tissue,the resolution obtained from the time-gated ballistic imaging in (B3) is poorer than that from (A3), Part of the nonuniformity of the image at a time segment can be accounted for by the laser beam nonuniformity, the sample:refractive index variation, and internal structures.

medium replaced by the clear water. The transmitted signal wavelength was 527nm and pumping pulse wavelength was 1054nm. The 527nm narrow-band filter was set in front of the ICCD camera. Two turbid medium samples were made of: (1) 3.5mm-thick human breast tissue, and (2) 3mm-thick fresh chicken breast tissue. The tissue was fit in two glass slide separated by 3.5mm and 3mm, respectively.

IV.3 Summary

Due to the multi-scattering in turbid media, FWHM of PSF (the size of point image) was broadened. The increase of FWHM of PSF reduced the gap depth in between image points and the neighbor points. Only the farther-separated points can be resolved for an acceptable contrast, i.e., the image resolution decreased. Using a early-time detection method, the FWHM of PSF through turbid media was smaller, which is equivalent to a higher image resolution. Meanwhile, in CW imaging, both the late-arrival diffusive noise and the true signal would be detected, which caused a fatter PSF, which result in decrease of the resolution.

Reference

1. R. J. Zdrojkowswi and R. L. Longini, "Optical transmission through whole blood", J.O.S.A. Vo.59, 898-904 (1969)
2. A. Ishimaru,"Limitation on image resolution imposed by a random medium"' Appl.

3. R. F. Lutomirski, "Atmospheric degeneration of electro-optical system performance"' Appl. Opt. 17, 3915(1978)

4. N. S. Kopeika, S. Solomon, and Y.Gencay,"Wavelength variation of visable and near in-fared resolution through the atmosphere: dependence on aerosol 2nd meteorological conditions" J. Opt. Soc. Am. 71, 892 (1981)

5. N. S. Kopeika, "Spatial frequency dependence of scattered background light: the atmospheric modulation transfer function resulting from aerosol", J. Opt. Soc. Am. 72, 548 (1982)

6. A. Zardecki, Siegfried A. W. Gerstl, and Janon F. Embury, "Multiple scattering effects in spatial frequency filtering", Appl. Opt. 22, 4124-4131(1984)

7. Y. Kusuo and A. Ishimaru, "Modulation transfer function and image transmission through randomly distributed spherical particles", J. Opt. Soc. Am., 12, 2330-2335(1985)

8. Willard H. Wells,"Loss of resolution in water as a result of multiple small-angle scattering", J. Opt. Soc. Am. 59, 686 (1969)

9. J. A. Moon, R. Mahon, M. D. Duncan, and J. Reintjes, Opt. Lett. **18**, 1591 (1993)

10. K. M. Yoo and R. R. Alfano, "Time-resolved coherent and incoherent components of forward light scattering in random media", Opt. Lett. 15, 320-322, (1990)

11. L. Wang, P. Ho, C. Liu, G. Zhang, R.R. Alfano, "Ballistic 2-D imaging through scattering walls using an ultrafast Kerr gate", Science, 253, 769-771 (1991)

12. L. Wang, Y. Liu, P. P. Ho, R. R. Alfano, "Time-resolved imaging of tissues" ed. B. Chance, in Proceedings OE/LASE SPIE 1431, pp97-101 (1991).

Chance, in Proceedings OE/LASE SPIE 1431, pp97-101 (1991).

13. L. Wang, X. Liang, P. P. Ho. R. R. Alfano, " Time and Fourier space gated optical imaging of thick turbid media", SPIE, 1888,(1993)

14. L. Wang, P. P. Ho. R. R. Alfano, " Time-resolved Fourier spectrum and imaging in highly scattering media", Appl. Opt. 26, 5043-5048 (1993)

15. R.R. Alfano, X. Liang, L. Wang, P. Ho, "The time-resolved imaging of translucent droplets in highly scattering turbid media", Science, 264, 1913-1915 (1994).

Chapter V

Spatial Fourier Analysis of Optical Imaging in Turbid Media

V.1 Introduction

Various methods[1-8] has been applied to reduce the diffusive noise component of the scattered light to improve the quality of an image through random scattering media. Due to the serious requirement to achieve a significant large dynamic range of over $\geq 10^{10}$ to image an object through highly thick turbid media, such as breast tissues, a simple time-gate approach can not achieve such a large dynamic range. In this chapter, a time and space gate has been developed based upon the determination of Fourier optical spectrum through turbid media.

To examine the spatial frequency distribution as a function of time from a turbid medium, the time-dependence of Fourier transform spectrum of the transmitted signal of turbid media was measured in a time-resolved 4F imaging system. The time-resolved spatial spectrum in Fourier spectrum transform plane (FSTP) will be studied in this section. This part of work is to use to the Fourier transformations to improve optical imaging. The Fourier transformation with an object hidden in turbid media will be developed as a scanning method.

When a plane wave illuminates an object, the light will be scattered into different directions in space. This scattered light from an object represents a spatial angular

frequency spectrum of the object shape. The angular frequency components can be displayed on the Fourier plane. The medium has its own spatial spectrum. A diffraction pattern consists of a series of different spatial frequency components on the Fourier plane. The object has it Fourier spectrum. The center of the diffraction pattern which comes from the collimated diffraction light represents the zero frequency DC component. The spatial region spread away from the central portion represents higher frequency components. The higher angular frequencies are located at larger radii on the Fourier plane. This pattern at the Fourier plane can then be backward-Fourier-transformed to the imaging plane to form a true image of the object.

As discussed in Chapter II, the spatial frequency is defined by[9]: $f_x = \Delta X/(\lambda f)$ (lines)/mm, where λ is the wavelength of the illumination laser; f is the focal length of the lens L; and ΔX is the half width at full maximum (HWFM) of the Fourier spectral profile at the back focal plane. For an object illuminated by a plane wave, the radius of the diffraction image is equal to: $\Delta X = f \Delta\Theta$, where $\Delta\Theta \approx \lambda/D$, is the angle of diffraction. The Fourier spatial frequency of an object is ~ 1/D.

V.2 Spatial Fourier Spectrum of Turbid Media

The spatial Fouirer spectrum of turbid media can be measured at Fourier transform spectrum plane of an imaging system. To reveal the difference of the spectrum pattern at early-time detection to that at later-time detection, a Fourier-Kerr imaging system was used.

V.2.1 Experimental method of time-resolved 4F system

An experiment was designed to show the time-resolved pattern distribution in FTSP for a pure diffusive media in this section. The time-resolved imaging system used to detect the spatial Fourier spectrum of turbid medium is shown in Fig.V.2.1.1.

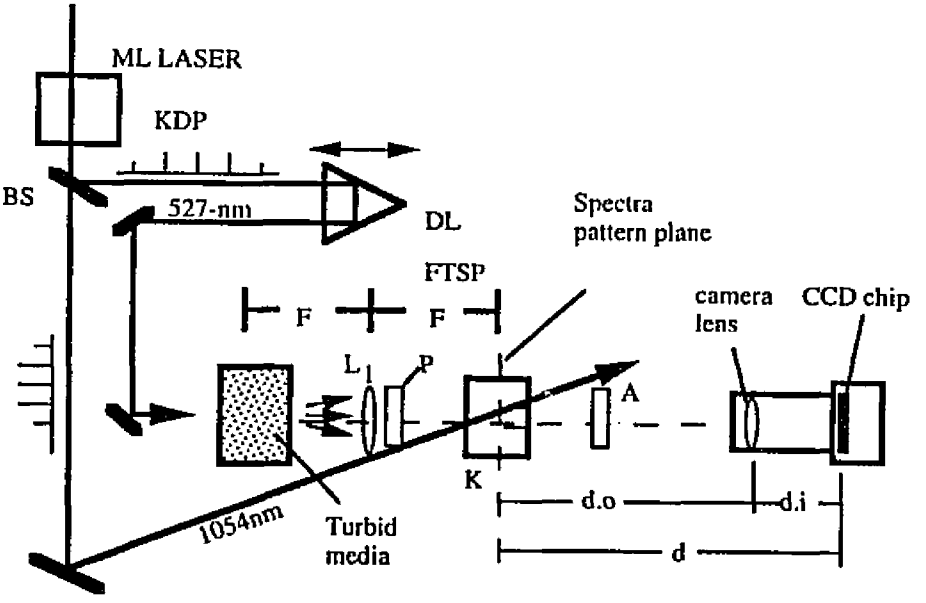

Fig.V.2.1.1 The time-resolved imaging experimental setup to detect the Fourier spectrum of clear water, Intralipid, and Polystyrene particle solution located at FTSP Wavelength :527nm. d = d.o + d.i, where, d.o is the diatance between spectra pattern and camera lens (object distance); d.i is the image distance. 527nm laesr beam size: 10mm.

In the setup, the middle plane of turbid media was placed at the front focal plane, and the Kerr cell was placed at the back focal plane of lens L_1 with L_f = 60cm. The size of the 1054nm pumping beam at FTSP was ~10mm. To image the Fourier spectrum of a turbid medium, the turbid medium sample was illuminated by a collimated laser pulse at 527nm. A intensity distribution of spatial Fourier spectrum was formed at FTSP (back-focusing plane of the lens L_1 after forward Fourier transform by lens L_1. Then the intensity distribution of which spectrum was imaged by a CCD camera located at distance of d.

To calibrate the spatial frequency at the Fourier transform spectrum plane with respect to the measured channels at the CCD, a 0.5mm-wide slit was placed at middle plane of the turbid sample (front focal plane, shown in Fig.V.2.1.1). The diffraction width of a 0.5-mm slit was formed at FTSP, and imaged by the CCD camera was ~ 20 channels (FWMH). The scale of spatial frequency at the back focal plane can be determined: given the input radius of the slit, D = 0.5-mm, the zeroth order spatial width and the maximum spatial frequency of the slit at the FTSP are $\Delta X = f \lambda/D$ = 60-cm x (527-nm/0.5-mm) ~ 0.63-mm and $f_x \sim 1/D$ = 2 lines/mm, respectively. Since the width of each CCD pixel is ~ 18-μm, the demagnification factor between the FTSP to the CCD plane is ~ [18-μm/channel x 20-channels]/0.63-mm = 0.56. Since the minimum resolution of the CCD is 2 channels, the smallest object size at the front focal plane to be resolved from our experimental setup is ~ 1-mm x (2-channels/20-channels)~ 0.1-mm.

Three types of turbid samples were used to demonstrate the above concepts: 1) 0.25% concentration polystyrene particle of the diameter 11.9μm solutions; 2) 1% intralipid solution; and 3) a clear water for reference. Each material was filled within

a 2.54-cm x 2.54-cm x 4.5-cm transparent cell. The optical path length was 2.54-cm. A 1054-nm laser pulse with diameter ~12mm was used as a gating pulse to open the Kerr shutter. The time-resolved Fourier transform spectrum (TRFTS) images (the intensity patterns of spatial Fourier transfer spectrum) of the input 1-cm diameter collimated 527-nm laser beam through three turbid samples were measured.

V.2.2 Experimental results

Experimental results of 0.25% 11.9μm Polystyrene particle solution and 1% diluted Intralipid solution are shown in Fig.V.2.2.1a and b, respectively. Fig.V.2.2.1(a-I) and (b-I) were detected at T=0, and (a-II) and (b-II) were detected at T=40ps. The spatial spectrum was much broader at the later time (sequence II). Fig.V.2.2.1c represents a reference TRFTS images in which clear water was used to replace the turbid medium. The corresponding digitized 1-D intensity profiles of TRFTS images of Fig.V.2.2.1 are displayed in Fig.V.2.2.2. The HWFM of the central peak in Figs.V.2.2.2a-I, 2b-I and 2c were ~8, 12, and 4 channels corresponding to the beam radius of ~ 144-μm, 216-μm, and 72-μm, respectively. The largest diffusive spectrum displayed in Fig.V.2.2.1b-II was ~ 125 channels which corresponds to an image size at the FTSP to be 2 x (125-ch x 18-μm/ch)/0.56 ~ 8-mm. The image field size was limited by the opening of the entrance window opening of the first polarizer of the Kerr gate.

The TRFTS image of the water sample does not have higher spatial frequency wing-distribution around the central peak as that from the turbid media because that in clear water test, only the collimated laser beam transmitted onto FTSP, and focused at the

center. In turbid media test, besides that the ballistic photons formed a central peak, a small amount of diffusive photons caused a wing. The appearing of diffusive photons at early detecting time is due to the finite ~8ps duration time of gating pulse.

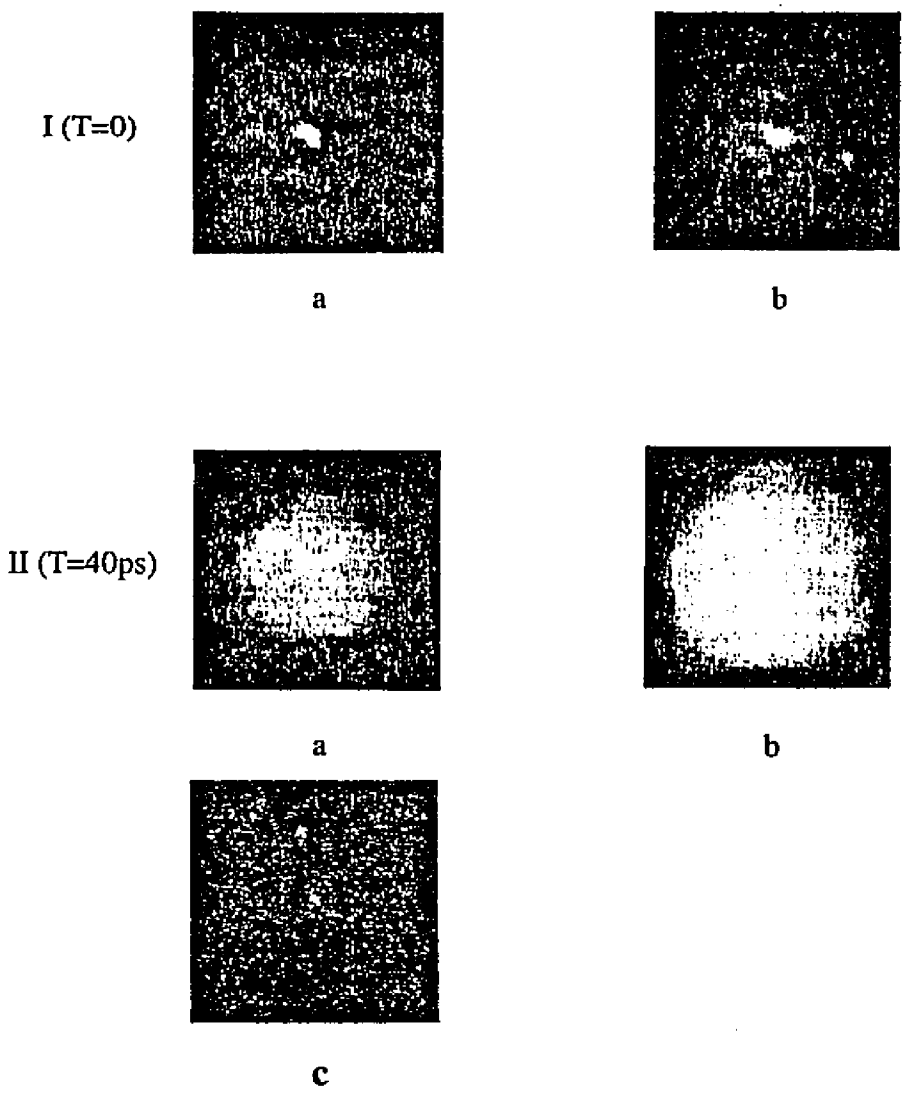

Fig.V.2.2.1 The time-resolved images of the Fourier spatial spectrum of turbid media and clear water: a) Dia. 11.9um Polystyrene particle solution; b) 1% dulited Intralipid solution.

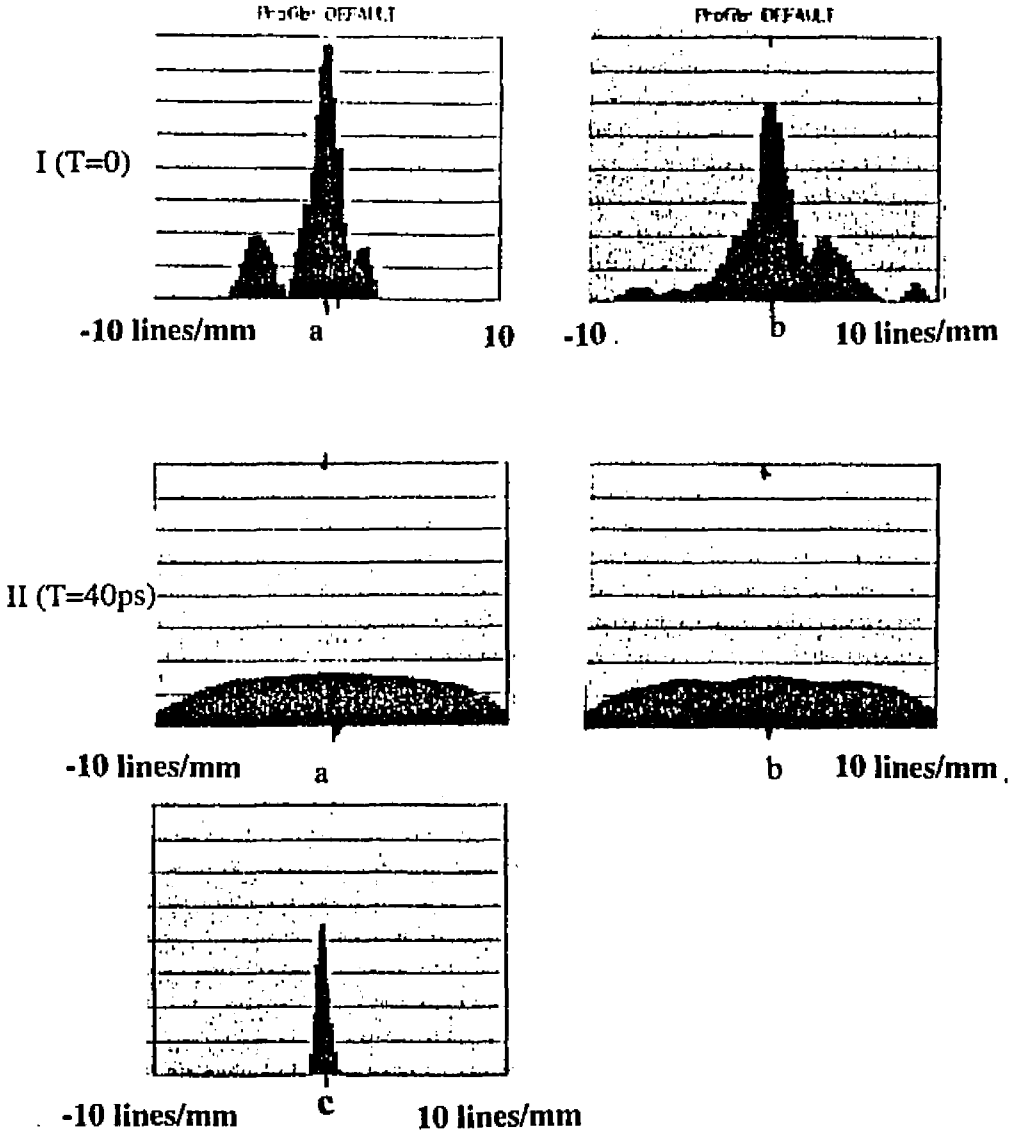

Fig.V.2.2.2 The digitized intensity profiles of the Fourier spectrum of turbid media and clear water: a) Dia. 11.9um Polystyrene particle solution; b) 1% dulited Intralipid solution.

The measured spot size of 72-μm from clear water in Fig.V.2.2.1c is spread out to 216-μm at T = 0-ps from the 1% diluted Intralipid solution in 1b-I. The most possible reason for which is larger number of the snake photon was detected at early gating time, which widened the peak due to their small deflection angles.

The wing-distribution of the intensity profile from the 11.9μm polystyrene beads solution is narrower than that of the intralipid solution. This difference in distribution may be accounted for by the different size-distribution of particles in the intralipid and bead solution: from ~0.2μm to ~1μm for the former, and 0.46μm for the later. Therefore the Intralipid solution caused the higher spatial frequencies (i.e., located at the wider range at FTSP) distribution.

At earlier-gating time T=~0, most energy of the transmitted signal is located in the central spot at the Fourier plane. A quantitative comparison of this feature is extracted from the digitized intensity profiles of Figs.V.2.2.2a-I and b-I. This FTS formed at the back-focal plane indicates the peak intensity mainly consists of a small-divergence-angle (~0.2°) diffraction light which is the ballistic and snake transmitted light. The earlier light represents the zero- and the low- spatial spectrum frequency components. Two weak side lobes around the central peak are shown in the earlier-gated Fourier spectra in Figs.V.2.2.2a-I and a-II. The side loops are the contribution of higher Fourier frequency ballistic/snake signals from the turbid medium. At the later gating time T=20ps shown in Figs.V.2.2.1a-II and b-II, the later-arrival diffusive light with the spherical wavefront formed an uniform intensity distribution at the FTSP. In a transparent medium, such as clear water with nearly no light scattered, the transmitted light appears on the Fourier

plane as a point image. The finite size of the measured spot is determined by the detector's finite resolution. A spatial Fourier filtering technique coupled with the ultrafast time gating imaging has the capability to greatly improve the dynamic range and signal-to-noise ratio. The measured spatial spectrum mainly depends on the size and the type of a hidden-in object. This dependence could be used to distinguish the different hidden-in objects. For example, the spatial frequency of small tumor objects with dimensions in the order of 0.1 to 1-mm embedded in a turbid medium (tissues) consisting of smaller scattering particles of dimensions on the order of 1 to 10-μm is significantly different and can be filtered out at the Fourier plane. The spatial frequency (~ 1/object size) of the tumor objects at the Fourier transform spectrum plane is lower than that from the surrounding small random particles, e.g., cells. The spatial dimension of the gating laser pulse radial profile can induce a spatial aperture at the Kerr cell to effectively remove the higher spatial frequencies. In this manner, information from the surrounding random small particles can be removed while the lower spatial frequencies from the tumor is transformed. The different type of hidden-in objects also cause different spectrum, such as the difference between a scattering object and a absorption object hidden in turbid media. A scattering object usually changes the spectrum of turbid media more than that done by a same-size absorption object.

V.3 Spatial Fourier Spectrum of Turbid Media with Embedded-in Objects

The spatial Fourier spectra depends on the size of the object. When an object hidden-in a turbid medium, the spatial variation of the optical parameters between the object and its surrounding media formats the information of a image of the object. The meida would have its own Fourier spectrum. The spatial Fourier spectra of the media and the object at FTSP are different temporally and spatially. The major component of the image information of the object can be discriminated using a spatial filter set at FTSP. At the early gating time, the ballistic/snake part of the diffraction light modulated by the region will form an undistorted Fourier spatial spectrum. Due to the larger spatial size of the phantom, its Fourier spectrum will be situated more near at the central area of FTSP. At later gating times, the diffusive scattering light arrives and spreads around the whole FTSP to form a quasi-uniform spatial noise distribution.

For a turbid medium with a hidden-in object, the spatial Fourier spectra will build up from these two types of media in different ways. The spatial variation of the optical parameters between the object and its surrounding media can be distinguished. Using a collimated light illumination, the diffraction light from each of these regions will form a specific pattern at FTSP. At the early gating time, the ballistic/snake part of the diffraction light modulated by the region will form an undistorted Fourier spatial spectrum. Due to the larger spatial size of the phantom, its Fourier spectrum will be situated at the central area of FTSP. At later gating times, the diffusive scattering light arrives and spreads around the whole FTSP to form a quasi-uniform spatial noise

distribution.

V.3.1 Experimental method

The difference between the Fourier spectrum measurement and the 4F Fourier imaging measurement is the location of lens L_2 and CCD camera. When L_2 was located at the focal length from FTSP, Fourier image was obtained at the image plane at the focal distance away from L_2. For the Fourier spectrum measurement, L_2 was located as a regular image lens to collect the spectrum at FTSP to the CCD following 1/object + 1/image = 1/f. A 0.1mm width slit immersed in a turbid medium cell was used as hidden-in object. A 0.5% concentration 0.46μm polystyrene particle solution filled in 4cm thick cell. A 527-nm laser beam was used as the turbid medium. The spectral patterns formed at FTSP was imaged by a cooled CCD camera as a function of gating time T. For the imaging measurement, a test grid with 1-mm space located in front of a 2.54-cm x 2.54-cm x 4.5-cm cell filled with 1% Intralipid solution was used for all cases.

Schematic diagram of experimental setup to measure Fourier spatial spectrum of an object hidden in a turbid medium is shown in Fig.V.3.1.1. F: focal length; L: Fourier transform lens; FFP: front focal plane; S: scattering particles; BL: ballistic light; SL: scattering light; CL: collimated illumination light; TM: turbid medium; FTSP: Fourier transform spectrum plane (or back focal plane). The sample preparation: a 0.1mm slit, simulated as an object hidden in 0.5% Intralipid solution filled in 5cm transparent cell.

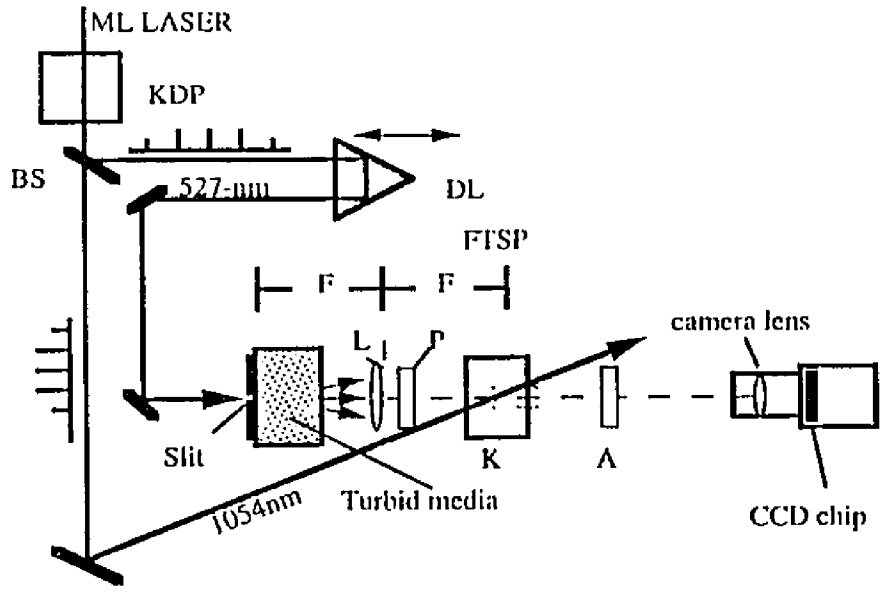

Fig.V.3.1.1 The time-resolved imaging experimental setup to detect the Fourier spectrum of a 0.1mm slit behind the Intralipid, and Polystyrene particle solution located at FTSP Wavelength :527nm.

V.3.2 Experimental results

The time-resolved Fourier spectrum images of 0.1mm slit in a turbid medium are shown in Fig.V.3.2.1: a) T=0; b) T=6.6ps; c) T=13.3p; d) T=40ps. At T=0, the spectrum image is shaped as a horizontal spreading diffraction pattern, which corresponded to the vertically-oriented slit. Because the most diffusive photons did not arrive yet, the diffraction pattern of the slit was not distorted. When the gating time was delayed at T=6.6ps, the diffraction pattern was gradually distorted by the diffusive light. At T=40ps, the pattern was totally blurred, and the pattern was buried by the scattering noise background. The diffraction pattern distortion of the slit shows that most spatial frequency components would not be blurred at early time, which can insure the early-time image a best quality.

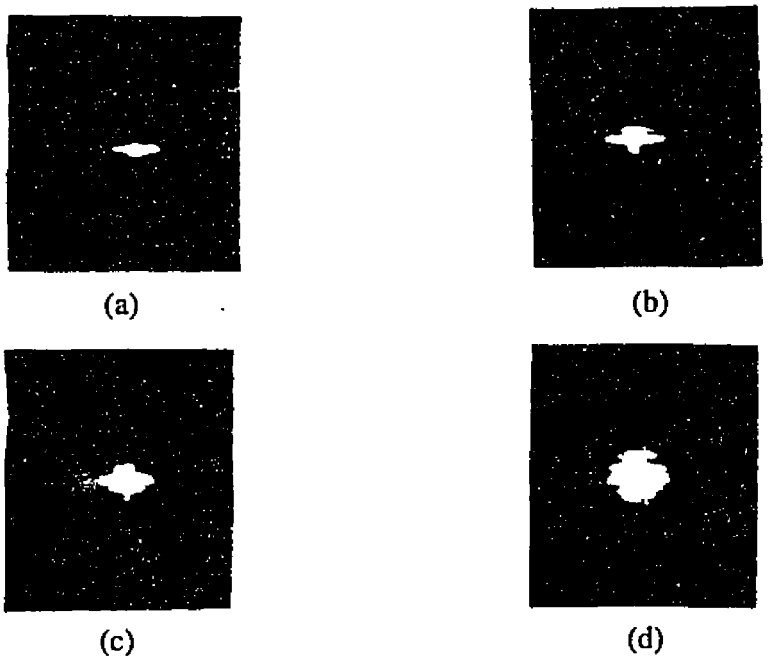

Fig.V.3.2.1 The time-resolved Fourier spatial spectrum of a 0.1mm slit through 40mm-thick 0,5% Polystyrene solution . The slit was set vertically. a) T=0; b) 6.6ps; c) 13ps; d) 40ps.

V.4 Aperture Dependence of Image Contrast in CW Measurement

An aperture with a small size (small NA) has been widely used in the optical information process[9] and the collimation detection in the optical signal transmission[10-12]. To improve the quality of an image detected in turbid media, the temporal and spatial responses of a imaging system must be examined. Experimental results have shown that the image contrast of an object hidden in highly turbid media can be improved using a small-size aperture[13-15], which is a low-pass spatial filtering function of the aperture. In

this chapter, two problems related to the spatial filtering effect of an aperture will be described: (1) the image contrast/resolution distributions as a function of the aperture size at the FTSP; and (2) the temporal intensity distribution of the transmitted photons through turbid media as a function of the aperture size at FTSP.

V.4.1 Aperture Dependence of Image Contrast

The contrast improvement provided by an aperture at back focal plane is based on the concept of the spatial Fourier spectrum and the modulation transform function (MTF) in turbid media (MTF was discussed in Chapter II). When a highly scattering turbid medium exists in an imaging process, the main energy of a true signal is carried only by the early-arrival ballistic/snake photons. At Fourier transform spectrum plane (FTSP, the back focal plane of the Fourier transform lens), the collimated (ballistic/snake) photons concentrate at the center and its neighbor area (DC and the lower frequency range). The non-collimated (diffusive) photons distribute at the whole FTSP due to the nature of the spherical wave of the diffusive scattering photons caused by scatters (scattering light sources) inside turbid media. When the dimension of a hidden-in object to be resolved is much larger than that of the scatters of turbid media, the image contrast can be effectively improved by using a smaller-size aperture at FTSP.

In the transmission through turbid media, the higher frequency components met much greater attenuation. The basic reason for which was that the major power of the scattering noise distributed also in the higher frequency range, which buried the higher frequency components of the true signal.

V.4.1.1 Experimental Method

To examine the image contrast improvement of an space Fourier filter used in a conventional transillumination method, a CW-F imaging experiment was designed to image the testing bar chart samples in Intralipid solution as shown in Fig.V.4.1.1. The space filter was made by setting a mechanical aperture in FTSP. The window of the mechanical aperture was adjusted to ~1.5mm, ~2.5mm, ~5mm, ~8mm, and ~12mm. The contrast of bar charts detected in a clear water was 100% used as a reference. A 1054nm laser beam was used as a probing beam. Three different bar charts with the resolving widths of ~0.25mm, 0.5mm, and 1mm, have been tested. Turbid medium was made by diluted 10%-Intralipid solution by 50-times (2%) and filled in a 55mm-thick transparent cell. The bar chart was placed at the middle of the cell.

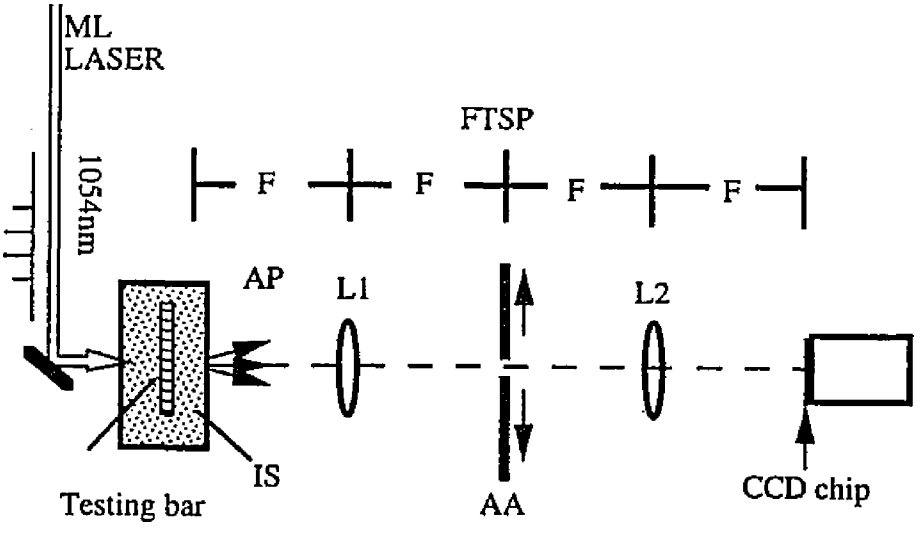

Fig.V.4.1.1 Experimental setup to determine the contrast of a testing bar chart in turbid media as a function of the size of the Fourier spatial aperture. L1=60cm; L2=20cm.

V.4.1.2 Experimental Results

The image contrast detected by a CW-F imaging is plotted in Fig.V.4.1.2 as a function of the aperture diameter of the spatial filter from the three different phantom testing bar charts of widths ~0.25mm, 0.5mm and 1mm on a glass slide used as the hidden objects immersed in the middle of a 5-cm thick 2% diluted Intralipid solution. When the aperture was reduced from ~15mm to ~2.5mm, the image contrast was improved by ~170% in all three bar widths. The contrast decreased with the resolution increased from 1mm, to 0.25mm. The reducing rate was about 17±5%. For instance, the contrast of 1-mm, 0.5-mm, and 0.25-mm bar width using a 4-mm aperture are 64%, 57%, and 44%, respectively. When the aperture diameter was less than 2mm, the image contrast starts to be lower in all bar widths. This reduction of the image quality can be accounted for by the lower signal level and the cutoff frequency from the spatial filtering.

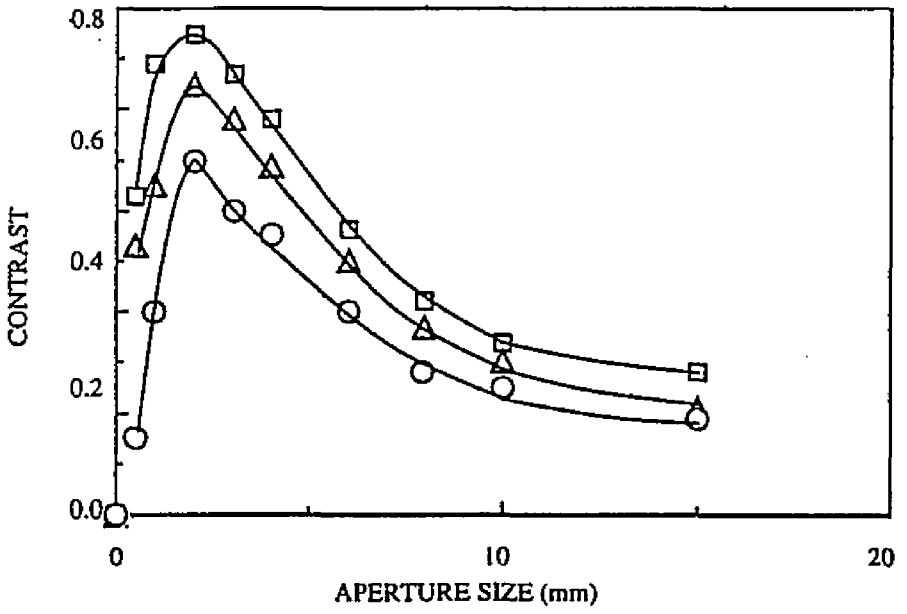

Fig.V.4.1.2 The contrast distribution of 1mm (□), 0.5mm (△) and 0.25mm (○) resolution bars in 2% diluted Intralipid solution. as a function of the aperture size.

V.4.2 Aperture Dependence of Temporal Intensity Distribution

For a turbid media sample, the measured results of the temporal intensity distribution depends on the measuring system. Due to the different spatial response of an small-size aperture to the ballistic/snake parts and to the diffusive part of the transmitted signals, the temporal intensity distribution will be a function of the aperture size. The different response of an aperture to the ballistic/snake and to the diffusive scattering photons can be used to improve the image contrast.

Due to the fact that the major power of the ballistic/snake and diffusive photons appear at different range in Fourier spectrum plane (FTSP), a proper-size aperture set in a time-resolved system would improve the degrading of the detected image. In a time-resolved experiment using a Kerr-Fourier imaging system with a small-size induced aperture, the diffusive component was filtered out, and the faster pulse profile was obtained, which was examined by a streak camera test.

V.4.2.1 Experimental method and setup of time and space gate

To demonstrate the shape change of temporal intensity profile by adding a spatial filter in time-gate imaging system, three different types of time-gated imaging system have been used: a regular Kerr gate system, a Kerr-Fourier system with a size-limited "soft aperture" at FTSP, and a streak camera system. Here, the size-limited soft aperture is made by an intensive laser beam in CS_2 liquid of Kerr cell. This "soft aperture" would only appear in Kerr cell for a short period of time when the gating pulses exist in CS_2. When the size of gating beam is changed by a mechanical aperture, the size of the "soft

2mm. A 527-nm laser beam was used as a probing light. A grid chart with 1mm-separation was imaged, which was placed in a 25mm-thick cell filled with diluted 10%-Intralipid by 100-times (1%). The collection solid-angle was same as ~2° for both two systems. A conventional Kerr gating imaging system and a Kerr-Fourier imaging system are shown in Fig.V.4.2.1.1 and Fig.V.4.2.1.2 separately.

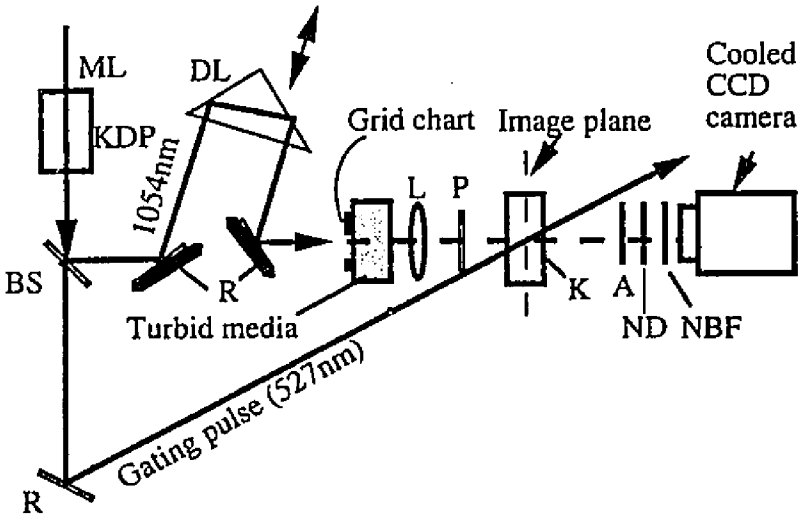

Fig.V.4.2.1.1. A picosecond optical Kerr gated imaging system:

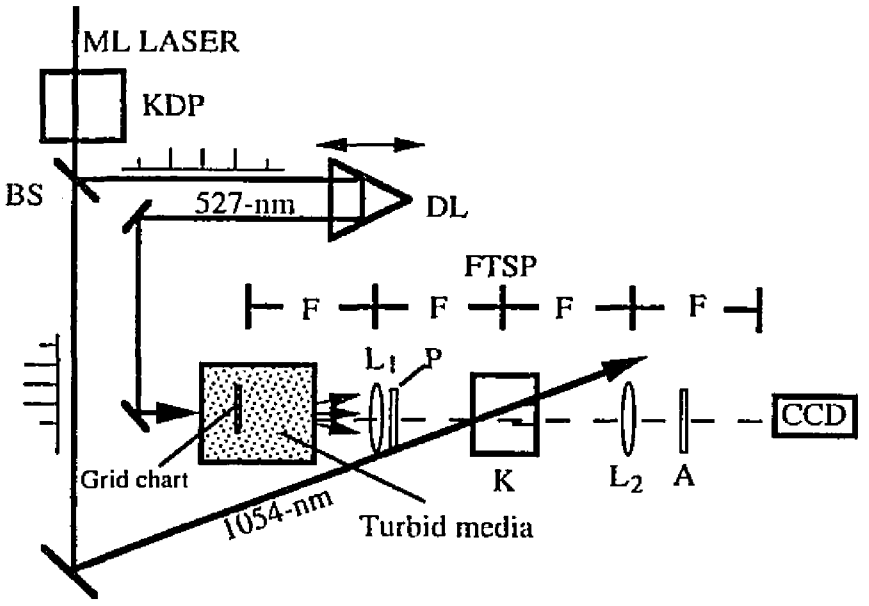

Fig.V.4.2.1.2 Picosecond Kerr-Fourier time-spatial imaging system.

The aperture dependence of the temporal distribution has also been demonstrated by a series experiments using a streak camera. The setup is shown in Fig.V.4.2.1.3. In the experiment, a 4F collection optics was built, and an adjustable mechanical aperture was set at the Fourier spectrum plane. A single 527-nm laser pulse was used as the probing light. The turbid medium was made by a diluted 10%, 2%, and 0.4% of Intralipid-10% solutions filled in 2mm, 10mm, and 50mm glass cells, respectively.

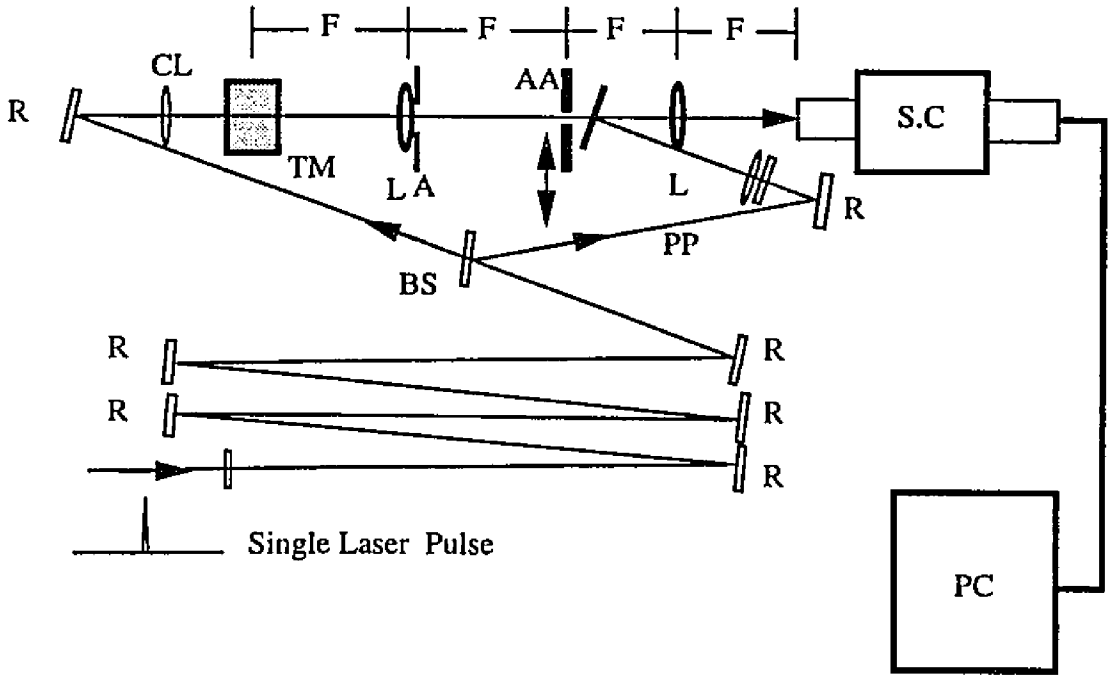

Fig.V.4..2.1.3 Experimental setup to detect temporal intensity profiles using a sreak camera. R: mirror; TM: turbid media made of Intralipid suspension; CL: beam collimating lens; L: Fourier transform lens; A: input aperture: AA: adjustable aperture; PP: prepulse; BS: beam splitter; SC: sreak camera; PC: personal computer.

V.4.2.3 Experimental results

Results of the temporal transmitted image signal of a 527-nm laser pulse from the transparent part of a testing grid passed through scattering media detected by a Fourier-Kerr gate and a conventional Kerr gate are plotted in Fig.V.4.2.3.1 as a function of gating

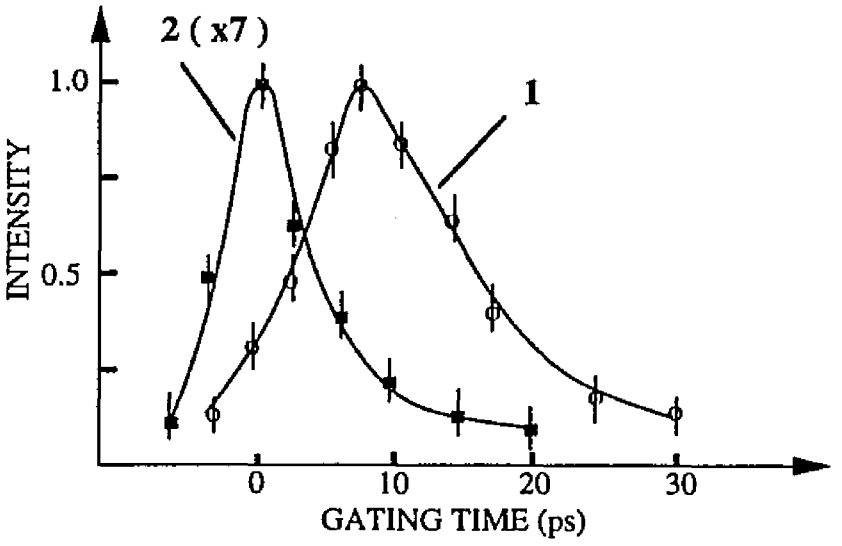

Fig.V.4.2.1.3 Temporal distributions of 1-mm grid placed inside 1% of Intralipid-10% filled in a 25-mm thick cell imaged by a Kerr (curve 1) imaging system and a Kerr-F (curve 2) imaging system with ~2.5mm induced aperture.

time. The signals are represented by curves 1 and 2, respectively. The curve 1, by a Fourier Kerr imaging system, and the curve 2, by a conventional Kerr imaging system. The intensity of the curve I has been magnified 7 times for comparison.

The signal transmitted through the Fourier-Kerr gate was chopped. After ~13-ps, most of the diffusive scattered light was removed by a space gate. For a conventional Kerr gate, due to the limited capability to remove the diffusive noise, the peak of the transmitted signal appeared at ~ 8-ps later and the overall temporal profile was much broader (~ 80-ps). The temporal Kerr intensity profiles displays some difference between the data measured by the conventional the Kerr and the Kerr-F imaging system.

broader (~ 80-ps). The temporal Kerr intensity profiles displays some difference between the data measured by the conventional the Kerr and the Kerr-F imaging system. Temporal Kerr-Fourier intensity profile (curve 2) consists of mainly snake/ballistic components centered at T = 0-ps. In this case, the selection of low spatial frequencies picks out early time components of output signal. Most of the diffusive component was removed by the added Fourier spatial filtering: a soft aperture at FTSP. However, the standard Kerr gate profile (curve 1), on the other hand, displays the more of diffusive components, peaking later and over a wider time spread. The Kerr Fourier gate reduces the diffusive light by removing late-time tail.

The results shown in Fig.V.4.2.3.1 were checked using a streak camera with a resolution of 7.5ns/mm to measure temporal profile passing through scattering media in 4F arrangement with different aperture sizes. The normalized temporal profiles of 527nm laser pulses transmitted through the 50mmx0.4% sample at aperture sizes of 1mm, 3mm, and 10mm are shown in Fig.V.4.2.3.2. It can be seen that the profile of 10-mm aperture was broadened and peak-delayed compared to that of 1-mm aperture. The curve displayed in Fig.V.4.2.3.2 shows that the 1mm aperture significantly filtered out the diffusive photons in late time domain, and made the profile much narrower. A aperture works as a temporal gate when the diffusive light exists.

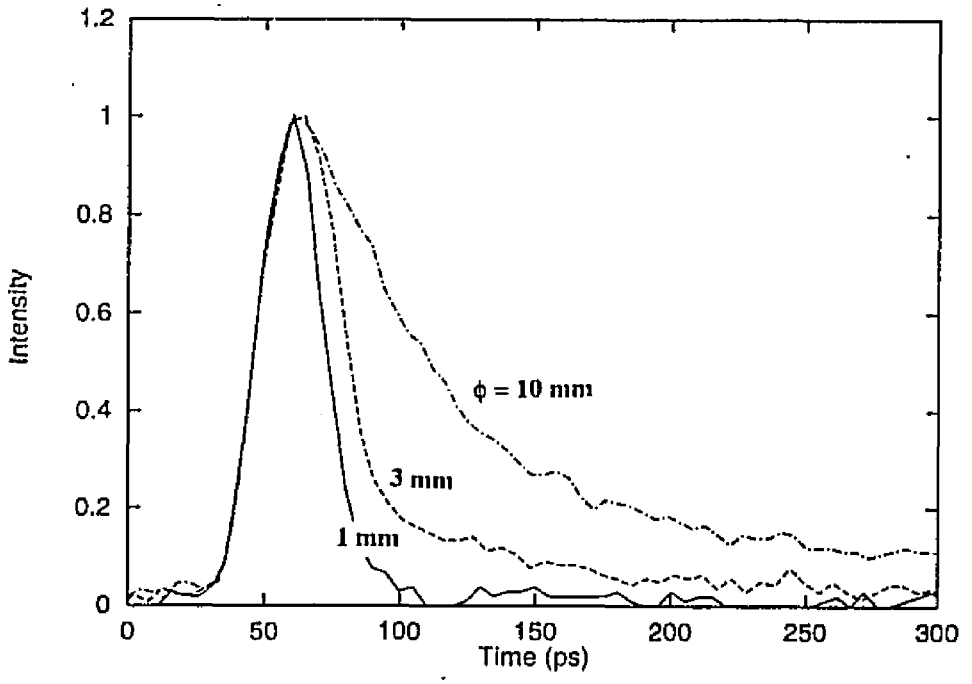

Fig.V.4.2.3.2 The temporal profiles of the laser pulses scattered by 50mm x 0.4% Intralipid solution. As the diameter of the spatial Fourier filter changed from 10mm to 1mm, the pulse duration of the scattered pulse reduced significantly.

V.4.2.4 Conclusion

The spatial filtering provided by an aperture at FTSP in an imaging system can improve the image contrast of an object hidden in highly scattering turbid media when the dimension of the object is larger than that of the scatters. The contrast of image can be improved either using a temporal/spatial or a CW spatial Fourier gate by filtering out the most of diffusive scattering photons at the Fourier plane. With the combination of the time and space filtering, the image quality can significantly be improved using only a space gate, which works as a time gate. When aperture size is too small, the image resolution of fine structures of a hidden-object would be obviously worsen due to the loss of the higher spatial frequency components. A space gate acts as time gate for diffusive light. A space gate removes diffusive light which occurs late in time.

V.5 Aperture Size Dependence on Image Contrast in Time-Resolved Imaging

Since the information carried by the ballistic/snake photons is non- or less-distorted than that by the diffusive photons, the higher image contrast and SNR appeared at T=0, or close to T=0. The contrast and SNR image formed by late-arrival diffusive photons would be lower. The highest contrast and SNR appeared approximately at the same time as that the ballistic/snake component. In this section, the contrast distribution are determined using a time-gated (Kerr) and a time-space-gated (Kerr-F) imaging systems.

V.5.1 Comparison of Image Contrast Achieved by Conventional Kerr imaging system to Kerr-Fourier Imaging System

This part of experiment was concentrated on the comparison of the contrast improvement between a conventional Kerr gated and a Kerr-Fourier systems as shown in Fig.V.5.1.1 and Fig.V.5.1.2. In Fig.V.5.1.2, images of 0.25mm and 1mm bar charts placed in 0.35% of Intralipid-10% solution filled in a 5.5cm cell. A 527-nm laser pulse was used as a probe. For different detecting time T, the size of 1054-nm gating beam was changed by a mechanical aperture in five steps: ~1.5mm, ~3mm, ~5mm, ~8mm, and ~12mm. When the aperture size was set 12-mm, the setup worked like a conventional Kerr gated imaging system. As the aperture size was set the smaller, the contrast was increased. At a early-gating time. This contrast increase was achieved by both time- and space-gates. At the later time, the contrast increase was done mainly by the space gate.

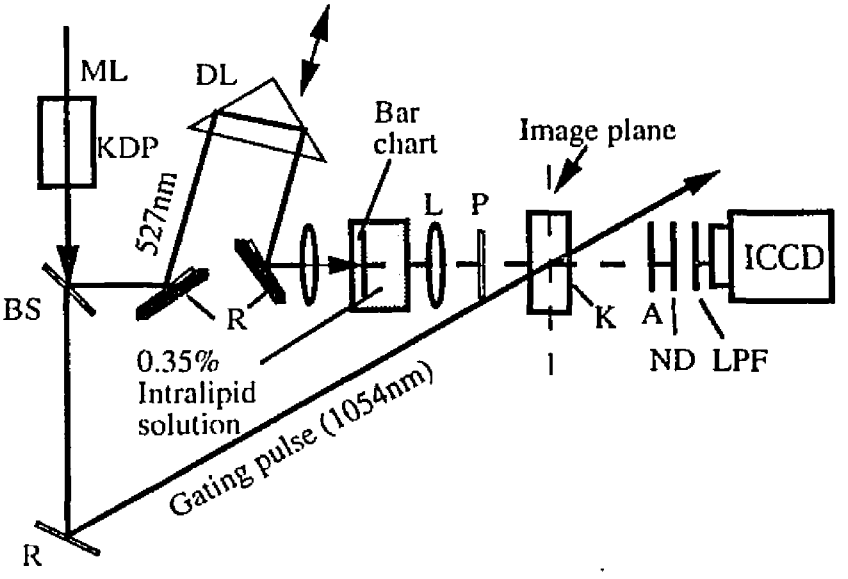

Fig.V.5.1.1 A conventional Kerr gated imaging system to determine the contrast distribution as a function of time. B: 0.25mm / 1mm bar charts; T: 0.35% diluted Intralipid solution; Cell thickness: 5.5cm; wavelength: 527nm; 1054nm pumping beam size: ~12mm.

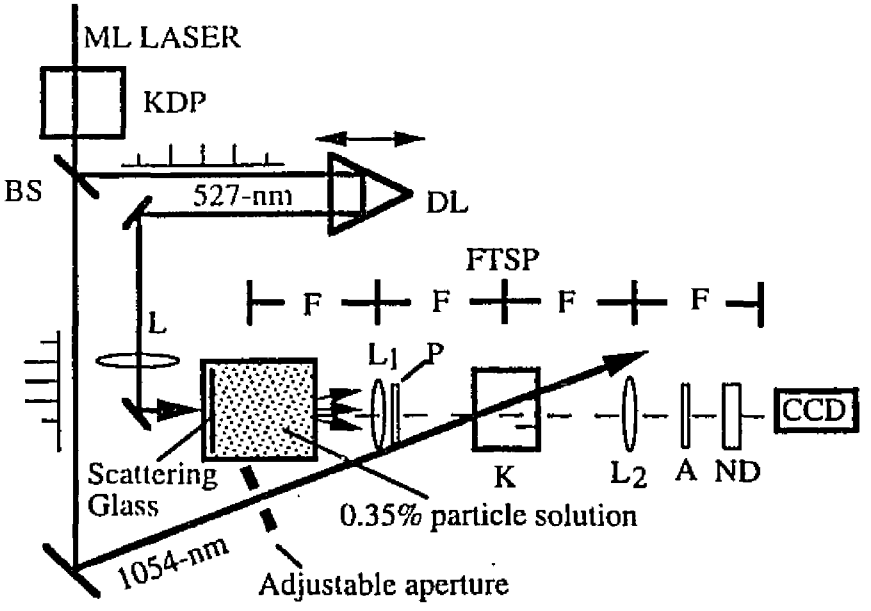

Fig.V.5.1.2 A Kerr-Fourier imaging system to determine the contrast distribution as a function of time and aperture size. B: 0.25mm / 1mm bar charts; T: 0.35% diluted Intralipid solution; Cell thickness: 5.5cm; wavelength: 527nm; 1054nm pumping beam size: ~1.5mm, ~3mm, ~5mm, ~8mm, and ~12mm.

The measured results of contrast distributions as a function of the "soft aperture" size in different gating time obtained is displayed in Fig.V.5.1.3. The curves 1 and 2 represent the contrast of 1mm and 0.25mm bar charts detected at T=0, respectively. The curves 3 and 4 represent the contrast of 1mm and 0.25mm bar charts detected at T=~26ps. The curves 5,6 are the calculated contrast as function of the aperture size in clear water, which are used as references. There were several points have been revealed from this result:

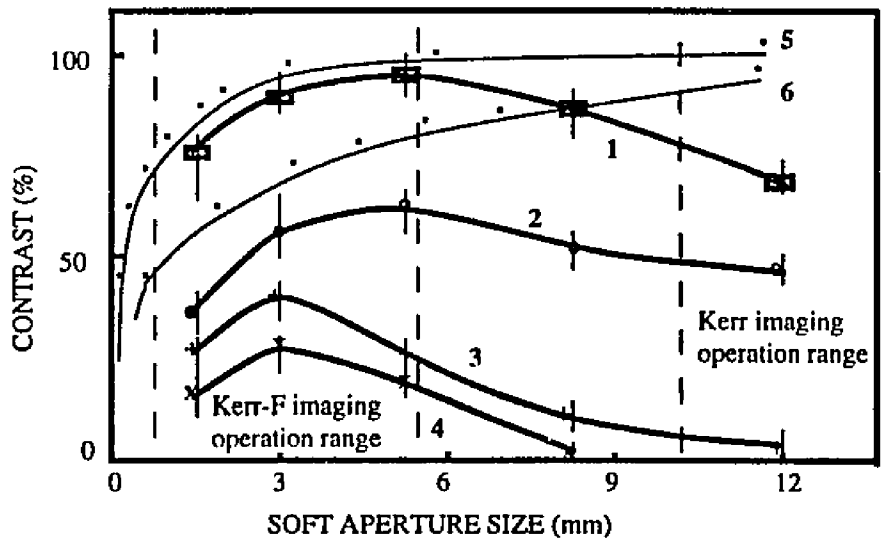

Fig.V.5.1.3 Contrast dostribution as a function of a soft aperture size gated at T=0 and ~21ps. Turbid medium cell thickness: 55-mm; theconcentration of Intralipid: 0.35% (of Intralipid-10% suspension). Probing wavelength: 527nm. 1) T=0 and 1mm-bar-chart; 2) T=0, and 0.25mm-Bar-chart; 3)T= ~21ps and 1mm-bar-chart; 4)T=~21ps and 0.25mm-bar-chart; 5) calculated contrast of imm-bar; 6) calculated contrast of 0.25mm-bar.

1) At an early imaging time as shown by curves 1 and 2, the contrast improvement caused by the size of the aperture was not large as it does at later imaging time, as shown by curves 3 and 4. At early-gating time, the major component was dominated by the ballistic/snake photons. These photons concentrated at the center of FTSP, and would not be affected greatly when the aperture size was increased over ~3mm. The maximum contrast was ~95% at 3mm, the minimum was ~75% at 1.5mm and 12mm. The decrease rate is about 21%.

2) At the late gating time T=~21ps as shown by curves 3 and 4, a contrast peak appeared when aperture size was ~3mm. After 3mm, the contrast of 0.25mm dropped fast down to zero at ~8mm. For 1mm bar, the contrast dropped in a long tail with a contrast ~5%. When gating time T=21ps (Because the measured result was a convolution of 10ps-WWHM gating pulse and ~8ps-WWHM probing pulse. Therefore, the gating time T=21ps was still setting inside the probing pulse duration , which corresponded to the ~10ps, the half-Max.height of pulse), the diffusive component increased quickly. These diffusive photons spread at higher frequency range, that is the larger radius area of FTSP. In this case, the contrast at a small aperture (as in Kerr-F system) was still ~40% for 1mm-bar, and ~25% for 0.25mm-bar, shown by curves 3 and 4, respectively. When the aperture was increased to 12mm Dia., these diffusive photons passed the aperture and spoiled the contrast. This is the case happened in a conventional Kerr imaging system.

V.6 Application of Space-Time Gate in Imaging Through Turbid Media

As an application of the Kerr Fourier imaging system in turbid media, two actual time-resolved images of 0.25mm-bar are displayed in FIg.V.6.1: (b) soft-aperture size ~3mm, (d) soft-aperture size ~12mm. Their intensity profiles are shown in (a) and (c) respectively. The contrast of the image detected at T=0 (Fig.d) is about 25%, and the image detected at T=21ps is completely spoiled by the light noise (refer to Fig.V.6.1b).

Experimental results have verified that the early ballistic/snake transmitted light from turbid media appeared to be located at the zero- and lower spatial components at the Fourier transform plane. The improvement of the image recognition of hidden objects is mainly determined by the lower spectrum response under earlier-parallel-propagated rays located at the center zone of the diffraction spectrum plane of the turbid medium from a collimated illumination. A portion of the diffusive light is collimated after a transformation lens and impinges nearly uniform onto the back-focal plane at later time. The contrast of the time and spatial Kerr-gated ballistic image is improved through selective filtering of the lower Fourier frequencies of the scattered light. A proper-aperture-limited-time-resolved gate set at the spectrum plane can reject most of the noise diffusive light and improve the dynamic range, image contrast and S/N. This improvement is greatly paid by a loss of sharpness.

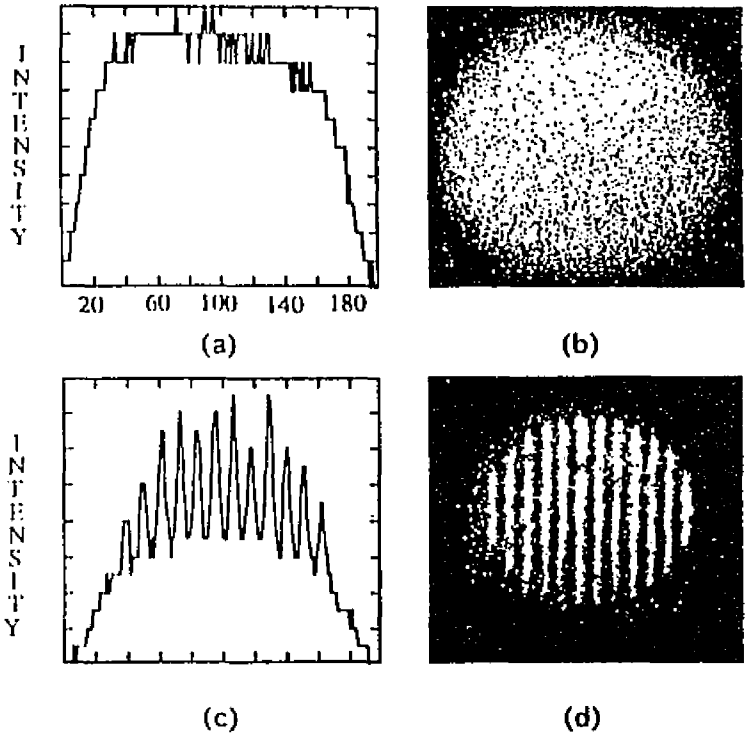

FIG.V.6.1 Time-resolved images of 0.25mm-bar-chart set inside 0.35%-Intralipid-10% solution detected by a K-F imaging system at T=-20ps with an aperture size: (b): 15mm, (d): 1.5mm. (a) and (c)are the profile of the images in (b) and (d), respectively.

References

1. J. Fujimoto, S. De Silversti, E. Ippen, R. Margolis, A. Oseroff, "Femtosecond optical ranging in biological system" Opt. Lett. 11, 150-152 (1986); Science, "Optical coherence tomography" 254, 1178-1182 (1991).

2. H. Chen, Y. Chen, D. Dillworth, E. Leith, J. Lopez, J. Valdmanis, "Two-dimensional imaging through diffusing media using 150-fs gated electronic holography techniques", Opt. Lett., 16, 487-489 (1991)

3. A. Rebane and J. Feinberg, "Time-resolved holography", Nature, 351, 378-380 (1991)

4. K.G. Spears, J. Serafin, N.H. Abramson, "Chrono-Coherent Imaging for Medicine",

IEEE Trans. Biomed. Eng. 36, 1210-1221 (1989); N. H. Abramson and K.G. Spears "Single pulse light-in-flight recording by holography", Appl. Opt., 28 1834-1841 (1989)

5. B. Chance, J. Leigh, J. Miyake, D. Smith, S. Nioka, R. Greenfield, M. Finander, K. Kaufmann, W. Levy, M. Young, P. Cohen, H. Yoshioka, R. Boretsky, "Comparison of time-resolved and un-time-resolved measurements of deoxyhemoglobin in brain", Proc. Nat. Acad. Sci. 5, 4971-4975 (1988)
6. S. Anderson-Engels, R. Berg, S. Svanberg, O.Jarlman, "Time-resolved transillumination for medical diagnosis", Opt. Lett. 15, 1178-1180 (1990)
7. J. Lakowicz and K. Berndt, "Lifetime-selective fluorescence imaging using an rf phase-sensitive camera", Rev. Sci. Instrum., 62, 1727-1735 (1991)
8. L. Wang, P. Ho, C. Liu, G. Zhang, R.R. Alfano, Science, 253, 769 (1991)
9. J. Goodman, "Introduction to Fourier Optics", McGraw-Hill Book Co., New York (1968)
10. Hugo J. van Staveren, Christian J. M. Mose, Jan van Marle, Scott A. Prahl, and Martin J. C. van Gemert, "Light scattering in Intralipid-10% in the wavelength range of 400-1100nm", App. Opt. 4507-4514(1991).
11. Christian J. M. Mose, Martin j. C. van germert, Jan van Marle, Willem M. Star, Jonhannes P. A Marilnissen, and Scott A. Prahl, "Measurements and calculations of the energy fluence rate in a scattering and absorbing phantom at 633nm", **Appl. Opt.** 12, 2292-2296(1989)
12. I. Driver, J. W. Feather, P. R. King, and J. B. Dawson, "The optical properties of

aqueous suspensions of Intralipid, a fat emulsion", **Phys. Med. Biol.** 12, 1927-1930(1989)

13. L. Wang, P. Ho, X. Liang, H. Dai, R. Alfano, "Fourier-Kerr Imaging in Thick Turbid Media", Optics Letters, 18 241-243 (1993).

14. L. Wang, X. Liang, P. P. Ho, R. R. Alfano,"Time and Fourier space gated optical imaging of thick turbid media", SPIE, 1888, (1993)

15. L. Wang, P. P. Ho. R. R. Alfano, " Time-resolved Fourier spectrum and imaging in highly scattering media", Appl. Opt. 26, 5043-5048 (1993)

Chapter VI

Image Contrast as A Function of Illumination Intensity Density

VI.1 Introduction

Using more intense illumination has been used to enhance the image contrast in X-ray. This enhancement was reduced by a requirement to reduce the dose to the patient as far as possible to avoid a risk associated with ionizing radiation. For X-ray imaging technology, the spatial resolving capability is seriously limited in the detection of small hidden objects in vivo. The minimum dose to visualize an object increases as the inverse fourth power of the size of the object[1] (~ the maximum spatial resolution), i.e., resolution α E^{-4}, where E is the exposure dose. The minimum dosage to detect a 1-mm diameter hidden object will be 10^4 times more than that to detect 1-cm diameter hidden object.

For optical radiation in diagnosis, there is no known safety hazard to human tissues using red light under low energy density illumination. The data from an experimental study performed at Commonwealth University, Los Almos Laboratory, and NIH in 1974, the laser energy, peak power, and peak intensity used in a picosecond time-resolved imaging measurement are well within the safety directly human beings. In their study, the threshold injury for the use of picosecond laser pulses directly illuminating the retina of monkeys in vivo was ~67GW/cm^2 or ~2J/cm^2.

A formula from ANSI Z136 (American Standard Institute) also has been used to estimate the maximum safety for dosage caused by optical energy in exposure time duration t:

$$I = 1.7t^{1/4}\ (J/cm^2) \qquad (VI.1.1)$$

For instance, for t=15 seconds $1.7(15)^{1/4} = \sim 3.3 J/cm^2$ is maximum energy density allowed to be applied in human skin.

When an optical image signal was detected by a CCD device, the detection noise (major part is quantum mottle) would be added to the electronic image signal. Since the number of photons detected per unit area of the detector is a Poisson process, the added noise of output electronic image by CCD detector is proportional to the square root of the exposure dose: $I_{noise} \propto E^{1/2}$,[1,2]. The SNR will be improved proportionally to a ratio of $E/E^{1/2} = E^{1/2}$, where E is the exposure dose or intensity of input optical signal, i.e., $S/N = E^{1/2}$. Therefore, the higher illumination intensity produces a better SNR and higher contrast in the output electronic image signal.

This approach has been a major way to improve detection sensitivity of an optical transilluminational imaging technology, such as diaphanography. When the SNR of input optical signal is low (higher noise level), the higher illumination intensity source won't necessarily achieve an expected improvement of image contrast and SNR. In this chapter, an experiment has been done using time-resolved and CW imaging system to determine the exposure intensity dependence of image contrast improvement in turbid media.

VI.2 Experimental Method

Experiments were performed to study the intensity dependence of the contrast at 1054nm wavelength, and compare it to that at 527nm wavelength.

In the first part, three tests have been done to investigate the intensity dependence of contrast by measuring a resolution target: (1) in a clear water using K-F system; (2) in 2% diluted Intralipid solution using K-F system; and (3) in a 2% diluted Intralipid solution using CW-F system. In the second part, two wavelengths laser light have been used to determine the wavelength effect onto the contrast enhancement rate as a function of input exposure on CCD chip.

Since there are several different types of noises affecting the SNR of an overall imaging system other than the quantum mottle in CCD chip, such as thermal noise of electronic circuits, stray light noise caused by imaging optics, the contrast improvement with increase of intensity may not follow formula $E^{1/2}$. Therefore an actual intensity dependence of contrast of the overall system had to been experimentally determined without turbid media (in a clear water). Which result was used as a reference. The turbid medium was made by filling 2% diluted Intralipid solution into 50mm-thick transparent cell. The mean free transport path is l_t = ~5mm. The contrast calculated from images of a Air Force bar testing target with a 0.315mm-resolution bar. The experimental arrangements used here are similar as that used in the other imaging tests. In the measurement, neutral density filters were used to adjust the illumination intensity density onto the samples. To avoid the nonlinear intensity response of CCD chip, all input exposure on CCD chip was kept in between 100 - 1200 count readout. The contrast of

the image was limited at a lower range from 5% to 10%. Two reasons were considered to choose this lower contrast level: (1) a minimum acceptable contrast level; (2) avoid the non-linear response of CCD caused by too high transmittance level at the transparent range of a black/white bar chart. The Kerr Fourier images was detected at T=0. The pumping size of 527nm laser beam for Kerr-Fourier system was ~Dia.2.5mm. A 1054nm and 527nm laser pulses were used as a probing and gating beams, respectively. Before the tests, the leak signal for Kerr gate has been calibrated by adding a proper neutral density filters to eliminate the effect of fluctuation of noise background.

VI.2.2 Experimental Results and Discussions

The experimental contrast results as a function of the illumination intensity density in 2% diluted Intralipid solution at 1054nm is shown in Fig.VI.2.2.1. The dashed curve is the calculation from $E_{1/2}$. The black square data is actual measured contrast response as a function of input exposure in a clear water of CCD chip at 1054nm, which can be approximately matched by a function $E^{1/2.2}$. This shown there were unknown noise sources in the CCD camera, which reduced actual SNR and caused lower contrast response. The hallow square data is for the contrast response as a function of input exposure in diluted 2% Intralipid solution on CCD chip tested by a K-F imaging system at T=0. Which can be approximately matched by $E^{1/2.5}$. This higher rate of contrast enhance can be compared to the contrast response obtained by a CW-F imaging system with no aperture, where the contrast enhance rate is roughly as $E^{1/3}$. Which is

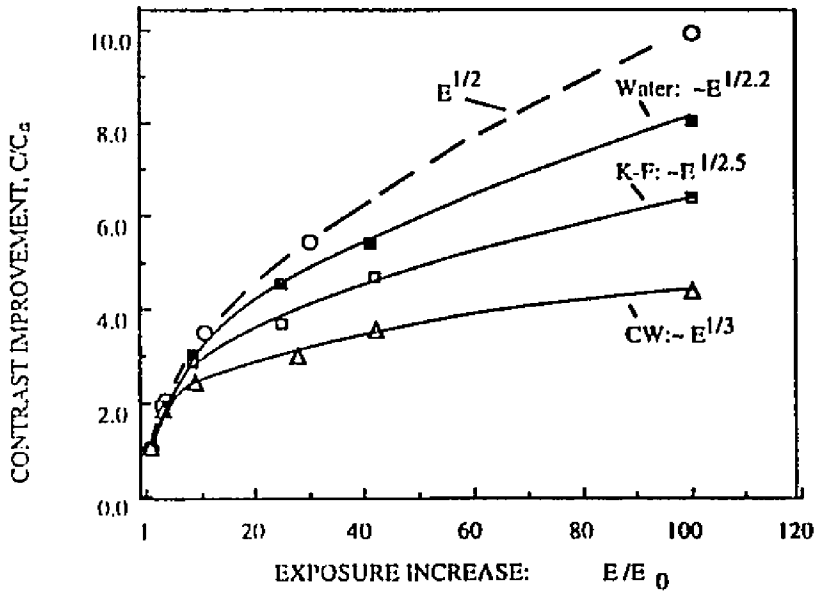

Fig.VI.2.2.1 The contrast improvement as a function of multification of CCD exposure intensity, E/E$_0$. E = 1.0, E$_0$ is the intensity of input optical intensity at CCD surface. O: Calculation from E$^{1/2}$.■ : Contrast improvement in a clear water. □ : 4F data of contrast improvement in 2% diluted Intralipid solution at T=0. △: CW data of contrast improvement in 2% diluted Intralipid solution.

showing when turbid media exists, the faster increase of contrast enhancement should be attributed to the less diffusive photons in detected signal by early-time detection using K-F system.

The experimental data of contrast enhancement as a function of input exposure for 1064nm and 527nm obtained by Kerr-F imaging system is shown in Fig.VI.2.2.2. The dashed curve is calculated by E$^{1/2}$. The black square and a hallow curves are for 1054nm and 527nm, respectively. Due to a low concentration of 0.4%, the 1054nm contrast response is about E$^{1/2.3}$ very close to that in a clear water, which is ~E$^{1/2.2}$ as shown in Fig.IV.2.2.1. Meanwhile, the contrast enhancement for 527nm wavelength in 0.4% Intralipid solution is much slower as E$^{1/2.6}$. The difference between two data can be attributed to the larger scattering coefficient μ_s at 527nm, which cause more seriously

crosstalk and the higher noise background level in whole detection area. This confirmed that the higher noise level of input optical signal would decreased the contrast enhancement of the output electronic signal as shown in the last experimental data shown in Fig.IV.2.2.1.

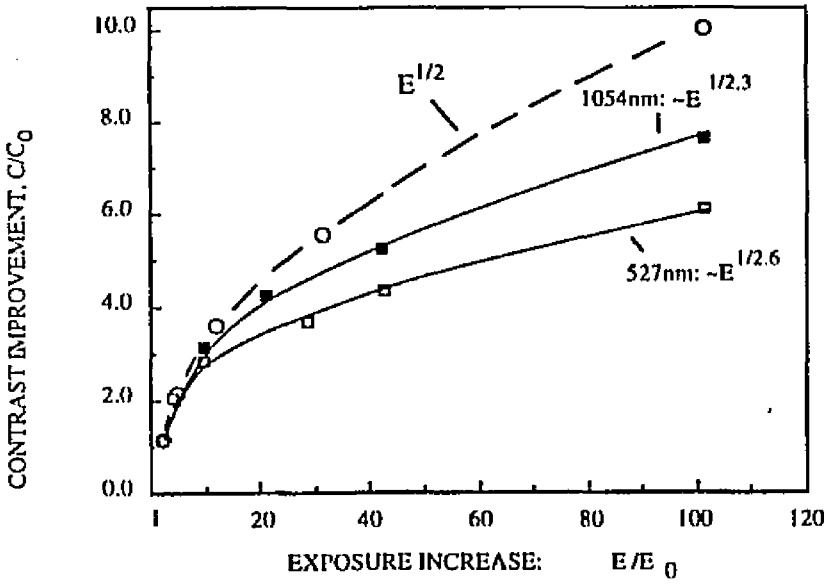

Fig.VI.2.2.2 The K-F contrast improvement as a function of multification of CCD exposure intensity, E/E_0 at 1054nm ■and 527nm□. E_0= 1.0, which actually corresponded to ~70 counts. E is the intensity of input optical intensity at CCD surface. C_0 is image contrast ~5-10%; C is the contrast with exposure increased. Concentration of Diluted Intralipid solution: 0.4% of stock, Cell thickness: 50mm. Dashed line, Q is a calculation from E1/2

The comparison of K-F curves at 1054nm in Fig.VI.2.2.1, where 2% Intralipid solution used, and Fig.VI.2.2.2, where 0.4% Intralipid solution used, shows the concentration effect onto the intensity dependence. K-F curves for 2% and 0.4% Intralipid solutions were fitted by $E^{1/2.5}$, and $E^{1/2.3}$. This graph shows when the concentration increased (the number of diffusive photons increased, the contrast enhancement by intensity was reduced.

VI.4 Summary

The SNR of the output signal from a CCD device is usually higher than that of the input optical signal because the signal increases faster than the noise background in CCD surface (Poisson process) when the input signal increases, i.e., SNR ~ $E^{1/2}$. In the imaging of an object hidden in turbid media, the image contrast depends on the illumination intensity in three ways: 1) the improvement rate of SNR is decreased with a increase of exposure in CCD input surface; 2) the decrease of SNR of input optical signal caused by diffusive scattering photons; and 3) the wavelength of the illumination light.

In CW imaging method, the increase of the illumination intensity would amplify both of the true image signal and the scattering diffusive noise. The contrast improvement is seriously affected by the extremely low SNR of the optical signal coming out from turbid media. The enhancement of the contrast as a function of input exposure was decreased faster than that for the early time measurement. In this case, the increase of the illumination intensity won't achieve an obvious improvement in the contrast.

To improve the contrast with the higher illumination intensity, the scattering noise must be removed as greatly as possible before they arrived at the detector using a early-time and space gate imaging method.

References

1. S. Webb, "The Physics of Medical Imaging", (IOP Publishing, New York 1990).

2. L. Levi,"Vision in communication", PROGRESS IN OPTICS, Vo.VII

Chapter VII

Imaging in Thick Turbid Media

VII.1 Object Location Influence of Image Contrast in Thick Turbid Media

When laser light travels through a turbid medium, the diffusive scattering photons act as a secondary light source to illuminate a hidden-in object. Other than the primary illumination from the input laser beam, this secondary source is a non-collimated point source and depends on the depth in the turbid medium. The intensities of these two types of light source change rapidly with different depths inside turbid media. A regions closer to the input surface of turbid media, there are more ballistic/snake photons, and less diffusive photons, while a regions closer to the exiting surface of turbid media, the diffusive photons are much more than the ballistic/snake photons. The transmitted image signal is less distorted for the object located closer to the exiting surface than that to the input surface. Both factors determine the quality, contrast, and SNR of the detected images. In this section, the contrast of hidden objects at different locations in a highly scattering Intralipid solution has been investigated and experimentally measured.

VII.1.1 Experimental Method and Setup

Three different test black phantom bar charts of width 0.25-mm, 0.5-mm, and 1-mm

on a glass slide were used as the hidden objects merged into the intralipid solution at different depths. When the test chart was located at the entrance window and the exit window of the sample cell, the depth was defined to be zero and 5.5-cm, respectively. In each measurement, two bar charts: a and b in horizontal and vertical directions were inserted into the intralipid solution in two different depths as shown in Fig.VII.1.1.1. Test bars in two different directions and two depths

were simultaneously measured to improve the accuracy of data calculation.

Test bar charts hidden in a 5.5-cm thick 2.5% intralipid solution of transport length of 2.4-mm were measured as a function of depth and object size using steady state and picosecond Kerr Fourier imaging systems.

The schematic diagram of the Fourier-Kerr gate imaging system is shown in Fig.VII.1.1.2. The imaging system consists of three main parts: laser source, optical Kerr gate, and detector.

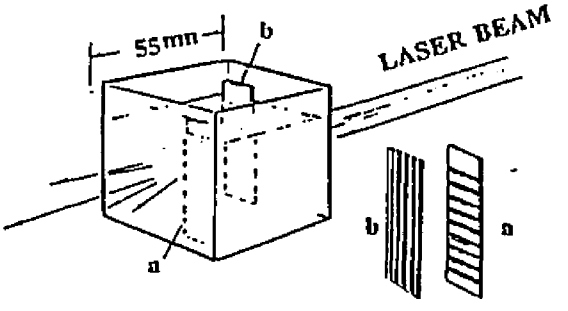

Fig.VII.1.1.1 The sample design

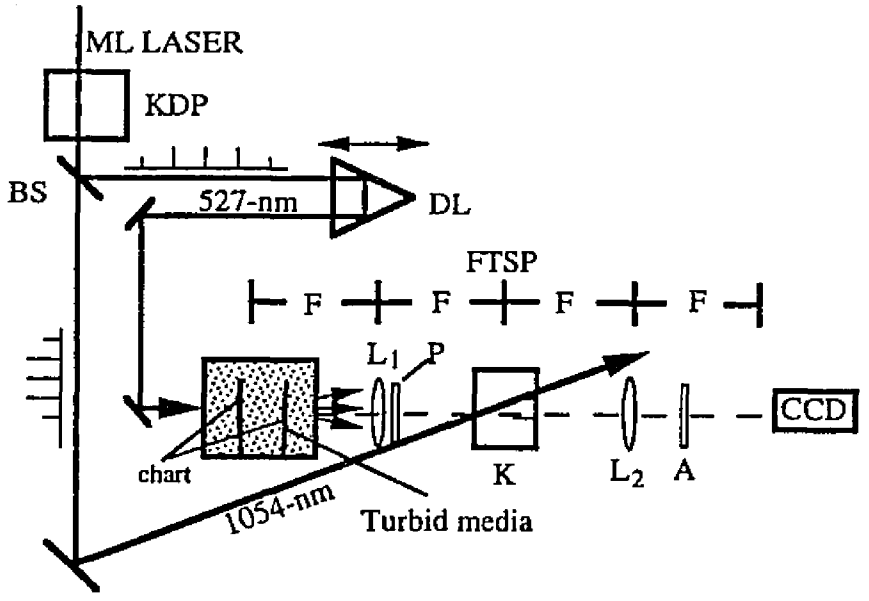

Fig.VII.1.1.2 The experimental setup of Kerr Fourier imaging system.

Essentially, in Kerr-Fourier imaging system, the signal from the turbid sample located at the front focal plane[1,2] of the lens L_1 was collected and transform to the Kerr cell located at the back focal plane (FTSP in Fig.VII.1.1.2). The focal length of L_1 used in this experiment was 60-cm. The spatial filtered and temporal segmented signal of the phantom is imaged by L_2 onto the CCD camera for display. This is a standard 4F Fourier imaging where the Fourier spectrum was transformed by L_1 onto FTSP and the image was obtained after the transformation of the Fourier spectrum by L_2. A picosecond mode-locked Nd^+ glass laser system which emitted 1054-nm 8-ps laser pulse train was used as the illumination source and its second harmonic 527-nm was used as the gating source. For small scattering particles, optical scattering from the 1054-nm inside the turbid

medium was reduced by 16 times (~ $1/\lambda^4$) over that from the 527-nm beam. The total energy of the amplified 1054-nm laser output which consists of a train of ~ 100 laser pulses was ~ 500-mJ. The illumination beam size was about 1-cm^2. The peak power density of the 527-nm gating pulse was ~100-MW/cm^2 per pulse and the duration ~ 8-ps. The Kerr gate consists of a pair of calcite crossed polarizers and an 1-cm CS_2 filled Kerr cell. The extinction ratio of the Kerr gate was ~ 10^5 and the transmission efficiency was ~ 10%. A transparent sample cell with inside dimension of 7.5 x 5.5 x 5.5 cm^3 (optical path = 5.5-cm) was filled with 2.5% intralipid solution. The transport mean free path of this modeled turbid medium is ~2.4-mm which is similar to transport scattering length of human breast tissues[3,4]. A cooled CCD camera system controlled by a Mac IIci from Photometrics Inc. was used to detect the gated image.

VII.1.2 Experimental Results

Two photographs of the time-space gated images of the 1-mm bar chart at T = 0-ps and 15-ps are displayed in the lower portion of Fig.VII.1.2.1 with the contrast to be ~ 0.85 and 0.55, respectively. The signal intensity level at T = 15-ps was ~ five times lower.The contrast is defined as a ratio of maximum difference, (I_{max} - I_{min}), to the summation of variation and the background, (I_{max} + I_{min}), of an image signal:

$$C = (I_{max} - I_{min})/(I_{max} + I_{min}) \qquad \text{(VII.1.2.1)}$$

And the corresponding signal-to-noise ratio for the image of a clear-black bar chart is:

$$I_{max}/I_{min} = (I_{bright\ bar} - I_{background})/(I_{dark\ bar} - I_{background}) \qquad \text{(VII.1.2.2)}$$

It was ~ 20 at T = 0-ps and was ~ 4 at T = 15-ps. The location of the time T = 0-ps was determined when the test bar chart was inserted into the sample cell filled with clear water.

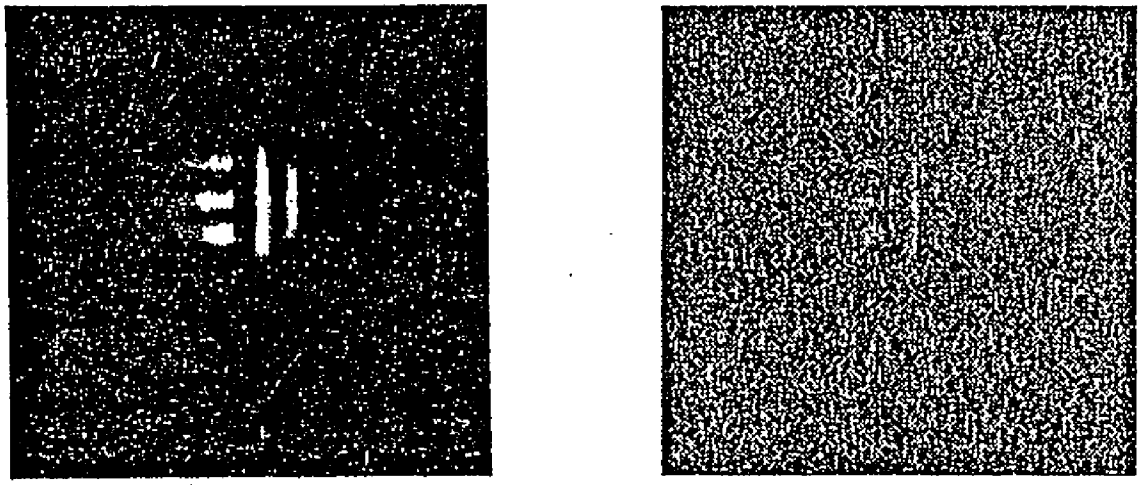

(a) (b)

Fig.VII.1.2.1 The blank points are Kerr time gated data and the solid points are cw (no time gate) data. The dashed lines and solid lines of eye guided curves. For time-gated images, all the data were measured at the gating time = 0-ps. When the gating time = 15-ps, the contrast of each measurement is ~ 80% of the contrast value at T = 0-ps. The vertical axis is the image contrast of the opaque bars where the contrast = 100% is defined to be the measured contrast of the bar merged in a clear water cell. The horizontal depth axis is the location of the bar chart from the entrance window, e.g. bar phantoms at the entrance window of the 55-mm cell is defined to be the depth = 0. Each data point is an average of ~5 measurements with ±5% error bar.

The measured contrast in these three test bars at five different depths in 50mm-thick cell filled with 2% diluted Intralipid solution were calculated and averaged from the measured images at T = 0-ps and 15-ps, the contrasts are displayed in Fig.VII.1.2.2a and 2b, respectively. The image contrasts at gating time = 0-ps (ballistic signal) are plotted as the blank squares, triangles, and circles in Fig.VII.1.2.2a. At the later gating time of

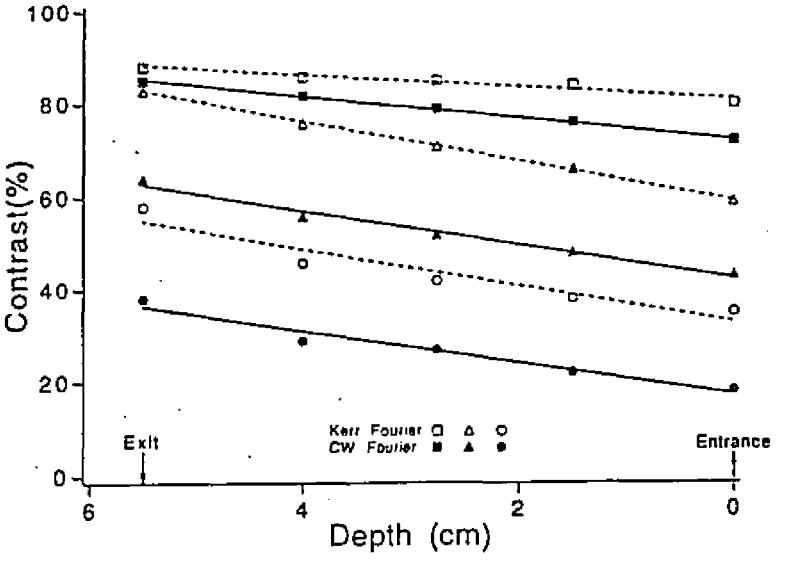

Fig.VII.1.2.2a The image contrast of 1-mm (squares), 0.5mm (triangles), 0.25mm (circles) bars detected at T = 0ps as a function of the sample location in 2% diluted Intralipid solution.

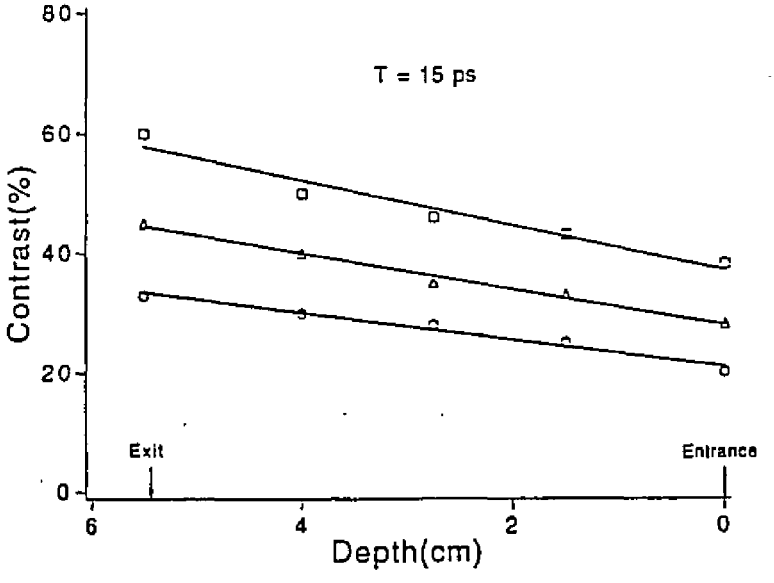

Fig.VII.1.2.2b The image contrast of 1-mm (squares), 0.5mm (triangles), 0.25mm (circles) bars detected at T = 15ps as a function of the sample location in 2% diluted Intralipid solution.

~ 15-ps (snake signal) in Fig.VII.2.2.2b, the image contrast of the time-gated imaging was slightly reduced by a factor of ~20% of that measured at 0-ps. Furthermore, the measured contrast of cw-Fourier (no Kerr gate) spatially filtered images with ~2.5mm mechanical aperture are plotted as the solid squares, triangles, and circles in Fig.VII.1.2.2a for comparison. The CW-Fourier images were obtained with the same experimental setup shown in Fig.VII.1.1.2. except the two polarizers of the Kerr gate were set in the parallel direction (the time gate was turned off). Similar to the absorption gating technique, the diffusive background light was significantly reduced by the Fourier spatial filtering. The signal-to-noise ratio, in parallel to Figs.VII.1.2.2a and 2b, of these three test bars at five different depth at T=0-ps and 15-ps are displayed in Figs.VII.1.2.2c and 2d, respectively.

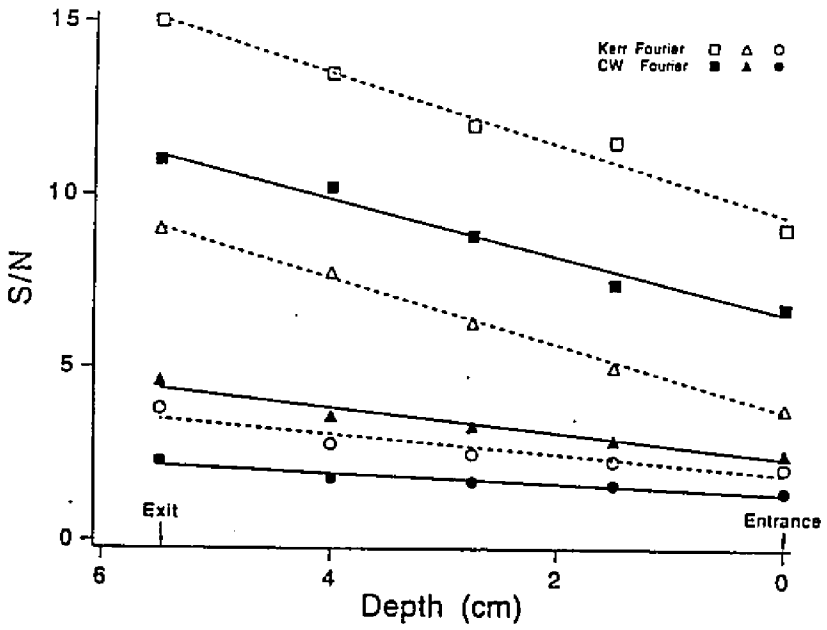

Fig.VII.1.2.2c The image SNR of 1-mm (squares), 0.5mm (triangles), 0.25mm (circles) bars detected at T=0ps as a function of the sample location in 2% diluted Intralipid solution.

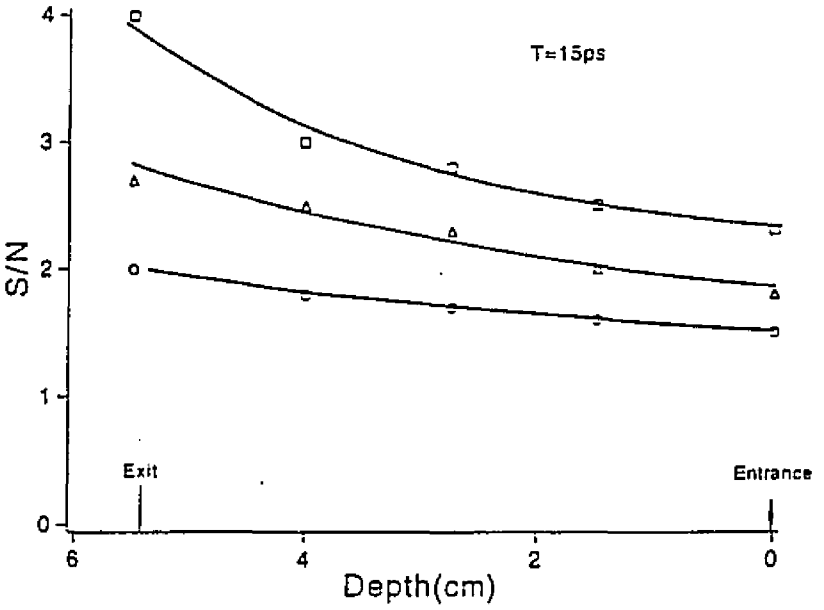

Fig.VII.1.2.2d The image SNR of 1-mm (squares), 0.5mm (triangles), 0.25mm (circles) bars detected at T=15ps as a function of the sample location in 2% diluted Intralipid solution.

The minimum detectability of the time gated signal level is about 10 counts per pixel above the dark current level. The peak intensity of the image through the intralipid solution was ~ $1.5x10^{-10}$ of the incident 1054-nm laser beam which was calibrated with a set of neutral density filters. This transitivity is consistent with the calculated early signal ~ exp[-(optical path/transport length)] = exp[-(55-mm/2.4-mm)] ~ $1.1x10^{-10}$.

The salient feature of Fig.VII.1.2.2 indicates that in all cases studied the contrast and the S/N increased when the depth was increased (close to the exit window) and the contrast was higher for the time gated image. In addition, the contrast and S/N were lower for the smaller bar width. The contrast and S/N curves at different depths were smoother for the time gated image than that from the ungated image. When the bar width was reduced, the improvement of the time gate was larger. For instance, the contrast

improvement between the object located at the exit plane and the entrance plane is ~ 10% for 1-mm bars and ~ 95% for the 0.25-mm bars for Kerr-Fourier over cw-Fourier imaging.

With the improved S/N, a 250-μm spatial resolution of hidden bars in a 5.5-cm 2.5% intralipid solution has been obtained from the time and spatial gated Fourier Kerr imaging. The image contrast of the 250-μm bars varies from 58% at the exit plane to 35% at the entrance plane. The contrast reduction ratio between the front to exit plane was ~ (58%-35%)/58% ~ 40%. When the width of the bar was increased, the contrast was increasing and the difference at different depth was reducing. For the 1-mm bar, its image contrast varies from 88% to 80% at the exit and entrance plane, respectively which corresponds to a ~ 8% reduction. While for the 500-μm bar, its image contrast varies from 86% to 59% or a 27% drop.

Under some severe cases such as the object is located at the front part of the turbid medium or an ultra-small object with poor signal level, the combination of time and space gating can significantly improve the image contrast.

The contrast obtained from all CW-Fourier measurements was worse than that from Kerr-Fourier measurement. When the bar width is ≥ 1-mm, the difference between cw- and Kerr-Fourier imaging was not significant. However, for bar size = 1-mm, the contrast was 88% for Kerr-Fourier image and 87% for cw-Fourier image at exit plane; for bar size= 0.5-mm, the contrast was 80% for Kerr-Fourier image and 72% for cw-Fourier image; and for the bar size of 250-μm, the Kerr-Fourier gated image contrast was about twice better than that of the cw-Fourier image. In addition, the time gate on the image

contrast was more significant for objects located at the entrance window than that for objects at the exit window.

The time-resolved image contrast of three test bar charts from the Fourier-Kerr gate at T = 15-ps is plotted in Fig.VII.1.2.2b as a function of object depth. These graphs are similar but are poorer than the contrasts obtained at T = 0-ps for the three bar widths. The contrast for three bar widths at T = 15-ps was slightly decreased (~ 80% of the peak value) from the contrast obtained at T = 0-ps. This measured contrast at T = 15-ps obtained from the Kerr-Fourier imaging is much better than that obtained from a conventional Kerr gate. Due to the incomplete removal of the diffusive scattering noise, the measured contrast at 15-ps from the conventional Kerr gate dropped to ~10% of the peak contrast value obtained at 0-ps. The signal to noise ratio was reduced to ~ 1.2 at T = 15-ps from ~ 5 at T = 0-ps. While for the Fourier-Kerr gate, since there was less scattering noise, the S/N at 15-ps dropped to the level of 25-50% from that of 0-ps in all cases shown in Figs.VII.1.2.2c and 2d.

The quality of image improvement through temporal and spatial Kerr-Fourier gate is obtained from the collection of the ballistic/snake signal with most of the diffusive scattered noise light filtered out at the Fourier plane. Under some severe cases such as the object is located at the front part of the turbid medium or an ultra-small object with poor signal level, the combination of time and space gating can significantly improve the image contrast. The temporal and spatial gated Kerr-Fourier imaging has shown a significant improvement over the conventional time-gated Kerr imaging or the spatial gated imaging alone. These measurements further reveal the direction to follow for

optical systems to perform breast cancer screening.

Test bar charts hidden in a 5.5-cm thick 2.5% intralipid solution of transport length of 2.4-mm were measured as a function of depth and object size using steady state and picosecond Kerr Fourier imaging systems. With the improved dynamic range, signal to noise ratio, and spatial resolution offered by time and spatial gated imaging, a 250-μm width bar in thick highly scattering medium was resolved at the signal level attenuated to ~ 10^{-10} of the probe light.

References:

1. L. Wang, P. Ho, R. Alfano, "Time-resolved Fourier Spectrum and Imaging in Highly Scattering Media"Appl. Opt. 32 5043-5048 (1993)
2. J. Goodman, *Introduction to Fourier Optics,* (McGraw-Hill Book Co., New York, 1968).
3. C. Moes, M. van Gemert, W. Star, J. Marijinissen, and S. Prahl, Appl. Opt. 28, 2292 (1989).
4. Peter et al, Phys. Med. Biol. 1991, Vol 35, No.5, 1317-1334

VII.2 Determination on Minimum Detectable Difference for Transcendent Turbid Media and Absorption

VII.2.1 Introduction

Optical signals transmitted through the breast depend on composition of the tissue, i.e., the amount of fat, glandular tissues, and vascular tree. It also depends on the presence and extent of fibrosis, inflammations, cysts, and neoplasia. These different parts can not cause the very big difference of observation as a dark-clear bar pattern does when they are illuminated with an uniform light. Due to the mixing up from the diffusive scattering, the details of the part in the object with the lower irradiation difference will be more difficult to recognized at the detector. To simulate better imaging for an object in the practical condition similar to that in a real breast tissue, the minimum contrast of the object has to be determined. The irradiation difference from the different part of an object may be caused by the absorption, the scattering, or the both, which depends on the nature of the tissue. Studies have shown that the absorption in normal breast tissue is very small, and the loss of the transmitted photons from tissue was mainly due to the multi-scattering. Therefore, the major work in this chapter is concentrated at object contrast that would be achieved from the different scattering properties of the different types of tissue.

Near infrared laser technology offers a non-ionizing radiation advantage over the conventional x-ray method to image the shadow of objects. One of several optical methods used currently[1-10] is to gate the early-light with a large signal dynamic range and

high spatial resolution for breast cancer screening to measure the shadow of tumors in breasts due to the differences in scattering and absorption coefficients. Optical signals transmitted through the breast depend on the amount of fat, composition and density of internal media, glandular tissues, vascular supply, and the presence and extent of fibrosis, inflammations, cysts, and neoplasia. With recent advances[3-10]in ultrashort lasers and ultrasensitive photo-detectors, the spatial resolution of optical images on the order of 0.1-mm can be achieved[1,4] in a modeled turbid medium. A study of morphological differences and optical properties, such as the dependence of the transport mean free path on diseased tissues is needed in order to identify the type of tumors with high fidelity.

VII.2.2 Experimental Method and Setup

The 2D imaging of two different semi-translucent modeled phantoms in thick highly scattering host Intralipid solutions using time-resolved Fourier-Kerr imaging. Translucent phantom solutions as small as a 2-mm thickness with as small as a 0.1% concentration difference from the 55-mm thick surrounding scattering host environment and 0.5-mm width semi-transparent bars with $\Delta OD=0.14$ can be clearly identified using digital video processed data. The object sample was made of a 2mm-thickness cell filled with a concentration ranged from 1% to 4% from the 55mm thick surrounding scattering host environment, which made of a 2% Intralipid. The host sample was place inside a 55mm-thickness cell filled by 2% Intralipid solution. The different image contrasts would be obtained for a same hidden-in object using different imaging techniques due to the several different dependence of the contrast: the gating time and the spatial spectrum

(aperture size dependence). The former is based upon the time-dependence of the different components of the transmitted signal, and the latter is based upon the Fourier spatial spectrum filtering. In this chapter, the temporal and spatial contrast varying and its limitation from CW, F-CW, Kerr and Kerr-F imaging systems will be examined.

The minimum phantom opacity difference of hidden objects of various size in turbid media was measured as a function of the thickness, location, and transport mean free path of the scattering media. Experimental results will determine the resolving capability of a minimum object contrast for a time-resolved and non-time-resolved imaging systems.

The time-resolved and CW images of bar charts with different opacity under different intralipid concentrations will be detected. The image contrast of the chart inside the intralipid solutions with different concentrations and different locations will be measured.

The experimental setup of the time and 4F-space gated Kerr Fourier transillumination imaging system is shown in Fig.VII.2.2.1 and Fig.VII.2.2.2. Higher spatial frequency components from diffusive noise is removed at the Fourier plane by the induced Kerr aperture. A single shot Nd^{+}:glass mode-locked laser generating 1054-nm 8-ps pulses was used as the probing pulse. The Kerr gate consisted of a pair of crossed calcite polarizers and a CS_2 cell. The Kerr cell was placed at the back focal plane of the lens L_1. This arrangement is the main difference to the conventional optical Kerr gate. The second harmonic 527-nm beam was used to actuate the Kerr gate. A cooled CCD camera system with 16-bit resolution was used to detect the shadow of the transmitted signal with 2.5×10^5 detection pixels. A Fourier spatial filtering technique coupled with

the ultrafast time gated imaging has greatly improved the dynamic range and signal-to-noise ratio. The spatial dimension of the gating laser pulse radial profile automatically induces a spatial aperture at the Kerr cell to effectively remove the higher frequencies.

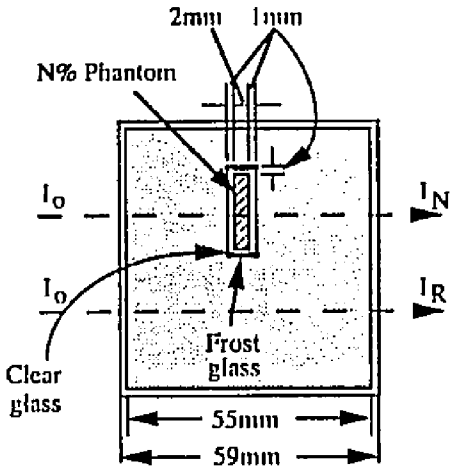

Fig.VII.2.2.1 Sample to determine the minimum contrast in turbid media using a picosecond Kerr-Fourier time-spatial imaging system

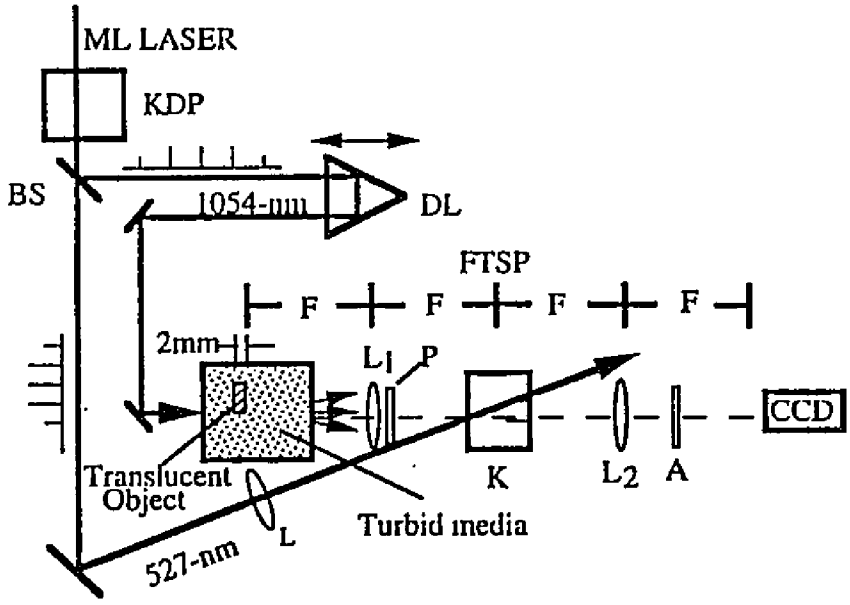

Fig.VII.2.2.2 Kerr Fourier imaging system to determine the minimum contrast in turbid media.

In this manner, when collimated ultrashort laser pulse enters a turbid material, the forward propagation ballistic and snake signals have a plane wavefront and a quasi-plane wavefront, respectively. These earlier arrival components will appear at the central DC frequency region of the Fourier transform spectrum plane (FTSP). The multi-scattered diffusive light at large angles has a spherical wavefront formed by off-axis line rays. This later arriving diffusive light will spread around as the higher spatial frequencies and can be gated either by using an ultrafast time gate or a spatial filter.

Intralipid solutions were used as the host and one of the phantom turbid media. For an 2% diluted Intralipid stock solution of 10% (final solution was 0.2%), the transport coefficients, μ_t, of this modeled turbid medium at input wavelengths of 625-nm and 1060-nm are ~ 1/(2.4-mm) and 1/(5.0-mm), respectively, which are similar to that of human breast tissues. The absorption length of the modeled Intralipid solution is on the order of 500-mm. The effect of absorption was negligible in our experimental arrangements. The modeled phantom was a diluted Intralipid solution of various concentrations from 1% to 4% contained in a 2-mm thick by 10-mm width rectangular glass cell situated in the middle of the turbid medium as shown in the inset of Fig.VII.2.2.2. The second type of phantom was a printed test dark/white bar chart on a thin cellophane sheet with variable optical densities for the dark and white bars.

VII.2.3 Experimental Results

Two measured time-resolved 2D images with inserted phantoms of 3% and 4% diluted Intralipid stock solutions situated in the middle of a 55-mm thick box filled with

a 2% diluted Intralipid solution are shown in Figs.VII.2.3.1a-I and 1a-II, respectively.

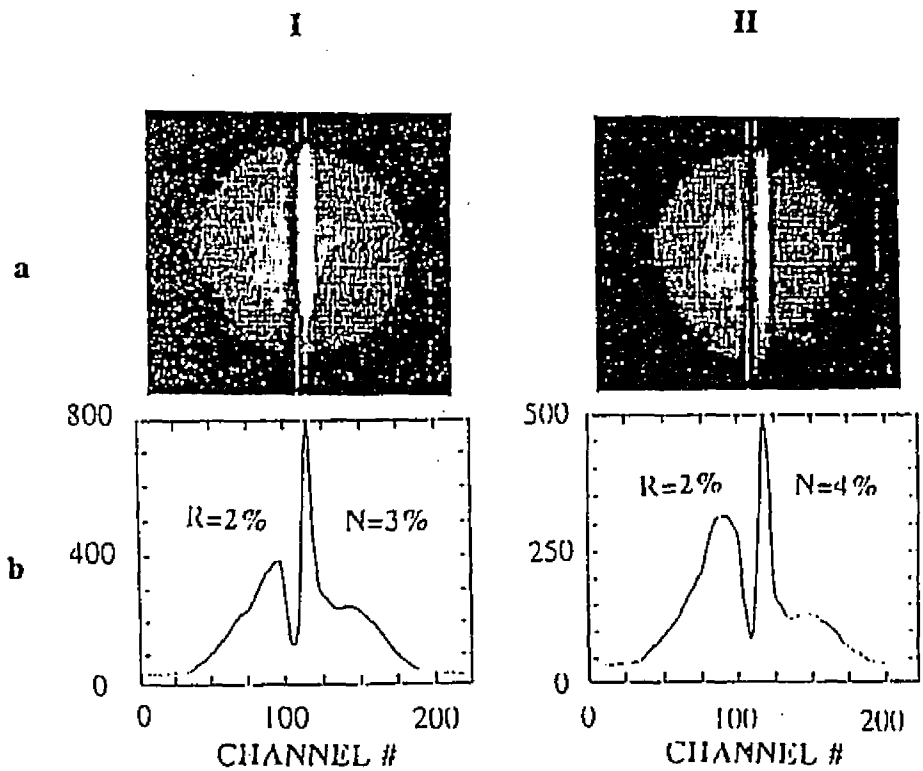

Fig.VII.2.3.1 Early time images of 2-mm thick translucent Intralipid phantoms in a host 55-mm thick R=2% diluted Intralipid stock solution. The brighter left beam circle was the early light through the background turbid medium. The right part of the image circle was the early light through the phantom cell. The sharp dark/white stripe at the center of the image was accounted for by the scattering / transmission from the frost/clear parts of the phantom cell side wall.

(I) N = 3% Intralipid Phanton; (a) 2-D image; (b) 1-D digitized intensity profile; (II) N=4% Intralipid Phantom; (a) 2-D image; (b) 1-D digitized intensity profile. The vertical axis of (b) is the measured digitized counts of signal integrated from row #60 to row #120, then subtracted by 1000 counts. The noise level of the CCD system was 1037 ± 1 counts. The error bar was either ~ ±5% or ±1 counts whichever was greater. The horizontal axis of (b) is the channel # of the CCD. Each channel was equivalent to a ~ 40-μm object width.

The transmitted signal intensity from the 3% phantom in Fig.VII.2.3.1a-I is brighter than that from the 4% phantom in Fig.VII.2.3.1a-II. The 2-mm thick phantoms with a Δ (≡ N - R) = 1% concentration difference of diluted Intralipid solution can be visually

identified, where N and R are the concentration of the phantom and the hosting material, respectively. The 1-D digitized intensity profiles in Fig.VII.2.3.1b have confirmed the visual evaluation. Using digital processed data, translucent phantoms in a host scattering medium with even smaller concentration difference of $\Delta \sim 0.1\%$ has been distinguished from the host as shown in Fig.VII.2.3.2. The ratio of the normalized transmitted signals from two phantoms with Δ=0.1% is $[I_N/I_R]/[I_{N-0.1\%}/I_R] \sim 0.96$. This 4% difference between

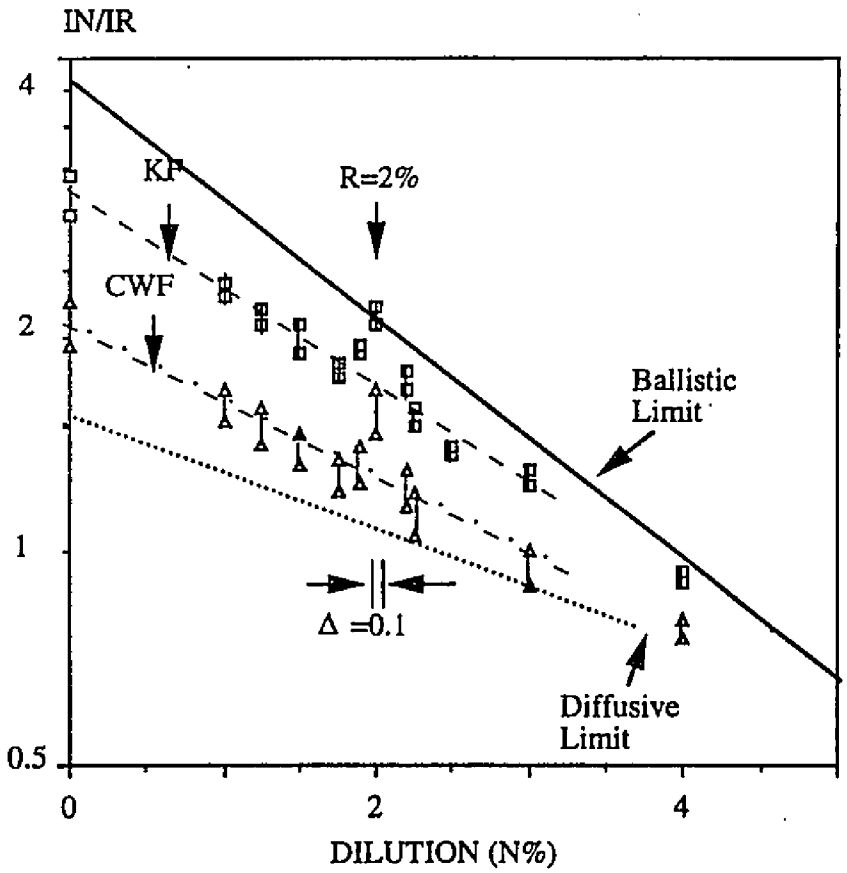

Fig.VII.2.3.2 The early KF gated transmitted signal of translucent phatoms as a function of Intralipid concentration. The horizontal axis, N, is the phatom dilution percentage from a 10% Intralipid stock solution. The vertical log axis is the early KF transmitted intensity through the phantom of N concentration, I_N, nirmalized by the reference signal, I_R, tranmitted through the 55-mm surrounding 2% Intralipid solution. $I_R=I_0 \exp(-55/26)-6.5\times10^{-10}I_0$. Each data ppppoint is an average of four to six independent measurement.

two phantoms can be quantitatively distinguished.

In Fig.VII.2.3.2, the ratio of the early time gated transmitted signals through the phantom, I_N, with the signal through the reference host medium, I_R, are plotted as a function of the concentration of phantoms from 0 to 4% diluted Intralipid solution. For comparison, the cw-Fourier gated transmitted signals are also plotted as a function of the phantom concentration. The salient features of the curves in Fig.VII.2.3.2 indicate that phantoms with the concentration difference of $\Delta \leq 0.1\%$ (or 5% relative scattering coefficient change $\equiv \Delta/R$) from the stock solution can be distinguished using the digital information. As the concentration of the phantom, N, is increased, the transmitted early radiation from the phantom Intralipid solution immersed in a 55-mm thick 2% diluted Intralipid stock solution have been measured. There is a small peak for both KF and CWF imaging when the concentration of the phantom (N=2%) is equal to the surrounding host (R = 2%) Intralipid solution.

To determine the smallest optical density difference of phantoms relative to the surrounding host that can be imaged through the Intralipid solution, a second type of phantom consisting of a test dark/white bar chart with various opacity differences was used. The optical density of the dark bars varied from OD 0.7 to 5 and the white bars varied from OD 0.1 to 4. The width of the bar was varied from 0.25-mm to 0.75-mm. These semi-transparent phantoms were inserted in the middle of a transparent sample cell with inside dimensions of $(5.5\text{-cm})^3$ filled with a 2.2% Intralipid solution. The measured contrast of a bar with the OD ratio of dark/white = 2.0/1.7 was slightly worse than that of a bar with the OD ratio of dark/white = 1.0/0.7 since the amount of photons

transmitted for the latter case is higher. The 2D early-time images and 1D digitized intensity profile of 0.5-mm test dark(OD 0.92)/white(OD 0.78) bar was measured by time-resolved KF imaging is displaced in Fig.VII.2..3.1. Phantom bars with a difference of $\Delta OD = 0.14$ can be clearly identified.

VII.2.4 Discussion

The model sample system consists of a 55-mm thick turbid medium consisting of a R% diluted Intralipid solution (host) and a 2-mm thick glass cell filled with N% diluted Intralipid solution (phantom). The measured normalized early light transmitted signal of the N% Intralipid phantom inside a R% turbid background Intralipid solution can be written as

$$I_N/I_R = T\, I_o \exp[-\mu_N z - \mu_R (t-z-2)]/\{I_o \exp[-\mu_R t]\} = T \exp[-\mu_N z + \mu_R (z+2)], \quad (1)$$

where I_N is the transmitted signal through the N% phantom, I_R is the transmitted signal through the R% background medium, I_o is the incident laser intensity, T is a transmission factor of the phantom due to the interface reflections between the glass windows and the turbid medium, μ_N is the attenuation coefficient for the early light (first 10-ps) of N% Intralipid phantom (a value between the scattering coefficient and the transport coefficient with the unit of 1/mm), μ_R is the attenuation coefficient for the reference turbid medium, t is the thickness of the sample cell, z is the phantom thickness which is 2-mm with two 1-mm thick glass windows.

The attenuation coefficient is approximately proportional to the concentration of the Intralipid stock solution. The attenuation coefficient of the phantom, μ_N, in a reference R=2% Intralipid host can be approximately written as

$$\mu_N \sim N\%/R\% \ \mu_R \tag{2}$$

Eq.1 can be rewritten as

$$I_N/I_R \sim T \exp[2 + (1-N/R)z] \ \mu_R \tag{3}$$

For a phantom with thickness of z = 2-mm in a R = 2% host, eq.3 can be simplified as

$$I_N/I_R = T \exp[4-N] \ \mu_R \tag{4}$$

For a clear water phantom where N = 0, $I_o/I_{ref} = T \exp[4\mu_R]$. Plotting the data points on a semi-log graph or fitting the experimental results as a function of N, the attenuation coefficient can be deduced from the slope = $1/\mu_R$. At the same time, the transmission factor T can also be numerically extracted. Using the data displayed in Fig.VII.2.3.2, the experimental μ_t is deduced to be 1/2.6 mm^{-1} from KF imaging and is 1/3.8 mm^{-1} from CWF imaging. These values are situated between the scattering coefficient at 1054-nm wavelength, μ_s, of 1/2.2 mm^{-1} and the transport coefficient, μ_t, of 1/5.0 mm^{-1} which corresponds to the attenuation coefficients[11] for the pure ballistic signal

and the diffusive component, respectively. These two measured values of μ_R = 1/2.6 mm^{-1} and 1/3.8 mm^{-1} indicated that signals obtained from KF and CWF imaging techniques are accounted for by the signals from ballistic, snake, and diffusive components. Using KF imaging, most of the signals collected are ballistic/snake-like due to the effective time and spatial gating. For signals obtained from CWF imaging where only the spatial filtering exists which acts like a time-gate, they are dominated by snake-like and a portion of diffusive photons. The transmission factor, T, through the phantom in equation 1 can be fitted to be 74±4% through out both curves in Fig.VII.2.3.2 except at the point where the phantom concentration, N, was nearly equal to the surrounding medium of R=2%. The fitted transmission factor for N=2% phantoms in R=2% background from KF imaging are CWF imaging is 98±4%. This T factor is higher than expected value and may be accounted for by the constructive interference between the two glass windows (see N=2% shown in Fig.VII.2.3.2) of the phantom cell.

VII.2.5 Summary

The limitation on imaging semi-transparent phantoms embedded in a highly scattering environment was experimentally determined using a non-invasive and non-destructive time- and spatial-gated Kerr-Fourier transillumination imaging system. Weak-absorbing phantoms, 0.25-mm wide dark/white bars with an opacity difference of ΔOD=0.14 have been distinguished from a thick highly scattering 2.2% Intralipid solution. For a translucent scattering phantom, less than a 5% relative scattering coefficient change (Δ/R = 0.1%/2%) of a 2-mm thick phantom can be separated from the background

medium with the absolute signal difference of ~ 10^{-10}. From the data fitting of the transmitted signal as a function of the phantom concentration, the attenuation coefficient of the early light which is a mixture of the scattering coefficient and the transport coefficient has been determined.

References

1. L. Wang, P. Ho, C. Liu, G. Zhang, R. R. Alfano, "Ballistic 2-D imaging through scattering walls using an ultrafast Kerr gate", Science, 253, 769-771 (1991)
2. M. A. Duguay and A. T. Mattick, "Ultrahigh speed photography of picosecond light pulses and echoes", Appl. Opt. 10, 2162-2170 (1971).
3. L. Wang, P. Ho, X. Liang, H. Dai, R. Alfano, "Fourier-Kerr Imaging in Thick Turbid Media", Optics Letters, 18 241-243 (1993).
4. D. Benaron, D. Stevenson, "Optical time of flight absorbance imaging of biomedical media", Science, 259, 1463-1466, (1993)
5. B. Das, K. Yoo, R. Alfano, "Ultrafast time gated imaging", Opt. Lett., 18, 1092-1094 (1993)
6. J. Izatt, M. Hee, D. Huang, E. Swanson. C. Lin, J. Schuman, C. Puliafito, J. Fujimoto, "Micron-resolution biomedical imaging", Opt. & Phot. News, 4, no.10, 14-19, (1993)
7. H. Chen, Y. Chen, D. Dillworth, E. Leith, J. Lopez, J. Valdmanis, "Two dimensional imaging through diffusive media using 150 fs gated holographic technique", Opt.Lett., 16 487-9 (1991)
8. M. Duncan, R. Mahon, L. Tankersley, J. Reintjes, "Spectral & temporal characteristics

of spontaneous Raman scattering in the transient regime", Opt. Lett., 16 1868-1870 (1991)

9. L. Wang, P. Ho, R. Alfano, "Time-resolved Fourier Spectrum and Imaging in Highly Scattering Media", Appl. Opt. 32, 5043-5048 (1993).

10. L. Wang, X. Liang, P. Ho, R. Alfano, "Time and Fourier-space gated optical Imaging in Thick Turbid Media", SPIE, 1888 2-5 (1993).

11. H. van Staveren, C. Moes, J. van Marle, S. Prahl, M. Van Gemert, "Light scattering in Intralipid in the wavelength range of 400-1100 nm", Appl. Opt. 30, 4507-4514 (1991)

VII.3 Time-resolved Imaging of Translucent Droplets in Highly Scattering Turbid Media

VII.3.1 Introduction

To observe translucent objects inside a highly scattering environment, early ballistic/snake light imaging[1-9] technique offers a non-destructive and non-invasive method. In this section an experiment result about 2D imaging of translucent droplets is introduced. Where, phantoms without container boundaries, with different densities entered into a highly scattering host Intralipid solution using time-resolved Kerr-Fourier imaging. The spatial distribution of the translucent droplets inside the 50-mm thick surrounding scattering host environment can be clearly visualized.

VII.3.2 Experimental Method and Setup

The experimental setup of the time and 4F-space gated Kerr-Fourier (KF) transillumination imaging system has been described in chapter II. In this 4F system, the transmitted shadow signal located at the front focal point plane was collected and transformed by a lens L_1 to the Kerr cell located at the back focal plane. With the time and induced spatial gating, the Fourier spectrum after the Kerr cell was retransformed and imaged by the second lens L_2 to the detector plane. A single shot Nd^+:glass mode-locked laser generating 1054-nm 8-ps pulses was used as the probing pulse. The Kerr gate consisted of a pair of crossed calcite polarizers and a CS_2 cell. The Kerr cell was placed at the back focal plane of the entrance lens. The second harmonic 527-nm beam was

used to actuate the Kerr gate. Higher spatial frequency components from diffusive noise is removed at the Fourier plane by the induced Kerr aperture. A cooled CCD camera system with 16-bit resolution was used to detect the shadow of the transmitted signal with $2.5x10^5$ detection pixels. A Fourier spatial filtering technique coupled with the ultrafast time gated imaging has greatly improved the dynamic range and signal-to-noise ratio. The spatial dimension of the gating laser pulse radial profile automatically induces a spatial aperture at the Kerr cell to effectively remove the higher spatial frequencies.

A schematic of the sample phantom and host cell arrangement is shown in Fig.VII.3.2.1. Diluted Intralipid solutions[10-13] of various concentrations and pure water were used for the phantom droplets in a 2% diluted Intralipid host turbid cell. The inside dimension of the host cell was 50x50x50 mm^3. The phantom droplets were generated in

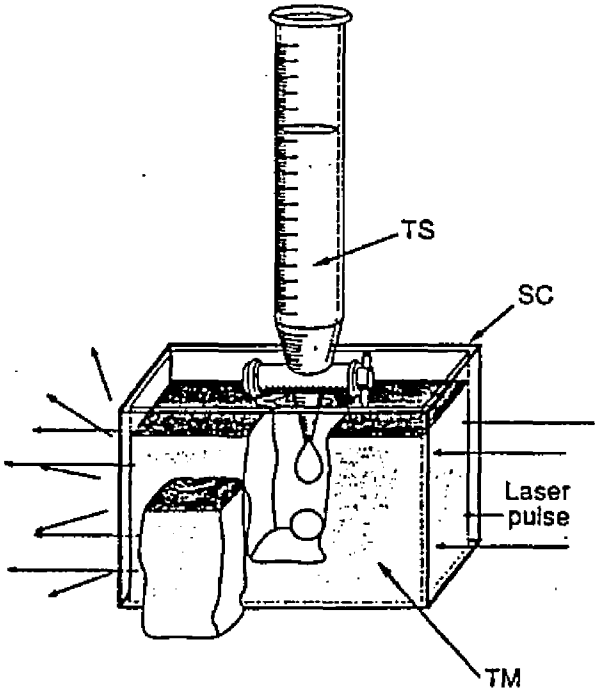

Fig.VII.3.2.1 Experimental setup of turbid sample cell and translucent intralipid phantom droplets. The cut from the side section of the cell displays pictorially the droplet releasing inside the host medium. SC: Sample cell with inside size 50x50x50mm^3; TM: 2% dilution of a 10% stock Intralipid solution for the host turbid medium; TS: Translucent phantom sample, x% diluted Intralipid solution in a buret.

a 50-mL Kimex buret with a straight bore stopcock with a PTFE plug. The subdivision or the limit of error of this buret is 0.1-mL. For a 2% diluted Intralipid stock solution of 10% (final solution was 0.2%), the measured attenuation coefficient[10] from the KF imaging system of this 2% diluted Intralipid solution is 1/(2.6-mm). Due to the additional time gating, this attenuation coefficient measured from the time-spatial gated approach was found to be larger than the scattering coefficient of ~ 1/(3.7-mm) obtained from both the cw Fourier[10] and the standard cw collimated transmission[14] approach. The absolute signal collected was ~ 10^{-10} of the input probe beam. The absorption length of the modeled Intralipid solution is on the order of 500-mm and can be neglected in our experimental arrangements.

VII.3.3 Experimental Results

Two measured time-resolved KF 2D images of water droplets dropped into the middle of a 50-mm thick host cell are shown in Figs.VII.3.3.1a to 1b. Since the scattering loss from the water droplet is less than that from the surrounding host, the intensity of the projected water droplet image was brighter. The shape of these water droplets depends on the amount of water released. The delay time between the stopper opening and the photographic time was varied from ~ 2 to 10 seconds. The inhomogeneity of the brighter circle in Fig.VII.3.2.1 corresponds to the collection aperture or signal beam diameter of ~ 12.7-mm was accounted for by the non-uniformity of the laser intensity distribution. To determine the contrast of the transmitted early snake light images as shown in Figs.VII.3.3.2a to 2d, four different phantom droplets with 1%, 2%,

3%, and 5% diluted Intralipid solutions were dropped into a 2% host medium, respectively. The projected image from the 5% Intralipid droplet shown in Fig.VII.3.3.1d is the darkest due to the increased scattering from the droplet, while the projected image from the 2% Intralipid droplet shown in Fig.VII.3.3.2b is hardly distinguishable from the surrounding host with the identical scattering property. The images obtained from the 1%

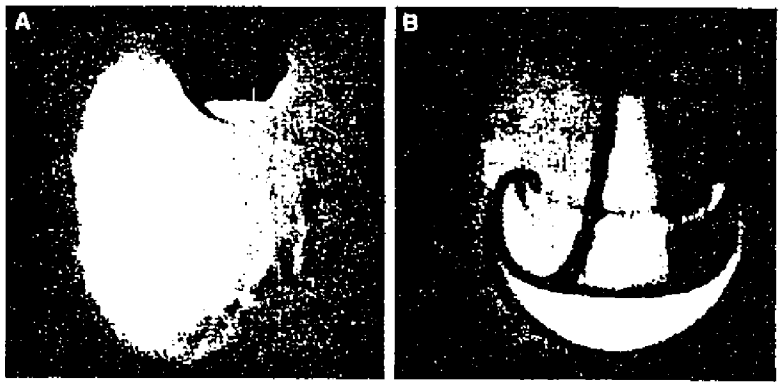

Fig.VII.3.3.1 Early time 2D shadow images of water phantom droplets in a host 50-mm thick of 2% diluted Intralipid stock solution. The spatial distribution of the water drop depends on the amount of water and the delay of release time. The dark shadow at the top middle part of the white laser beam circle is the end tip of the buret. (a) ~2 seconds delay from releasing stopper; (b) ~10 seconds delay from releasing stopper

Intralipid droplet shown in Fig.VII.3.3.2a is brighter than that from the 2% surrounding host and the image from the 3% Intralipid droplet in Fig.VII.3.3.1c is darker. A 1% concentration dilution difference between the phantom droplet and the host medium can be visually distinguished. The changes of the shape of the drop can be measured. A much smaller concentration difference of 0.1% between the phantom droplets and the host

medium could be identified using digital video signal processing (10). This work demonstrates that small differences in scattering properties and shapes of small dimension translucent droplets can be spatially determined inside a large host turbid medium which may be useful in moving towards the optical mammography. A droplet phantom inside a scattering host without an artificial container boundary is an ideal object to simulate,

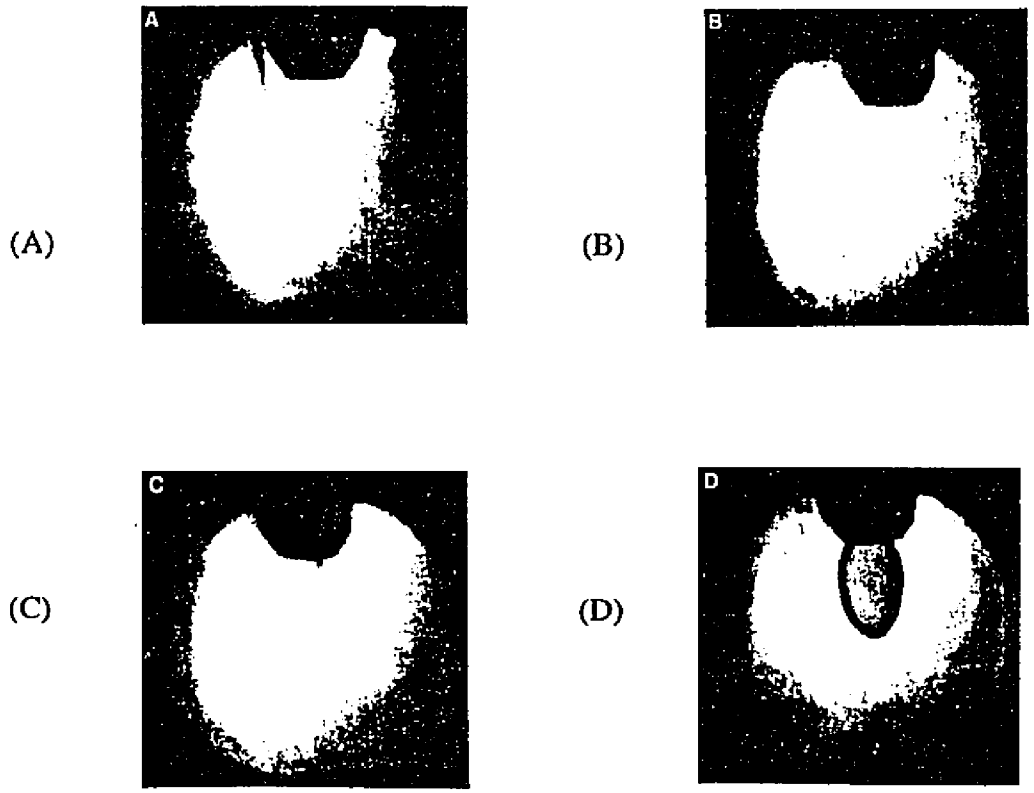

Fig.VII.3.3.2 Early time images of translucent Intralipid phantom drops of various concentrations in a host 50-mm thick 2% diluted Intralipid stock solution. (a) 1% Diluted Intralipid Phantom Drop; (b) 2% Diluted Intralipid Phantom Drop; (c) 3% Diluted Intralipid Phantom Drop; (d) 5% Diluted Intralipid Phantom Drop.

for example, a tumor embedded in a tissue or droplets in jet exhaust. Furthermore, the early light transillumination technique can be adapted to determine the spatial distribution

of the particle size and shape of the fuel spray in air from an jet nozzle to improve the efficient engine design.

References

1. L. Wang, P. Ho, C. Liu, G. Zhang, R. R. Alfano, Science, 253, 769-771 (1991)

2. M. A. Duguay and A. T. Mattick, Appl. Opt. 10, 2162-2170 (1971).

3. L. Wang, P. Ho, X. Liang, H. Dai, R. Alfano, Opt. Lett., 18 241-243 (1993).

4. M. Hee, D. Huang, E. Swanson. J. Fujimoto, Opt. Lett., 18 950-952, (1993)

5. D. Benaron, D. Stevenson, Science, 259, 1463-1466, (1993)

6. H. Chen, Y. Chen, D. Dillworth, E. Leith, J. Lopez, J. Valdmanis, Opt.Lett., 16 487-9 (1991)

7. M. Duncan, R. Mahon, L. Tankersley, J. Reintjes, Opt. Lett., 16 1868-1870 (1991)

8. B. Das, K. Yoo, R. Alfano, Opt. Lett., 18, 1092-1094 (1993).

9. K. M. Yoo, B. B. Das. R. Alfano, Opt. Lett., 17 958-960 (1992)

10. X. Liang, L. Wang, P. Ho, R. Alfano, (in preparation).

11. L. Wang, P. Ho, R. Alfano, Appl. Opt. 32 5043-5048 (1993)

12. M. S. Patterson, B. Chance, B. C. Wilson, Appl. Opt. 28, 2331-2336 (1989)

13. F. Liu, K. M. Yoo, R. R. Alfano, Opt. Lett., 18, 432-434 (1993)

14. H. van Staveren, C. Moes, J. van Marle, S. Prahl, M. van Gemert, Appl. Opt. 32, 4507-4514 (1991)

Chapter VIII

Summary and Future Direction

VIII.1 Summary

Various optical detection and imaging methods have been used to determine ultra-small hidden objects in turbid and bio-medical media. In the conventional steady-state transillumination or diaphanography, direct visual interpretation or IR mapping from video imaging was used for an physical examinations of the breast. In this method, the signal consisting of ballistic, snake, and diffusive components were detected without the use of time or space gating which results in higher noise levels with poor spatial resolution (>1cm).

When photons travel through a turbid medium, three signal components can be defined: diffusive, ballistic, and snake. The diffusive scattered photons of the signal travel over a much larger distance in turbid samples, and lost most of the true image information. The ballistic ones take the shortest path through the medium, and the snake component arises from those photons scattering within a small forward angular cone which arrives on the onset of the diffusive component, both of which carry true image information.

A significantly large dynamic range of over $\geq 10^{10}$ was used to obtain image information of an object in thick turbid media, such as mucked media and breast tissues. It was shown that a simple time-gating approach does not achieve this required dynamic

range. A Fourier spatial filtering technique coupled with ultrafast time gating was shown to increase the capability to greatly improve the dynamic range and diffusive noise rejection. For a single stage Kerr-Fourier imaging system, the rejection ration of diffusive photons has been demonstrated to be ~10^{-10}. A image system consisted of a double-stage Kerr and spatial gate would provide a diffusive photon rejection are ~ 10^{18}.

When laser light travels through a turbid medium, the diffusive scattering photons act as a secondary light source to illuminate a hidden-in object. Other than the primary illumination from the input laser beam, this secondary source is a non-collimated point source and depends on the depth of phantoms in the turbid medium. The intensities of these two types of light source change rapidly with different depths inside turbid media. Regions closer to the input surface of turbid media, there are more ballistic/snake photons, and less diffusive photons, while a regions closer to the exiting surface of turbid media, the diffusive photons are much more than the ballistic/snake photons. The transmitted image signal is less distorted for the object located closer to the exiting surface than that to the input surface. Both factors determine the quality, contrast, and SIR of the detected images. In all cases studied the contrast and the S/N increased when the depth was increased (close to the exit window) and the contrast was higher for the time gated image. In addition, the contrast and S/N were lower for the smaller bar width. The contrast and S/N curves at different depths were smoother for the time gated image than that from the ungated image. When the bar width was reduced, the improvement of the time gate was larger. For instance, in m 2% diluted Intralipid solution, the contrast improvement between the object located at the exit plane and the entrance plane is ~ 10% for 1-mm

bars and ~ 95% for the 0.25-mm bars for Kerr-Fourier over cw-Fourier imaging. The time gate on the image contrast was more significant for objects located at the entrance window than that for objects at the exit window.

Optical signals transmitted through the breast depend on composition of the tissue, i.e., the amount of fat, glandular tissues, H_2O, and vascular blood tree. The breast also depends on the presence and extent of fibrosis, inflammations, cysts, and neoplasia. These different components can not cause as large a difference as that a dark-clear bar pattern does when they are illuminated with an uniform light. Therefore, a study need to be done using a phantoms with a smaller contrast (<<100%) than that for a dark-clear bar pattern (~100%). To test this, the minimum detectable contrast of the object was determined. Experimental results determined the resolving capability of a minimum object contrast for a time-resolved and non-time-resolved imaging systems. It was demonstrated that weak-absorbing 2mm-thick phantom with an opacity difference of $\Delta OD=0.14$ can be distinguished from a 50-mm thick highly scattering 2.2% Intralipid solution (for a hidden 0.4mm spatial resolution of black-clear object) with l_t ~4.6mm. For a translucent scattering phantom, less than a 5% relative scattering coefficient change ($0.05mm^{-1}$-scattering attenuation) of a 2-mm thick phantom(Δ/R = 0.1%/2%) can be separated from the background medium (l_t ~4.6mm) with the absolute signal difference of ~ 10^{-10} in 1054nm wavelength.

The estimation of detectable snake photons number in biomedical media and experimental results obtained form time- and space- gated imaging system have shown the possibility to develop an optical mammography for breast cancer. In illumination

energy 12J/cm^2 at 1054nm and 1mm resolution, for benign tissue (l_t ~5.1mm), fatty tissue (l_t ~1.4mm), and fibroadenoma (l_t ~2.08mm), the detectable photon number is $1.4x10^{10}$, $1.5x10^5$, and 14, respectively.

The degrading of spatial resolution was studied using time-space imaging system or 527nm and 1054nm. It has shown that in 50mm 2% diluted Intralipid solution with l_t ~4.6mm, the spatial resolution with less than 0.4mm was obtained.

A space and time imaging system can be used to determine an accurate scattering attenuation coefficient of turbid media. For 2% diluted Intralipid solution, the experimental μ_t is deduced to be 1/2.6 mm^{-1} from KF imaging and is 1/3.8 mm^{-1} from CWF imaging. These values are situated between the scattering coefficient at 1054-nm wavelength, μ_s, of 1/2.2 mm^{-1} and the transport coefficient, μ_t, of 1/5.0 mm^{-1} which corresponds to the attenuation coefficients for the pure ballistic signal and the diffusive component, respectively. These two measured values of μ_R = 1/2.6 mm^{-1} and 1/3.8 mm^{-1} indicated that signals obtained from KF and CWF imaging techniques are accounted for by the signals from ballistic, snake, and diffusive components. Using KF imaging, most of the signals collected are ballistic/snake-like due to the effective time and spatial gating. For signals obtained from CWF imaging where only the spatial filtering exists which acts like a time-gate, they are dominated by snake-like and a portion of diffusive photons. Difference of the scattering attenuation coefficient, μ_s, deduce from the time-resolved to the transillumination measurements are accounted for by the later-arrived snake and diffusive photons within the collection angle of the detector. About 20% ~ 30% error can be obtained to CW measurement method. Time-space imaging methods provide a

significant reduction of the diffusive photons from the conventional collimation transillumination approach to determine the true scattering coefficient, μ_s, of turbid media.

To observe translucent objects inside a highly scattering environment, early ballistic/snake light imaging technique offers a non-destructive and non-invasive method. An experiment result about 2D imaging of translucent droplets with different concentrations was introduced. Where, phantoms without container boundaries, with different densities entered into a highly scattering host Intralipid solution using time-resolved Kerr-Fourier imaging. The spatial distribution of the translucent droplets inside the 50-mm thick surrounding scattering host environment can be clearly visualized.

This work demonstrates that small differences in scattering properties and shapes of small dimension translucent droplets can be spatially determined inside a large host turbid medium which may be useful in moving towards the optical mammography.

VIII.2 Future Directions

VIII.2.1 Optical Mammography

The major direction of this research in the future will focus on testing different types of thick breast tissues (cancer vs normal) for developing an optical mammography shadowgram breast screening system. Different wavelengths from 1000nm to 1300nm will be used to probe the tissue H_2O and fat in breast to attempt to separate tumors from normal breast tissues. The future effort will be done to increase the detectable signal level (ballistic/snake photon number) and reduce diffusive noise level using repeatable IR

laser light pulses for a longer illumination time. A series of experiments should be designed to image the cancer tissue hidden in normal breast tissue with thickness of ~ 5cm in vivo and in vitro applications with spatial resolution ~1mm using time-resolved and non-time-resolved imaging systems. According to the difference of blood, water, fat, normal, and cancer tissues, imaging experiments will be performed to investigate the contrast difference using multiple wavelengths to perform difference spectral shadowgram images of the breast.

To perform the future research work, the following improvements of the experimental setup will need to be accomplished:

1. Light source

1) To enhance rejection efficiency for diffusive photons using a time and space gating system, a repeatable tunable pulse laser with wavelength 800nm to 1300nm with pulse width from 1ps to 10ps with pulse power density of 5mJ per centimeter square. A possible laser system is Chromium-Doped Forsterite laser over the wavelength range from 1130nm to 1367nm, the pulse width of 1ps, repetition rate from ~0.25KHz to 2.0KHz, maximum power output of 2.8W, beam divergence of 0.5mrad, beam size of 5cm. The latter will be used in combination with pulses from Ti:Sapphire laser system covering from 800nm to 950nm.

2) Collimated CW pulse light source at repetition rate of with wavelength from 850nm to 1300nm, and effective power density of 1W per centimeter square is needed to investigate the improvement by a spatial filter to act as an early-time detection device.

When the laser pulses pass through tissues, the temperature of tissue will increase

due to the absorption of laser energy by tissue. To avoid the damage to the tissue organs due to the overheat, the maximum energy absorption and temperature increase must be determined. The data may be obtained by solving a heat conduction equation[1]. In this research work, a simple method was used to estimate the energy absorption and temperature rise. To do so, the same sample as used in Chapter II.2 was used, which is shown in Fig.VIII.2.1.1 below (refer to Fig.II.2.7.2.1 on page 62). A laser light with energy density of 12J/cm^2 uniformly illuminated at the front surface of 5x5cm^2 of a tissue sample with volume of 5cmx5cmx5cm in 60 seconds (total input energy is 300J). The volume density of the tissue m ~1.1gram/cm^3[2]. The specific heat for biological tissue σ ~3.7J/gram·°C[3]. The absorption length of tissue is assumed as l_a = 500mm. Based these conditions, it is assumed that the absorption is approximately uniform inside the sample tissue since the input laser light illumination is uniform in tissue surface, and the absorption length l_a is much longer than the sample tissue thickness. In the worst case,

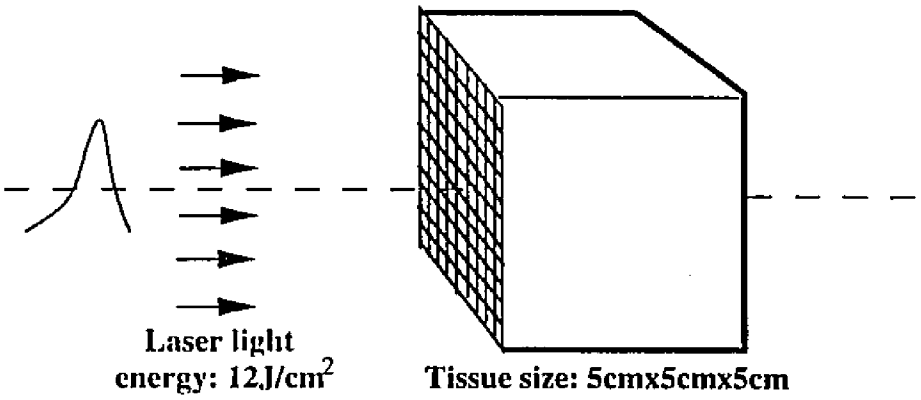

Fig.VIII.2.1.1 Sample and illumination arrangement for estimation of temperature increase due to the energy absorption.

all the laser light energy is completely absorbed in the breast. The energy absorbed per 1-cm^3 volume is E/V = 300J/[5x5x5cm^3] = 300J/125cm^3 = 2.4J/cm^3. The most extreme temperature rise expected in a 1-cm^3 volume due to the light energy absorption is:

$$\Delta T \leq (E/V)/(m \cdot \sigma)$$

$$\leq 2.4J/cm^3 \cdot (1.1gram/cm^3) \cdot (3.7J/gram \cdot cm^3 \cdot °C) = 0.59°C/cm^3,$$

This rise is less than maximum allowable temperature increase of 1°C (average value in 1cm^3)[4].

2. Image Detector

A CCD detector with a higher readout rate and lower SNR is needed to perform continuous imaging with 3KHz repeatable laser light source. The readout rate higher than 30 frame per second is preferred to fit TV format (higher readout rate can be done by modifying readout format by CCD manufacture). The readout-rate per frame is less than 30ms.

VIII.2.2 Fuel Spray

Knowledge of the spatial distribution of fuel spray in liquid rocket and airplane engines can lead to improve the efficiency of operation. This knowledge often requires very expensive full scale injector screening test. In order to overcome this problem,one required advancement is a diagnostic approach that would provide for detailed in situ quantitative data for dense sprays found in rocket engines. Once a method is developed, it is likely that this technique can be synergistically applied to aircraft engines to gain a better understanding of the fuel injection and mixing processes. In either cases, better

design and more effective engines may be obtained. Rocket engine fuel spray, and to a certain degree aircraft engine fuel spray as well, tend to be dense and opaque to light. This create several difficult diagnostic problems. For instance, in a large rocket engine, the flow rate of liquid fuel plus oxidizer can be as large as 200lb/sec in chamber of 20 inches diameter. The quality of ordinary optical measurements of the size of a fuel drop located in a dense spray are often degraded because of the noise that arises from multiple photon scattering in a jet spray. The density of these sprays limits the use of traditional optical technique, e.g., Malvern and Phase Doppler Particle Analyzer, in making drop size or set break-up measurements. The use of penetrating radiation technique, such as X-rays, neutron radiography, requires working fluids with physical properties quite dissimilar to engine propellants or their simultants.

Optical imaging studied here offers a novel approach to be used in fuel spray diagnosis in high scattering region. Ultrafast early light imaging technique has been applied to measure the spatial distribution of hidden objects embedded in highly scattering media. Sub-millimeter resolution has been obtained using the 2D and 3D imaging techniques. In a liquid rocket engine, the fuel is injected at high velocity (15-100m/sec) through orifices into the combustion chamber where the fuel forms liquid sprays. Using high pressure gas, the sprays break-up into small droplets.

The future research on the Fuel spray imaging will concentrate the image of individual particle size and shapes a function of time. Collimated laser light will be used to illuminates the highly scattering regime, and the transmitted photons are detected by a 4F system in different angles to create a deep distribution-map.

References

1. Ashley J. Welch and Garrett D. Polhamus, "Measurement and prediction of thermal injury in the retina of the rhesus monkey", IEEE Tran. on Biol. Eng. BME-31, 10, 633, (1984).

2. Patricia A. Athey and Frank P. Hadlock., *Ultrasound in Obstetrics & Gynecology,* 249-252, published by C. V. Mosby Co., St. Louis, (1981).

3. G. Duncan, *Physics for Biologists,* 24, published by John Willey & Sons, Inc., New York, (1975).

4. Webb, S., *The Physics of Medical Imaging,* 607, IOP Publishing, New York (1990).

Chapter IX

Appendix

IX.1 Electromagnetic field propagation in a double-stage Kerr gate

The analysis on the electromagnetic field in a single-stage Kerr gate has been done[1]. In this section, the analysis for a double-stage Kerr gate is derived. The analysis starts from the EM field entering the analyzer of the first Kerr gate, (for the detailed discussion on a single-, and double- stage Kerr gate, refer to Chapter II):

First, assuming the output EM field after the first Kerr cell represented by $\hat{e}_2$, i.e.:

$$\hat{e}_2 = \mathrm{Re}(\cos\Theta \cdot e^{i\delta\phi_1}\, \underline{X} + \sin\Theta_1\, \underline{Y})E_0 e^{i\omega t};$$

where $e^{i\delta\phi_1}$ is the EM field phase shift induced in the first Kerr cell; $\underline{X}$ and $\underline{Y}$ represent the horizontal and vertical coordinate directions; Θ_1 is the spatial angle between the direction of the first analyzer and the vertical direction.

After the first analyzer,

Then the EM vector after the analyzer is:

$$\hat{e}_3 = \mathrm{Re}[-\cos\Theta_1 \cdot \cos(\Theta_1 + 90) \cdot e^{i\delta\phi_1} + \sin\Theta_1 \cdot \sin(\Theta_1 + 90)]\, E_0 e^{i\omega t}$$

$$= \mathrm{Re}(-\cos\Theta_1 \cdot \sin\Theta_1 \cdot e^{i\delta\phi_1} + \sin\Theta_1 \cdot \cos\Theta_1)\, E_0 e^{i\omega t};$$

Where $\hat{e}_3$ is oriented at the first analyzer as shown in Fig.III.3.3.1. After the second polarizer, the EM field will be splitted into X- and Y-components respectively along the directions represented by $\underline{X}$ and $\underline{Y}$. If the second polarizer is also oriented in the same

direction as the first analyzer represented by Θ_1, then the EM field after the second polarizer (refer to Fig.II.3.3.1 in Page 69) is:

$$\hat{e}_4 = \mathrm{Re}\{[-\cos\Theta_1 \sin\Theta_1 e^{i\delta\phi}_1 + \cos\Theta_1 \sin\Theta_1]\cos\Theta_1 \underline{X}$$
$$+ [-\cos\Theta_1 \sin\Theta_1 e^{i\delta\phi}_1 + \sin\Theta_1 \cos\Theta_1]\sin\Theta_1 \underline{Y} \} E_0 e^{i\omega t}$$

After the last (i.e. the second) analyzer in the second Kerr gate, the second induced-phase shift $e^{i\delta\phi}_2$ happened in the second Kerr cell will be added to the $\underline{X}$-component of EM field, which is represented by $\hat{e}_5$:

$$\hat{e}_5 = \mathrm{Re}\{[(-1+\sin^2\Theta_1)\sin\Theta_1 e^{i\delta\phi}_1 + \cos^2\Theta_1 \sin\Theta_1] e^{i\delta\phi}_2 \underline{X}$$
$$+ [-\cos\Theta_1 \sin^2\Theta_1 e^{i\delta\phi}_1 + \sin^2\Theta_1 \cos\Theta_1] \underline{Y} \} E_0 e^{i\omega t}$$
$$= \mathrm{Re}[\sin\Theta_1 \cos^2\Theta_1 (1-e^{i\delta\phi}_1)e^{i\delta\phi}_2 \underline{X} + [\cos\Theta_1 \sin^2\Theta_1 (1-e^{i\delta\phi}_1)\underline{Y}] E_0 e^{i\omega t}$$

$$= \mathrm{Re}\{ \tfrac{1}{2}i^{-1} (e^{i\Theta}_1 - e^{-i\Theta}_1) [\tfrac{1}{2}i^{-1} (e^{i\Theta}_1 + e^{-i\Theta}_1)]^2 (1-e^{i\delta\phi}_1)e^{i\delta\phi}_2 \underline{X}$$
$$+ \tfrac{1}{2}i^{-1} (e^{i\Theta}_1 + e^{-i\Theta}_1) [\tfrac{1}{2}i^{-1} (e^{i\Theta}_1 - e^{-i\Theta}_1)]^2 (1-e^{i\delta\phi}_1)\underline{Y} \} E_0 e^{i\omega t}$$

When Θ_1 is assumed as 45 degree,

$$\hat{e}_5 = \mathrm{Re}\{ \tfrac{1}{4} 2^{\frac{1}{2}} [(1-e^{i\delta\phi}_1)e^{i\delta\phi}_2 \underline{X} + (1-e^{i\delta\phi}_1) \underline{Y} \} E_0 e^{i\omega t}$$

When the analyzer of the second pair of polarizers is also oriented at Θ_2=45 degree, the EM field in 45 degree direction, represented by $\underline{A}$, is:

$$\hat{e}_6 = \tfrac{1}{4} 2^{\frac{1}{2}} \mathrm{Re} \{[(1-e^{i\delta\phi}_1)e^{i\delta\phi}_2 (-\cos\Theta_2) + (1-e^{i\delta\phi}_1)\sin\Theta_2] E_0 e^{i\omega t}\} \underline{A}$$
$$= \tfrac{1}{4} \mathrm{Re}\{[(-1+e^{i\delta\phi}_1)e^{i\delta\phi}_2 + (1-e^{i\delta\phi}_1)] E_0 e^{i\omega t} \} \underline{A}$$

The intensity of the EM field after the second analyzer is:

$$\mathbf{I} = \langle \hat{e}_6^2 \rangle$$
$$= \tfrac{1}{4} E_0^2 [\cos\omega t - \cos(\delta\phi_1 + \omega t) - \cos(\delta\phi_2 + \omega t) + \cos(\delta\phi_1 + \delta\phi_2 + \omega t)]$$

$$= \tfrac{1}{4}E_0^2[\ \cos^2\omega t - 2\cos\omega t + \cos(\delta\phi_1 + \omega t) + \cos^2(\delta\phi_1 + \omega t) - 2\cos\omega t\cdot\cos(\delta\phi_2 + \omega t)$$

$$- 2\cos\omega t\cdot\cos(\delta\phi_1 + \delta\phi_2 + \omega t) + \cos^2(\delta\phi_1 + \omega t) + \cos^2(\delta\phi_1 + \delta\phi_2 + \omega t)$$

$$- \cos(\delta\phi_2 + \omega t)\cdot\cos(\delta\phi_1 + \delta\phi_2 + \omega t)]$$

$$= \tfrac{1}{2}E_0^2[\ 1 - \cos\delta\phi_1 - \cos\delta\phi_2 + \cos\delta\phi_1\cdot\cos\delta\phi_2$$

$$= 2E_0^2\sin^2\tfrac{1}{2}(\delta\phi_1)\cdot\sin^2\tfrac{1}{2}(\delta\phi_2)\ ,$$

Bibliography

1. Alfano, R.R., X. Liang, L. Wang, P. Ho, "The time-resolved imaging of translucent droplets in highly scattering turbid media", Science, 264, 1913-1915 (1994). [III,IV]
2. Anderson-Engles, S., et al.,"Time-resolved transillumination for medical diagnosis", Opt. Lett. 15, 1178-1180, (1990). [I]
3. Ariel, Irving M., and Joseph B. Cleary, "Breast Cancer", published by McGraw-Hill, New York (1987) [II]
4. Athey, P. A. and F. P. Hadlock, *Ultrasound in Obstetrics & Gynecology, 249-252,* published by The C. V. Mosby Co., St. Louis, 1981 [VIII]
5. Benaron, D., D. Stevenson, "Optical time of flight absorbance imaging of biomedical media", Science, 259, 1463-1466, (1993)
6. Berg, R., et al.,"Medical transillumination using short pulse diode lasers", Appl. Opt.. 32. 574-579 (1993). [I]
7. Bartrum, Royal J. ,Jr. and Harte C. Crow,"Transillumination lightscanning to diagnose breast cancer: a feasibility study", AJR 142, 409-414 (1984) [II]
8. Bruckner, A. P., Appl. Opt. 17 3177 (1978) [I]
9. Benaron, D., D. Stevenson, "Optical time of flight absorbance imaging of biomedical media", Science, 259, 1463-1466 (1993) [III,VII]
10. Chance, B., J. Leigh, J. Miyake, D. Smith, S. Nioka, R. Greenfield, M. Finander, K. ufmann, W. Levy, M. Young, P. Cohen, H. Yoshioka, R. Boretsky, "Comparison of time-resolved and un-time-resolved measurements of deoxyhemoglobin in brain",

Proc. Nat. Acad. Sci. 5, 4971-4975 (1988) [I,V]

11. Chance, B. Ed., **Photon Migration in Tissues**(Plenum, New York, 1990). [I]

12. Chance, B. and R. R. Alfano, ed,"Photon migration and imaging in random media and tissue", SPIE, 1888, 1993. [I]

13. Chen, H., Y. Chen, D. Dillworth, E. Leith, J. Lopez, J. Valdmanis, "Two dimensional imaging through diffusive media using 150 fs gated holographic technique", Opt. Lett., 16, 487-9 (1991) [I, III,V]

14. Das, B., et al., "Ultrafast time imaging in thick tissue", to be published in Opt. Lett. [I]

15. Das, B., K. Yoo, R. R. Alfano,"Ultrafast time gated imaging", Opt. Lett., 18, 1092 -1094 (1991) [III,VII]

16. Driver I., J., W. Feather, P. R. King, and J. B. Dawson, "The optical properties of aqueous suspensions of Intralipid, a fat emulsion", Phys. Med. Biol. 12, 1927-1930 (1989) [III,V]

17. Duguay, M. A. and A. T. Mattick,"Ultrahigh speed photography of picosecond laser pulses", Appl. Opt. 10, 2162-2170 (1971). [II,III]

18. Duguay, M. A., and J. W. Hanson, Appl. Phys. Lett., 15 6 (1969) ([I]

19. Duguay, M. A., and J. Hansen, "An ultrafast light gate", Appl. Phys. Lett. 15, 192-194 (1969) [I]

20. Duguay, M. A., and A. T. Mattick, "Ultrahigh speed photography of picosecond light pulses and echoes", Appl. Opt. 10, 1971, 2162-2170. [I,VI,VII]

21. Duguay, M. A., R. Mahon, L. Tankerskey, J. Reintjes, Opt. Lett., 16, 1868 (1991) [I]

22. Duncan, A., et al.,"A multi-wavelength, wideband, intensity modulated optical imaging", SPIE,1888. [I]

23. Duncan, G., *Physics for Biologists,* 24, published by John Willey & Sons, Inc., New York, (1975) [VIII]

24. Duncan, M., R. Mahon, L. Tankersley, J. Reintjes, "Spectral & temporal characteristic of spontaneous Raman scattering in the transient regime", Opt.Lett., 16, 1868-1870 (1991) [III,VII]

25. Edward, A., Profio and Glenis A Navarro,"Scientific basis of breast diaphanography", Med Phys. 16(1), 60-65 1989 [II]

26. Edward A. Sickles,"Breast cancer detection with transillumination and mammography", AJR 142 341-344, (1984) [II]

27. Fujimoto, J., S. De Silversti, E. Ippen, R. Margolis, A. Oseroff, "Femtosecond optical ranging in biological system" Opt. Lett. 11, 150-152 (1986); Science, "Optical coherence tomography" 254, 1178-1182 (1991). [I, V]

28. Gandjbakhche, Amir H., R. Nossal, Roya Dadmarz, Douglas Schwartzentruber, Robert F. Bonner, Expected resolution and detectability of adenocarcinoma tumors within human breast in time-resolved images", SPIE, 2387-18(1995). [III]

29. Gaskill, Jack D.,"Linear System, Fourier Transform, and Optics", (Published by John Wiley & Sons, Ins, 1979 New York) [II]

30. Geslien, G. Eric, J. Ronald Fisher, C. Delaney,"Transillumination in breast cancer detection: screening, failures and potential", AJR 144, 619-622, 1985 [II]

31. Giordmaine, J. A., P. M. Rentzepis, S. L. Shapiro and K. W. Wecht, Appl. Phys.

Lett., 11 216,(1967) [II]

32. Gisvold, John J., Larry R. Brown, Ronald J. Raygor, Nancy Dickerson, Marie K. Ranfranz,"Comparison of mammography and transillumination light scanning in the detection of breast lesions", AJR 147, 191-194 (1986) [II]

33. Goodman, J.,"Introduction to Fourier Optics", McGraw-Hill Book Co., New York (1968) [II,V,VI]

34. Hee, D. Huang, E. Swanson. J. Fujimoto, Opt. Lett., 18 950-952, (1993)

35. Ho, P. P. and R. R. Alfano, Phys. Rev. A20, 2170 (1979) [II]

36. Ho, P. P., and R. R. Alfano, Phys. Rev. A17 2170 (1978) [II]

37. Ho, P. P. and R. R. Alfano, "Optical Kerr effect in liquids", **Phys. Rev.** A20, 2170-82 (1979). [II]

38. Ho, P. P., L. Wang, R. R. Alfano, SPIE 1599 (1991) [II]

39. Ho, P. P., P. Y. Lu, R. R. Alfano, Phys. Rev. A21, 1730 (1980) [II]

40. Ho, P. P. and R. R. Alfano, Phys. Rev. A20, 2170 (1979) [II]

41. Ho, P. P., Y. Liu, R. R. Alfano, J. Chem. Phys. 74 1605 (1981) [II]

42. Hulin, D., A. Mysyrowicz, A. Antonetti, A. Migus, W. Masselink, H. Morkoc, and H. Gibbs, N. Peyghambarian, Phys. Rev. B33 4389 (1984) [II]

43. Ishimaru, a.,"Limitation on image resolution imposed by a random medium"' Appl. Opt. 17, 348 (1978) [II,IV]

44. Izatt, L., M. Hee, D. Huang, E. Swanson, C. Lin, J. Schuman, C. Puliafito, Fujimoto, "Micro resolution biomedical imaging", Opt. & Phot. News, 4, No.10, 14-19 (1993) [III,VII]

45. Key et al, Phys. Med. Biol. 1991, Vol.36, No.5 579-590. [III]

46. Kopeika, N. S., S. Solomon, and Y.Gencay,"Wavelength variation of visible and near in-fared resolution through the atmosphere: dependence on aerosol 2nd meteorological conditions" J. Opt. Soc. Am. 71, 892 (1981) [II,IV]

47. Kopeika, N. S.,"Spatial frequency dependence of scattered background light: the atmospheric modulation transfer function resulting from aerosol" J. Opt. Soc. Am. 72, 548 (1982) [II,IV]

48. Kusa, Y., A. Ishmaru, A. P. Bruckner, "Experiments on picosecond pulse propagation in a diffusive medium", J. Opt. Soc. Am. 73, 1812-1815 (1983) [II]

49. Kusuo, Y., and A. Ishimaru, "Modulation transfer function and image transmission through randomly distributed spherical particles", J. Opt. Soc. Am., 12, 2330-2335(1985) [IV]

50. Lakowicz, J. and K. Berndt, "Lifetime-selective fluorescence imaging using an rf phase-sensitive camera", Rev. Sci. Instrum., 62, 1727-1735 (1991) [V]

51. Levi, L., "Vision in communication", PROGRESS IN OPTICS, Vo.VII

52. Li, Q. X., T. Jimbo, P. P. Ho, R. R. Alfano, Appl. Opt. 25 1869 (1986) [II]

53. Li, Y., G. Eichman, R. R. Alfano, Appl. Opt.25 209, (1986) [II]

54. Liu, Hanli, Andreas. H. Hielscher, C. Dean Kurth, S. L. Jacques, and Britton Chance, "Time-resolved photon migration in a heterogeneous tissue-vessel model", **SPIE**, 2389, (1995). [III]

55. Liu, F., K. M. Yoo, and R. R. Alfano, "Transmitted photon intensity through biological tissues within various time windows", Opt. Lett., **10**, 740-742 (1994) [II]

56. F. Liu, K. M. Yoo, R. R. Alfano, Opt. Lett., 18, 432-434 (1993) [VII]

57. Lutomirski, R. F., "Atmospheric degeneration of electrooptical system performance"' Appl. Opt. 17, 3915(1978) [II,IV]

58. Madsen, S. J., B. C. Wilson, M. S. Patterson, Y. D. Park, S. L. Jacques, Y. Hefetz, "Experimental test of a simple diffusion model for the estimation of scattering and absorption coefficients of turbid media from time resolved diffusive reflectance measurements", Appl. Opt. 31 3509-17 (1992) [III]

59. Marshall, V. David C. Williams, Kenneth D. Smaith,"Diaphanography as a means of detecting breast cancers", Radiology, 150 339-343, (1984) [II]

60. McMorrow, D., W. T. Lotshaw, G. A. Kenney-Wallace, IEEE J. Quantum Electron. 24 433 (1988) [II]

61. Moon, J. A., R. Mahon, M. D. Duncan, and J. Reintjes, "Resolution limits for imaging through turbid media with diffusive light", Opt. Lett. **18**, 1591 (1993) [IV]

62. Morioka, T., and M. Saruwatari, Opt. Eng. 29 200 (1990) [II]

63. Mose, Christian J. M., Martin C. van Germert, Jan van Marle, William M. Star, Jonhannes P. A Marilnissen, and Scott A. Prahl, "Measurements and calculations of the energy fluence rate in a scattering and absorbing phantom at 633-nm", Appl. Opt. 12, 2292-2296 (1989) [II,I,V,VI]

64. Navarro and A. Profio, "Contrast in diaphanography of the breast", Med. Phys. 15, 1988, 181-187. [I]

65. Ohlsson, B., J. Gundersen, and Dag-Martin Nilsson,"Diaphanography: A method for evaluation of the female breast", World J. Surge.,4 701-708, (1980) [II]

66. Patterson, M. S., B. Chance, B. C. Wilson,"Time-resolved reflectance and transmittance for the noninvasive measurement of optical properties", Appl. Opt. 28, 2331-2336 (1989) [III,VII]

67. Peters et al, Phys. Med. Biol. 1990, Vol.35, No.5 1371-1334 (Homogenized tissue model). [III,VI]

68. Rebane, A., and J. Feinberg, "Time-resolved holography", Nature, 351, 378-380 (1991) [I,IV]

69. Sala, K., and M. C. Richardson, Phys. Rev. A12, 1036 (1975) [II]

70. Scotland, J. C., J. C. Haselgrove, and J. S. Leigh,"Photon hitting density", Appl. Opt 4 1993 [I]

71. Sevick, E., et al.,"Time-dependent photon migration imaging" SPIE, 1599, 1992,274-283.[I]

72. Spears, K.G., J. Serafin, N.H. Abramson, "Chrono-Coherent Imaging for Medicine", IEEE Trans. Biomed. Eng. 36, 1210-1221 (1989); N. H. Abramson and K.G. Spears "Single pulse light-in-flight recording by holography", Appl. Opt., 28 1834-1841 (1989) [I,V]

73. Staveren, Hugo J. van, Christian J. M. Mose, Jan van Marle, Scott A. Prahl, and Martin J. C. van Gemert, "Light scattering in Intralipid-10% in the wavelength range of 400-1100nm", Appl. Opt. 4507-4514 (1991). [III,V,VII]

74. L. Wang, P. Ho, C. Liu, G. Zhang, R.R. Alfano, "Ballistic 2-D imaging through scattering walls using an ultrafast Kerr gate", Science, 253, 769-771 (1991) [IV]

75. L. Wang, Y. Liu, P. P. Ho, R. R. Alfano, "Time-resolved imaging of tissues" ed. B.

Chance, in Proceedings OE/LASE SPIE 1431, pp97-101 (1991). [II,IV]

76. L. Wang, X. Liang, P. P. Ho. R. R. Alfano, " Time and Fourier space gated optical imaging of thick turbid media", SPIE, 1888,(1993) [IV,V,VII]

77. Wang, L., Liang, P. P. Ho, and R.R. Alfano, "Fourier -Kerr imaging in thick turbid media", Opt. Lett.,15, 1993 241-2435. [I]

78. Wang, L., P. P. Ho, R. R. Alfano, "Time-resolved Fourier spectrum and imaging in highly scattering media", Appl. Opt. 26, 5043-5048(1993) [I,II,III,IV,V,VI,VII]

79. Wang, L., P. Ho, C. Liu, G. Zhang, R.R. Alfano, Science, 253, 769 (1991) [I,II,III,VI]

80. Wang, L., X. Liang, P. P. Ho. R. R. Alfano, "Fourier-Kerr imaging in thick turbid media", Opt. Lett. 18, 241-243 (1993) [III,V,VII]

81. Watmough, D. J., "Diaphanography, Mechanism responsible for the images",Acta Radiological Oncology 21 11-15 (1982) [II]

82. Webb, S., "The Physics of Medical Imaging", (IOP Publishing, New York 1990). [II,VI]

83. Ashley J. Welch and Garrett D. Polhamus, "Measurement and prediction of thermal injury in the retina of the rhesus monkey", IEEE Tran. on Biol. Eng. BME-31, 10, 633, (1984) [VIII]

84. Wells, Willard H., "Loss of resolution in water as a result of multiple small-angle scattering", J. Opt. Soc. Am. 59, 686 (1969) [IV]

85. Yoo, K. M., and R. R. Alfano, "Time-resolved coherent and incoherent components of forward light scattering in random media", Opt. Lett. 15, 320-322 (1990) [I,III,IV]

86. Yoo, K.M., et al.,"Imaging objects hidden in highly scattering media using a

femtosecond second-harmonic-generation cross-correlation time gating", Opt.. Lett., 16, 1991, 1019-1021.[I]

87. Yoo, K.M., B.B. Das, R.R. Alfano, Opt. Lett., 17, 958 (1992) [I,VII]

88. Yoo, K. M., Q. Xing, R. R. Alfano, Opt. Lett. 16, (1991) [II]

89. Zardecki, A., Siegfried A. W. Gerstl, and Janon F. Embury, "Mutiple scattering effects in spatial frequency filtering", Appl. Opt. 22, 4124-4131(1984) [II,IV]

90. Zdrojkowswi, R. J., and R. L. Longini, "Optical transmission through whole blood", J.O.S.A. Vo.59, 898-904 (1969) [II,IV]

List of Leming Wang's Publications

1. Y. Li, L. Wang, P. Neos, G. Zhang, X. Liang, R. R. Alfano, "Demonatration of An Ultrafast Non-collinear Second-Harmonic Generation Based 4X4 Optical Switching Array", **Opt. Lett.** 14, 347-349(1989).
2. N. Schiller, X. Chao, X. Liang, L. Wang and R. R. Alfano, "Compact Picosecond Nd;Glass Mode-lock Laser With Variable Cavity Length 5 - 21m", **Appl. Opt.** 28, 946(1989).
3. L. Wang, G. Zhang, P. Ho, R. R. Alfano, **Proc. of Int. Laser'89**, 1074, ST Press (1990).
4. L. Wang, P. Ho, C. Liu, G. Zhang, R.R. Alfano, "Ballistic 2-D imaging through scattering wall using an ultrafast optical Kerr gate", **Science**, 253, 769 (1991).
5. P.P. Ho, L. Wang, R. R. Alfano, "Picosecond Kerr Gate for Ballistic/snake Time-gated Optical Imaging", **Proc. of Int. Lasers'91**, 277 (1991).
6. L. Wang, P. P. Ho, Y. Liu, R. R. Alfano,"Time-resolved imaging of tissues", **SPIE** 1431 97-101 (1991).
7. P. P. Ho, L. Wang, R.R. Alfano, "Ballistic time-gated imaging in turbid media", ed. Alfano Proceeding **SPIE** 1599, 325 (1992).
8. L. Wang, P. P. Ho, R. R. Alfano, " Time-Space Gated Optical Imaging in Thick Turbid Media for Breast Cancer Screening", in Proceedings **LEOS** (1992).
9. P. P. Ho, L. Wang, and R. R. Alfano, Pro. Soc. Photo-Opt. Instrum. Eng. **1599**, 325 (1992).

10. L. Wang, P. P. Ho, R. R. Alfano, "Double-Stage Picosecond Kerr Gate For Ballistic Time-Resolved Imaging in Turbid Media", **Appl. Opt.** 32, 535-540(1993).

11. L. Wang, P. Ho, X. Liang, H. Dai, R.R. Alfano, "Fourier-Kerr imaging in thick turbid Media", **Opt. Lett.** 18, 241-243(1993).

12. L. Wang, P. P. Ho, R. R. Alfano, "Time-Resolved Fourier Spectrum and Imaging in Highly Scattering Media", **Appl. Opt.** 32, 5043-5048(1993).

13. L. Wang, P. P. Ho, R. R. Alfano,"Time-space gated optical imaging in thick turbid media for breast cancer screening", in Proceedings **SPIE** 1888, 2-5(1993).

14. L. L. Kalpaxis, L. Wang, P. Galland, X. Liang, P. P. Ho, R. R. Alfano,"Three-dimensional temporal image reconstruction of objects hidden in highly scattering media by time-gated optical tomography", **Opt. Lett.** 18 1691-1693(1993).

15. P. P. Ho, L. Wang, X. Ling, L. L. Kapaxis, and R. R. Alfano', Snake light tomography", **Optics & Photonics News**, October 23-27(1993).

16. R. R. Alfano, X. Liang, L. Wang, and P. P. Ho, "Time-resolved imaging of translucent droplets in highly scattering turbid media", **Science**, 264, 1913-1915(1994)

17. P.P. Ho, X. Liang, L. Wang, R. R. Alfano, " Snake-light translucent phantoms tomography", **OSA** Proceedings on advances in optical imaging and phantom migration, **21**, 122-125 (1994)

18. L. Wang, X. Liang, P. Galland, P. P. Ho, R. R.. Alfano, "True attenuation coefficient of turbid matter measured by early time gating", accepted to be published, **Opt. Lett.** (1995).

19. X. Liang, L. Wang, P. P. Ho, R. R.. Alfano, "Two-dimensional Kerr-Fourier imaging

of translucent phantoms in thick turbid media", accepted to be published, **App. Opt.** (1995).

20. R. R. Alfano, X. Liang, L. Wang, P. P. Ho, "Time-resolved imaging of oil droplets in highly scattering solid solution", **SPIE**, to be published(1995).

21. X. Liang, L. Wang, P. P. Ho, R. R.. Alfano, "True scattering coefficient of turbid media", **SPIE**, to be published (1995).

22. Q. Z. Wang, X. Liang, L. Wang, P. P. Ho, and R. R.. Alfano, "Fourier spatial filter acts as a temporal gate for light propagating ", Accepted to be published, **Opt. Lett.** (1995).